Measurement of K*(892)$^{\pm}$ in Proton+Proton collisions with ALICE at the LHC and Study of Particle Production using Color String Percolation Model

Ph.D. Thesis

By

Pragati Sahoo

DISCIPLINE OF PHYSICS

INDIAN INSTITUTE OF TECHNOLOGY INDORE

November 2018

Measurement of K*(892)$^{\pm}$ in Proton+Proton collisions with ALICE at the LHC and Study of Particle Production using Color String Percolation Model

A THESIS

Submitted in partial fulfilment of the

requirements for the award of the degree

of

DOCTOR OF PHILOSOPHY

By

Pragati Sahoo

DISCIPLINE OF PHYSICS

INDIAN INSTITUTE OF TECHNOLOGY INDORE

November 2018

INDIAN INSTITUTE OF TECHNOLOGY INDORE

CANDIDATE'S DECLARATION

I hereby certify that the work which is being presented in the thesis entitled **"Measurement of K*(892)$^{\pm}$ in Proton+Proton collisions with ALICE at the LHC and Study of Particle Production using Color String Percolation Model"** in the partial fulfillment of the requirements for the award of the degree of **DOCTOR OF PHILOSOPHY** and submitted in the **DISCIPLINE OF PHYSICS, Indian Institute of Technology Indore**, is an authentic record of my own work carried out during the time period from December 2014 to November 2018 under the supervision of Prof. Raghunath Sahoo, Associate Professor, Discipline of Physics, Indian Institute of Technology Indore, Indore, M.P., India.

The matter presented in this thesis has not been submitted by me for the award of any other degree of this or any other institute.

Pragati Sahoo

(PRAGATI SAHOO)

This is to certify that the above statement made by the candidate is correct to the best of my knowledge.

R. Sahoo

Signature of Thesis Supervisor
(Dr. RAGHUNATH SAHOO)

Ms. PRAGATI SAHOO has successfully given her Ph.D. Oral Examination held on 11th April, 2019.

K. Eswara Murali 11/4/19
(Chairperson (OEB))
Date:

(External Examiner)
Date: 11/04/19

R. Sahoo
(Thesis Supervisor)
Date: 11.04.19

(PSPC Member)
Date: 11/4/19

(PSPC Member)
Date: 11/4/2019

(Convener, DPGC)
Date: 11-04-19

(Head of the Discipline)
Date: 11.04.19

Dedicated to LIFE...

Acknowledgements

First and foremost I would like to thank my supervisor, Prof. Raghunath Sahoo, for giving me the opportunity to work on this research topic and profoundly motivating me throughout my Ph.D. journey. I would like to express my sincere gratitude for his precious guidance, better inputs with logical thinking and consistent encouragement. His approach to handle any problem and his critical remarks in physics or apart from physics is very prudent. His farsighted action will be a constant source of encouragement for me. His sense of humour, strictness to his students but also constant support at the same time, all make an invaluable mix, from which I benefited a lot as a student. I am very much grateful to have a good person and successful physicist as my supervisor.

I would like to thank my PSPC committee members Prof. Manavendra Mahato and Prof. Subhendu Rakshit for their support and motivations. I would like to thank all the faculty and staff members of the IIT Indore for their help and support. I am very grateful to the Physics Department of IIT Indore for providing me all the required facilities. I thank my fellow labmates of the Experimental High-Energy Physics group at IIT Indore for the stimulating discussions and for all the fun we have had in the last years. Specially working with Aditya Bhaiya, Bhaswar Bhaiya, Arvind, Dhananjaya, Nirbhay Bhaiya, Pooja, Prakhar Bhaiya, Rutuparna, Sudipan Bhaiya, Suman, Sushanta, Swatantra Bhaiya, Trambak Da and Yunus Da has truly been a privilege. I would like to express my thanks to my friends-cum-roomies Aparna, Camellia, Deepika, Madhurima and Suchismita for making the time at IIT Indore memorable and much more cheerful.

I would like to thank Dr. Federico Antinori (Spokesperson, ALICE), Dr. Tapan Kumar Nayak (Deputy spokesperson, ALICE), Dr. Subhasis Chattopadhyay (ALICE-India spokesperson) for their support in various matters in spite of their busy schedules. I would like to thank the physics analysis group members and conveners in ALICE, Dr. Francesca Bellini, Dr. Alexander Philipp Kalweit, Dr. Stefania Bufalino, Dr. Viktor Riabov and Dr. Anders Garritt Knospe for their valuable suggestions and constructive criticism.

I would like to specially thank Dr. Angela Badalá for inviting me to INFN, Catania and giving me the opportunity to work together in Catania in resolving analysis related issues. This helped in bringing the analysis to a paper form.

I am acknowledging the financial supports from ALICE Project No. SR/MF/PS-01/2014-IITI(G) of Department of Science & Technology (DST), Government of India. I am also thankful to the DST for funding my travel to CERN and various collaboration meetings within India.

I was very much privileged to have a great friend circle beyond my research collaboration. My close friends and associates Kasinath Das, Kishora Nayak, Shibananda Sahoo helped a lot by ensuring a balance and perfect life in all respect beyond my research life. The good memories shared with them have made my life more pleasant and memorable.

I am indebted to my school, college and university teachers, who have supported me a lot with their valuable guidance as a result of which I have reached to this stage. I bow down to all of them specially, Prof. Swapna Mahapatra and Prof. Karmadev Maharana for their magnanimous support and encouragement for my career.

Here I am also showing my gratitude to Mrs. Gayatri Sahu for her caring nature and support during my stay at IIT Indore. I spent wonderful moments with Mamun and Papun. I restored the playfulness on my life by playing and engaged with them.

My journey would not have come this far without the love and support *of my loving parents, brother, sister and my whole family. I am blessed with such generous people around me. My heartfelt thank to my family and friends for their constant love, support, encouragement and having faith in me. I have learned a lot from everyone during my PhD period, which has helped me and will encourage me to cherish for rest of my career.*

(Pragati Sahoo)

ABSTRACT

The basic questions are always been asked by the mankind that, "What are the constituents of matter and what are its properties?". Many experiments are done to explain it and demonstrate the atom, its subatomic particles called nucleons (such as protons and neutrons) and further constituents of nucleons are called quarks. As the search turned to go into smaller scales, experiments needed to become even larger in the form of particle accelerators. On the pursuit of these fundamental questions numerous scientific fields are created. These fields include Quantum Mechanics, Quantum Chromodynamics (QCD), Quantum Electrodynamics (QED), Electro-Weak Theory (EWT), High-Energy Physics, and Particle Physics. Quarks exhibit the property of color confinement, which means a quark cannot be found in isolation. Confinement is the reason for bound state of quarks which are called as hadrons. The hadrons particularly, protons and neutrons together with electrons make up the visible matter of the Universe. With color confinement property, asymptotic freedom is also retained for quarks. In contrast to confinement, the asymptotic freedom suggests, at high temperatures or high baryon densities the quarks and gluons confined inside hadrons can be de-confined. This de-confined state of quarks and gluons is called as Quark-Gluon Plasma (QGP).

In laboratory, QGP can be experimentally created by ultra-relativistic heavy-ion collisions. The experimental search for de-confined state of quarks and gluons started with the first heavy-ion collisions in the Relativistic Heavy Ion Collider (RHIC) at Brookhaven National Laboratory (BNL) and thereafter in the Large Hadron Collider (LHC) at CERN. At RHIC, various signatures like jet quenching, azimuthal anisotropy, J/ψ suppression, strangeness enhancement indicated the creation of QGP. At the LHC, the colliding particles energy is in TeV scale, which is $\sim$ 10 times higher than RHIC. A Large Ion Collider Experiment (ALICE) at LHC is a dedicated experiment for the creation of QGP and study its properties. To study the properties of strongly interacting matter produced in the

ultra-relativistic collisions, various probes are required. The lifetime of the fireball created in Pb–Pb collisions at LHC is $\mathcal{O} \sim 10$ fm/c. The resonances by definition are very short-lived particle with lifetime $\tau \sim 1$ fm/c (10^{-23} s) can be used as an excellent probe for the study of system evolution in different time scale and to understand various in-medium phenomena. In this thesis, primarily $K^{*\pm}$ resonance is studied in detail. It is a vector meson (spin 1) containing a strange quark and having lifetime, $\tau_{K^{*\pm}} \sim 4$ fm/c, which is comparable to the fireball created in Pb–Pb collisions.

The formation of QGP and its properties can be explored by the study of such short living particle (which is one of the probes) when it transported through the medium. The transition of QCD matter from hadronic confined phase to QGP de-confined phase is fascinating. Theoretically, there are several signatures of first order phase transition and the critical point has been proposed. The color string percolation model (CSPM) is an approach to investigate the particle production through the percolation of color strings and the phase structure of the hadronic matter. A detailed formalism and methodology of CSPM is discussed in this thesis. In addition, thermodynamical and transport quantities like, energy density, shear viscosity, trace anomaly, speed of sound, entropy density and bulk viscosity of the matter produced in heavy-ion collisions at RHIC by using the CSPM are discussed. The energy and centrality dependence study of percolation parameters and various thermodynamical observables at RHIC energies are done. The electrical conductivity which is a well known observable for strongly interacting matter produced in heavy-ion collisions has drawn considerable interest. So, we estimate the normalised electrical conductivity to temperature ratio using the color string percolation approach. Limiting fragmentation (LF) is another interesting phenomena in high energy multiparticle production process. In this thesis we have revisited the phenomenon of limiting fragmentation for nucleus-nucleus (A+A) collisions in the pseudorapidity distributions of differential cross-section of charged particles ($d\sigma^{\mathrm{AA}}/d\eta$) by considering energy dependent inelastic cross-section (σ_{in}).

The organization of the thesis is as follows:

Chapter 1: This chapter gives an introduction to Standard Model, QCD, QGP and its various signatures. The motivations for relativistic pp and heavy-ion collisions are described. Subsequently, the motivation for resonance study in particular $K^*(892)^{\pm}$ meson measurements are discussed. An introduction to color string percolation model for the particle production is also discussed here along with the hypothesis of limiting fragmentation for particle production in high-energy nuclear collisions.

Chapter 2: In this chapter the experimental facilities at LHC which is based at CERN, Geneva are explained. The ALICE experiment and its different detectors are discussed in details. A detailed description of ITS and TPC detectors which are used significantly for the data analysis is given.

Chapter 3: The transverse momentum spectra have been measured at mid-rapidity and compared with QCD-inspired models (PYTHIA6, PYTHIA8) and hybrid model (EPOS-LHC). Comparison of $K^{*\pm}$ results with the ones obtained for K^{*0} at the same collision energies are also discussed. The collision energy dependence of the transverse momentum p_T spectra, integrated yields, $\langle p_T \rangle$ and K^*/K ratio are explored.

Chapter 4: In this chapter the transport properties in heavy-ion collisions at RHIC energies using color string percolation model (CSPM) are discussed. The transport properties for example, the initial energy density (ε), shear viscosity to entropy density ratio (η/s), trace anomaly (Δ), the squared speed of sound (C_s^2), entropy density, and bulk viscosity to entropy density ratio (ζ/s) are obtained and compared with the lattice QCD calculations for (2+1) flavor. Another observable, the normalised electrical conductivity ($\sigma_{\rm el}$/T) of hot QCD matter as a function of temperature (T) using the CSPM and comparison with various existing results is also discussed. The centrality dependent behaviour of initial temperature of the percolation cluster, energy density, average transverse momentum, shear viscosity to entropy density ratio (η/s) and trace anomaly for different

RHIC energies in the framework of CSPM is studied.

Chapter 5: In this chapter, the phenomenon of limiting fragmentation for nucleus-nucleus (A+A) collisions in the pseudorapidity distribution of charged particles at various energies is studied. Energy dependent σ_{in} is used to get the pseudorapidity distributions of differential cross-section of charged particles and study the phenomenon of LF.

Chapter 6: In this chapter we summarise the results with important findings.

PUBLICATIONS

<u>List of Publications</u>:

(Publications with [*] are included in this thesis.)

1. [*] **"Electrical conductivity of hot and dense QCD matter created in heavy-ion collisions: A color string percolation approach"**

   P. Sahoo, S. K. Tiwari and R. Sahoo, Phys. Rev. D **98**, 054005 (2018).

2. [*] **"Energy and Centrality Dependent Study of Deconfinement Phase Transition in a Color String Percolation Approach at RHIC Energies"**

   P. Sahoo, S. De, S. K. Tiwari and R. Sahoo, Eur. Phys. J. A **54**, 136 (2018).

3. [*] **"Limiting Fragmentation in High Energy Nuclear Collisions in the LHC Era"**

   P. Sahoo, P. Pareek, S. K. Tiwari and R. Sahoo, Phys. Rev. C **99**, 044906 (2019).

4. [*] **"Beam Energy Dependence of Thermodynamic and Transport Properties of Strongly Interacting Matter in a Color String Percolation Approach at the Relativistic Heavy Ion Collider"**

   P. Sahoo, S. K. Tiwari, S. De, R. Sahoo, R. P. Scharenberg and B. K. Srivastava, Mod. Phys. Lett. A **34**, 1950034 (2019).

5. [*] **"Analysis Note: Measurement of $K(892)^{*\pm}$ Mesons at Mid-Rapidity in Minimum-Bias pp Collisions at $\sqrt{s}$ = 5.02 TeV."**

   P. Sahoo and R. Sahoo, *https://alice-notes.web.cern.ch/node/628*

6. [*] **"Analysis Note: Measurement of $K(892)^{*\pm}$ Mesons at Mid-Rapidity in Minimum-Bias pp Collisions at $\sqrt{s}$ = 8 TeV."**

S. De, P. Sahoo and R. Sahoo,
https://alice-notes.web.cern.ch/node/629

7. [*] **"Paper Draft: Energy dependence of $K(892)^{*\pm}$ production in inelastic pp collisions at the LHC."**
   A. Badala, R. Sahoo, K. Garg, P. Sahoo and S. De,
   https://alice-publications.web.cern.ch/node/4270,
   [**ALICE IRC/Editorial board review**].

8. **"Speed of sound in hadronic matter using non-extensive Tsallis statistics"**
   A. Khuntia, P. Sahoo, P. Garg, R. Sahoo and J. CleymansEur. Phys. J. A **52**, 292 (2016)

9. **"Energy and Centrality dependence of $dN_{\rm ch}/d\eta$ and $dE_{\rm T}/d\eta$ in Heavy-Ion Collisions from $\sqrt{s_{\rm NN}}$ =7.7 GeV to 5.02 TeV"**
   A. Nath Mishra, R. Sahoo, P. Sahoo, P. Pareek, N. K. Behera and B. K. Nandi, Eur. Phys. J. A **52**, 319 (2016)

10. **"$\Lambda_{\rm c}^{+}$ production in Pb-Pb collisions at $\sqrt{s_{\rm NN}} = 5.02$ TeV"**
    S. Acharya,...,P. Sahoo *et al.* [ALICE Collaboration], arXiv:1809.10922 [nucl-ex]

11. **"Event-shape engineering for the D-meson elliptic flow in mid-central Pb-Pb collisions at $\sqrt{s_{\rm NN}} = 5.02$ TeV"**
    S. Acharya,...,P. Sahoo *et al.* [ALICE Collaboration], arXiv:1809.09371 [nucl-ex]

12. **"Measuring $\mathrm{K^0_S K^\pm}$ interactions using pp collisions at $\sqrt{s} = 7$ TeV"**
    S. Acharya,...,P. Sahoo *et al.* [ALICE Collaboration], arXiv:1809.07899 [nucl-ex]

13. **"Charged jet cross section and fragmentation in proton-proton collisions at $\sqrt{s}$ = 7 TeV"**
    S. Acharya,...,P. Sahoo *et al.* [ALICE Collaboration], arXiv:1809.03232 [nucl-ex]

14. **"Energy dependence of exclusive J/ψ photoproduction off protons in ultra-peripheral p-Pb collisions at $\sqrt{s_{\rm NN}}$ = 5.02 TeV"**

    S. Acharya,...,P. Sahoo *et al.* [ALICE Collaboration], arXiv:1809.03235 [nucl-ex]

15. **"Multiplicity dependence of light-flavor hadron production in pp collisions at $\sqrt{s}$ = 7 TeV"**

    S. Acharya,...,P. Sahoo *et al.* [ALICE Collaboration], arXiv:1807.11321 [nucl-ex]

16. **"Medium modification of the shape of small-radius jets in central Pb-Pb collisions at $\sqrt{s_{\rm NN}} = 2.76\,{\rm TeV}$"**

    S. Acharya,...,P. Sahoo *et al.* [ALICE Collaboration], JHEP **1810**, 139 (2018)

17. **"Measurement of dielectron production in central Pb-Pb collisions at $\sqrt{s_{\rm NN}}$ = 2.76 TeV"**

    S. Acharya,...,P. Sahoo *et al.* [ALICE Collaboration], arXiv:1807.00923 [nucl-ex]

18. **"p-p, p-Λ and Λ-Λ correlations studied via femtoscopy in pp reactions at $\sqrt{s}$ = 7 TeV"**

    S. Acharya,...,P. Sahoo *et al.* [ALICE Collaboration], arXiv:1805.12455 [nucl-ex]

19. **"Analysis of the apparent nuclear modification in peripheral Pb-Pb collisions at 5.02 TeV"**

    S. Acharya,...,P. Sahoo *et al.* [ALICE Collaboration], arXiv:1805.05212 [nucl-ex]

20. **"Production of the $\rho(770)^0$ meson in pp and Pb-Pb collisions at $\sqrt{s_{\rm NN}}$ = 2.76 TeV"**

    S. Acharya,...,P. Sahoo *et al.* [ALICE Collaboration], arXiv:1805.04365 [nucl-ex]

21. **"Anisotropic flow of identified particles in Pb-Pb collisions at $\sqrt{s}_{\rm NN} = 5.02$ TeV"**

    S. Acharya,...,P. Sahoo *et al.* [ALICE Collaboration].

    JHEP **1809**, 006 (2018)

22. **"Azimuthal anisotropy of heavy-flavour decay electrons in p-Pb collisions at $\sqrt{s_{\rm NN}} = 5.02$ TeV"**

    S. Acharya,...,P. Sahoo *et al.* [ALICE Collaboration], arXiv:1805.04367 [nucl-ex]

23. **"Measurements of low-p_T electrons from semileptonic heavy-flavour hadron decays at mid-rapidity in pp and Pb-Pb collisions at $\sqrt{s_{\rm NN}} = 2.76$ TeV"**

    S. Acharya,...,P. Sahoo *et al.* [ALICE Collaboration], JHEP **1810**, 061 (2018)

24. **"Inclusive J/ψ production at forward and backward rapidity in p-Pb collisions at $\sqrt{s_{\rm NN}} = 8.16$ TeV"**

    S. Acharya,...,P. Sahoo *et al.* [ALICE Collaboration], JHEP **1807**, 160 (2018)

25. **"Suppression of $\Lambda(1520)$ resonance production in central Pb-Pb collisions at $\sqrt{s_{\rm NN}} = 2.76$ TeV"**

    S. Acharya,...,P. Sahoo *et al.* [ALICE Collaboration], arXiv:1805.04361 [nucl-ex]

26. **"Measurement of the inclusive J/ ψ polarization at forward rapidity in pp collisions at $\sqrt{\rm s} = 8$ TeV"**

    S. Acharya,...,P. Sahoo *et al.* [ALICE Collaboration], Eur. Phys. J. C **78**, 562 (2018)

27. **"Inclusive J/ψ production in Xe–Xe collisions at $\sqrt{s_{\rm NN}} = 5.44$ TeV"**

    S. Acharya,...,P. Sahoo *et al.* [ALICE Collaboration], Phys. Lett. B **785**, 419 (2018)

28. **"Υ suppression at forward rapidity in Pb-Pb collisions at $\sqrt{s_{\rm NN}}$ = 5.02 TeV"**
S. Acharya,...,P. Sahoo *et al.* [ALICE Collaboration], arXiv:1805.04387 [nucl-ex]

29. **"Dielectron production in proton-proton collisions at $\sqrt{s} = 7$ TeV"**
S. Acharya *et al.* [ALICE Collaboration], JHEP **1809**, 064 (2018)

30. **"Transverse momentum spectra and nuclear modification factors of charged particles in Xe-Xe collisions at $\sqrt{s_{\rm NN}}$ = 5.44 TeV"**
S. Acharya,...,P. Sahoo *et al.* [ALICE Collaboration], arXiv:1805.04399 [nucl-ex]

31. **"Direct photon elliptic flow in Pb-Pb collisions at $\sqrt{s_{\rm NN}}$ = 2.76 TeV"**
S. Acharya,...,P. Sahoo *et al.* [ALICE Collaboration], arXiv:1805.04403 [nucl-ex]

32. **"Dielectron and heavy-quark production in inelastic and high-multiplicity proton-proton collisions at $\sqrt{s_{\rm NN}}$ = 13 TeV"**
S. Acharya *et al.* [ALICE Collaboration], arXiv:1805.04407 [hep-ex]

33. **"Two particle differential transverse momentum and number density correlations in p-Pb and Pb-Pb at the LHC"**
S. Acharya,...,P. Sahoo *et al.* [ALICE Collaboration], arXiv:1805.04422 [nucl-ex]

34. **"Centrality and pseudorapidity dependence of the charged-particle multiplicity density in Xe-Xe collisions at $\sqrt{s_{\rm NN}}$ = 5.44 TeV"**
S. Acharya,...,P. Sahoo *et al.* [ALICE Collaboration], arXiv:1805.04432 [nucl-ex]

35. **"Anisotropic flow in Xe-Xe collisions at $\sqrt{s_{\rm NN}}$ = 5.44 TeV"**

S. Acharya *et al.* [ALICE Collaboration], Phys. Lett. B **784**, 82 (2018)

36. **"Measurement of D^0, D^+, D^{*+} and D_s^+ production in Pb-Pb collisions at $\sqrt{s_{NN}} = 5.02$ TeV"**
S. Acharya,...,P. Sahoo *et al.* [ALICE Collaboration], JHEP **1810**, 174 (2018)

37. **"ϕ meson production at forward rapidity in Pb-Pb collisions at $\sqrt{s_{NN}} = 2.76$ TeV"**
S. Acharya,...,P. Sahoo *et al.* [ALICE Collaboration], Eur. Phys. J. C **78**, 559 (2018)

38. **"Energy dependence and fluctuations of anisotropic flow in Pb-Pb collisions at $\sqrt{s_{NN}} = 5.02$ and 2.76 TeV"**
S. Acharya,...,P. Sahoo *et al.* [ALICE Collaboration], JHEP **1807**, 103 (2018)

39. **"Azimuthally-differential pion femtoscopy relative to the third harmonic event plane in Pb-Pb collisions at $\sqrt{s_{NN}} = 2.76$ TeV"**
S. Acharya,...,P. Sahoo *et al.* [ALICE Collaboration], Phys. Lett. B **785**, 320 (2018)

40. **"Direct photon production at low transverse momentum in proton-proton collisions at $\sqrt{s} = 2.76$ and 8 TeV"**
S. Acharya,...,P. Sahoo *et al.* [ALICE Collaboration], arXiv:1803.09857 [nucl-ex]

41. **"Neutral pion and η meson production at mid-rapidity in Pb-Pb collisions at $\sqrt{s_{NN}} = 2.76$ TeV"**
S. Acharya,...,P. Sahoo *et al.* [ALICE Collaboration], Phys. Rev. C **98**, 044901 (2018)

42. **"Transverse momentum spectra and nuclear modification factors of charged particles in pp, p-Pb and Pb-Pb collisions at the LHC"**

S. Acharya,...,P. Sahoo *et al.* [ALICE Collaboration], JHEP **1811**, 013 (2018)

43. **"Prompt and non-prompt J/ψ production and nuclear modification at mid-rapidity in p–Pb collisions at $\sqrt{\mathbf{s_{NN}}} = \mathbf{5.02}$ TeV"**

    S. Acharya,...,P. Sahoo *et al.* [ALICE Collaboration], Eur. Phys. J. C **78**, 466 (2018)

44. **"Neutral pion and η meson production in p-Pb collisions at $\sqrt{s_{\rm NN}} = 5.02$ TeV"**

    S. Acharya *et al.* [ALICE Collaboration], Eur. Phys. J. C **78**, 624 (2018)

45. **"$\Lambda_{\rm c}^{+}$ production in pp collisions at $\sqrt{s} = 7$ TeV and in p-Pb collisions at $\sqrt{s_{\rm NN}} = 5.02$ TeV"**

    S. Acharya,...,P. Sahoo *et al.* [ALICE Collaboration], JHEP **1804**, 108 (2018)

46. **"Relative particle yield fluctuations in Pb-Pb collisions at $\sqrt{\mathbf{s}_{\rm NN}} = \mathbf{2.76}$ TeV"**

    S. Acharya,...,P. Sahoo *et al.* [ALICE Collaboration], arXiv:1712.07929 [nucl-ex]

47. **"Constraints on jet quenching in p-Pb collisions at $\sqrt{\mathbf{s_{NN}}}$ = 5.02 TeV measured by the event-activity dependence of semi-inclusive hadron-jet distributions"**

    S. Acharya,...,P. Sahoo *et al.* [ALICE Collaboration], Phys. Lett. B **783**, 95 (2018)

48. **"First measurement of $\Xi_{\rm c}^{0}$ production in pp collisions at $\sqrt{\rm s}$ = 7 TeV"**

    S. Acharya,...,P. Sahoo *et al.* [ALICE Collaboration], Phys. Lett. B **781**, 8 (2018)

49. **"Measurement of Z^{0}-boson production at large rapidities in Pb-Pb collisions at $\sqrt{s_{\rm NN}} = 5.02$ TeV"**

S. Acharya,...,P. Sahoo *et al.* [ALICE Collaboration], Phys. Lett. B **780**, 372 (2018)

50. **"Longitudinal asymmetry and its effect on pseudorapidity distributions in Pb-Pb collisions at $\sqrt{s_{NN}}$ = 2.76 TeV"**
S. Acharya,...,P. Sahoo *et al.* [ALICE Collaboration], Phys. Lett. B **781**, 20 (2018)

51. **"Production of ^{4}He and $^4\overline{\text{He}}$ in Pb-Pb collisions at $\sqrt{s_{\rm NN}}$ = 2.76 TeV at the LHC"**
S. Acharya,...,P. Sahoo *et al.* [ALICE Collaboration], Nucl. Phys. A **971**, 1 (2018)

52. **"Production of deuterons, tritons, ^{3}He nuclei and their antinuclei in pp collisions at $\sqrt{s}$ = 0.9, 2.76 and 7 TeV"**
S. Acharya,...,P. Sahoo *et al.* [ALICE Collaboration], Phys. Rev. C **97**, 024615 (2018)

53. **"Search for collectivity with azimuthal J/ψ-hadron correlations in high multiplicity p-Pb collisions at $\sqrt{s_{\rm NN}}$ = 5.02 and 8.16 TeV"**
S. Acharya,...,P. Sahoo *et al.* [ALICE Collaboration], Phys. Lett. B **780**, 7 (2018)

54. **"J/ψ elliptic flow in Pb-Pb collisions at $\sqrt{s_{\rm NN}} = 5.02$ TeV"**
S. Acharya,...,P. Sahoo *et al.* [ALICE Collaboration], Phys. Rev. Lett. **119**, 242301 (2017)

55. **"Constraining the magnitude of the Chiral Magnetic Effect with Event Shape Engineering in Pb-Pb collisions at $\sqrt{s_{\rm NN}}$ = 2.76 TeV"**
S. Acharya,...,P. Sahoo *et al.* [ALICE Collaboration], Phys. Lett. B **777**, 151 (2018)

56. **"The ALICE Transition Radiation Detector: construction, operation, and performance"**

S. Acharya,...,P. Sahoo *et al.* [ALICE Collaboration], Nucl. Instrum. Meth. A **881**, 88 (2018)

57. **"Kaon femtoscopy in Pb-Pb collisions at $\sqrt{s_{\rm NN}}$ = 2.76 TeV"**
S. Acharya,...,P. Sahoo *et al.* [ALICE Collaboration], Phys. Rev. C **96**, 064613 (2017)

58. **"Systematic studies of correlations between different order flow harmonics in Pb-Pb collisions at $\sqrt{s_{\rm NN}}$ = 2.76 TeV"**
S. Acharya,...,P. Sahoo *et al.* [ALICE Collaboration], Phys. Rev. C **97**, 024906 (2018)

59. **"π^0 and η meson production in proton-proton collisions at $\sqrt{s} = 8$ TeV"**
S. Acharya,...,P. Sahoo *et al.* [ALICE Collaboration], Eur. Phys. J. C **78**, 263 (2018)

60. **"Charged-particle multiplicity distributions over a wide pseudorapidity range in proton-proton collisions at $\sqrt{s}$ = 0.9, 7, and 8 TeV"**
S. Acharya,...,P. Sahoo *et al.* [ALICE Collaboration], Eur. Phys. J. C **77**, 852 (2017)

61. **"Measurement of deuteron spectra and elliptic flow in Pb–Pb collisions at $\sqrt{s_{\rm NN}}$ = 2.76 TeV at the LHC"**
S. Acharya,...,P. Sahoo *et al.* [ALICE Collaboration], Eur. Phys. J. C **77**, 658 (2017)

62. **"Searches for transverse momentum dependent flow vector fluctuations in Pb-Pb and p-Pb collisions at the LHC"**
S. Acharya,...,P. Sahoo *et al.* [ALICE Collaboration], JHEP **1709**, 032 (2017)

63. **"D-meson azimuthal anisotropy in midcentral Pb-Pb collisions at $\sqrt{s_{\rm NN}} = 5.02$ TeV"**
S. Acharya,...,P. Sahoo *et al.* [ALICE Collaboration], Phys. Rev. Lett. **120**, 102301 (2018)

64. **"Measuring $K^0_S K^{\pm}$ interactions using Pb-Pb collisions at $\sqrt{s_{NN}} = 2.76$ TeV"**
S. Acharya,...,P. Sahoo *et al.* [ALICE Collaboration], Phys. Lett. B **774**, 64 (2017)

65. **"Linear and non-linear flow modes in Pb-Pb collisions at $\sqrt{s_{NN}} = \mathbf{2.76}$ TeV"**
S. Acharya,...,P. Sahoo *et al.* [ALICE Collaboration], Phys. Lett. B **773**, 68 (2017)

66. **"J/ψ production as a function of charged-particle pseudorapidity density in p-Pb collisions at $\sqrt{s_{NN}} = 5.02$ TeV"**
D. Adamová,...,P. Sahoo *et al.* [ALICE Collaboration], Phys. Lett. B **776**, 91 (2018)

67. **"Flow dominance and factorization of transverse momentum correlations in Pb-Pb collisions at the LHC"**
J. Adam,...,P. Sahoo *et al.* [ALICE Collaboration], Phys. Rev. Lett. **118**, 162302 (2017)

68. **"Azimuthally differential pion femtoscopy in Pb-Pb collisions at $\sqrt{s_{NN}} = 2.76$ TeV"**
D. Adamova,...,P. Sahoo *et al.* [ALICE Collaboration], Phys. Rev. Lett. **118**, 222301 (2017)

69. **"Production of muons from heavy-flavour hadron decays in p-Pb collisions at $\sqrt{s_{NN}} = \mathbf{5.02}$ TeV"**
S. Acharya,...,P. Sahoo *et al.* [ALICE Collaboration], Phys. Lett. B **770**, 459 (2017)

70. **"Production of π^0 and η mesons up to high transverse momentum in pp collisions at 2.76 TeV"**
S. Acharya,...,P. Sahoo *et al.* [ALICE Collaboration], Eur. Phys. J. C **77**, 339 (2017), [Eur. Phys. J. C **77**, 586 (2017)]

71. **"First measurement of jet mass in Pb–Pb and p–Pb collisions at the LHC"**

S. Acharya,...,P. Sahoo *et al.* [ALICE Collaboration], Phys. Lett. B **776**, 249 (2018)

72. **"Measurement of D-meson production at mid-rapidity in pp collisions at $\sqrt{s} = 7$ TeV"**
S. Acharya,...,P. Sahoo *et al.* [ALICE Collaboration], Eur. Phys. J. C **77**, 550 (2017)

73. **"Energy dependence of forward-rapidity J/ψ and $\psi(2S)$ production in pp collisions at the LHC"**
S. Acharya,...,P. Sahoo *et al.* [ALICE Collaboration], Eur. Phys. J. C **77**, 392 (2017)

74. **"$K^*(892)^0$ and $\phi(1020)$ meson production at high transverse momentum in pp and Pb-Pb collisions at $\sqrt{s_{NN}} = 2.76$ TeV"**
J. Adam,...,P. Sahoo *et al.* [ALICE Collaboration], Phys. Rev. C **95**, 064606 (2017)

75. **"Production of $\Sigma(1385)^{\pm}$ and $\Xi(1530)^0$ in p-Pb collisions at $\sqrt{s_{NN}} = 5.02$ TeV"**
D. Adamova,...,P. Sahoo *et al.* [ALICE Collaboration], Eur. Phys. J. C **77**, 389 (2017)

76. **"Insight into particle production mechanisms via angular correlations of identified particles in pp collisions at $\sqrt{\mathrm{s}} = 7$ TeV"**
J. Adam,...,P. Sahoo *et al.* [ALICE Collaboration], Eur. Phys. J. C **77**, 569 (2017)

77. **"Centrality dependence of the pseudorapidity density distribution for charged particles in Pb-Pb collisions at $\sqrt{s_{NN}} = 5.02$ TeV"**
J. Adam,...,P. Sahoo *et al.* [ALICE Collaboration], Phys. Lett. B **772**, 567 (2017)

78. **"W and Z boson production in p-Pb collisions at $\sqrt{s_{NN}} = 5.02$ TeV"**

J. Adam,...,P. Sahoo *et al.* [ALICE Collaboration], JHEP **1702**, 077 (2017)

79. **"Determination of the event collision time with the ALICE detector at the LHC"**

    J. Adam,...,P. Sahoo *et al.* [ALICE Collaboration], Eur. Phys. J. Plus **132**, 99 (2017)

80. **"Measurement of the production of high-p_{T} electrons from heavy-flavour hadron decays in Pb-Pb collisions at $\sqrt{s_{\mathrm{NN}}}$ = 2.76 TeV"**

    J. Adam,...,P. Sahoo *et al.* [ALICE Collaboration], Phys. Lett. B **771**, 467 (2017)

81. **"Evolution of the longitudinal and azimuthal structure of the near-side jet peak in Pb-Pb collisions at $\sqrt{s_{\mathrm{NN}}} = 2.76$ TeV"**

    J. Adam,...,P. Sahoo *et al.* [ALICE Collaboration], Phys. Rev. C **96**, 034904 (2017)

82. **"Anomalous evolution of the near-side jet peak shape in Pb-Pb collisions at $\sqrt{s_{\mathrm{NN}}}$ = 2.76 TeV"**

    J. Adam,...,P. Sahoo *et al.* [ALICE Collaboration], Phys. Rev. Lett. **119**, 102301 (2017)

83. **"Measurement of electrons from beauty-hadron decays in p-Pb collisions at $\sqrt{s_{\mathrm{NN}}} = 5.02$ TeV and Pb-Pb collisions at $\sqrt{s_{\mathrm{NN}}} = 2.76$ TeV"**

    J. Adam,...,P. Sahoo *et al.* (ALICE Collaboration), JHEP **1707**, 052 (2017)

84. **"Jet-like correlations with neutral pion triggers in pp and central Pb–Pb collisions at 2.76 TeV"**

    J. Adam,...,P. Sahoo *et al.* (ALICE Collaboration), Phys. Lett. B **763**, 238 (2016)

85. **"J/ψ suppression at forward rapidity in Pb-Pb collisions at $\sqrt{s_{NN}} = 5.02$ TeV"**
J. Adam,...,P. Sahoo *et al.* (ALICE Collaboration), Phys. Lett. B **766**, 212 (2017)

86. **"Enhanced production of multi-strange hadrons in high-multiplicity proton-proton collisions"**
J. Adam,...,P. Sahoo *et al.* (ALICE Collaboration), Nature Phys. **13**, 535 (2017)

87. **"Higher harmonic flow coefficients of identified hadrons in Pb-Pb collisions at $\sqrt{s_{NN}} = 2.76$ TeV"**
J. Adam,...,P. Sahoo *et al.* (ALICE Collaboration), JHEP **1609**, 164 (2016)

88. **"Elliptic flow of electrons from heavy-flavour hadron decays at mid-rapidity in Pb-Pb collisions at $\sqrt{s_{NN}} = 2.76$ TeV"**
J. Adam,...,P. Sahoo *et al.* (ALICE Collaboration), JHEP **1609**, 028 (2016)

89. **"D-meson production in p-Pb collisions at $\sqrt{s_{NN}}$ =5.02 TeV and in pp collisions at $\sqrt{s}$ =7 TeV"**
J. Adam,...,P. Sahoo *et al.* (ALICE Collaboration), Phys. Rev. C **94**, 054908 (2016)

90. **"Measurement of azimuthal correlations of D mesons and charged particles in pp collisions at $\sqrt{s} = 7$ TeV and p-Pb collisions at $\sqrt{s_{NN}} = 5.02$ TeV"**
J. Adam,...,P. Sahoo *et al.* (ALICE Collaboration), Eur. Phys. J. C **77**, 245 (2017)

91. **"Pseudorapidity dependence of the anisotropic flow of charged particles in Pb-Pb collisions at $\sqrt{s_{NN}} = 2.76$ TeV"**
J. Adam,...,P. Sahoo *et al.* (ALICE Collaboration), Phys. Lett. B **762**, 376 (2016)

92. **“Correlated event-by-event fluctuations of flow harmonics in Pb-Pb collisions at $\sqrt{s_{\rm NN}} = 2.76$ TeV”**
J. Adam,...,P. Sahoo *et al.* (ALICE Collaboration), Phys. Rev. Lett. **117**, 182301 (2016)

93. **“Measurement of transverse energy at midrapidity in Pb-Pb collisions at $\sqrt{s_{\rm NN}} = 2.76$ TeV”**
J. Adam,...,P. Sahoo *et al.* (ALICE Collaboration), Phys. Rev. C **94**, 034903 (2016)

94. **“Centrality dependence of charged jet production in p–Pb collisions at $\sqrt{s_{\rm NN}}$ = 5.02 TeV”**
J. Adam,...,P. Sahoo *et al.* (ALICE Collaboration), Eur. Phys. J. C **76**, 271 (2016)

95. **“Centrality dependence of ψ(2S) suppression in p-Pb collisions at $\sqrt{s_{\rm NN}}$ = 5.02 TeV”**
J. Adam,...,P. Sahoo *et al.* (ALICE Collaboration), JHEP **1606**, 050 (2016)

96. **“Measurement of D-meson production versus multiplicity in p-Pb collisions at $\sqrt{s_{\rm NN}} = 5.02$ TeV”**
J. Adam,...,P. Sahoo *et al.* (ALICE Collaboration), JHEP **1608**, 078 (2016)

97. **“Particle identification in ALICE: a Bayesian approach”**
J. Adam,...,P. Sahoo *et al.* (ALICE Collaboration), Eur. Phys. J. Plus **131**, 168 (2016)

98. **“Anisotropic flow of charged particles in Pb-Pb collisions at $\sqrt{s_{\rm NN}} = 5.02$ TeV”**
J. Adam,...,P. Sahoo *et al.* (ALICE Collaboration), Phys. Rev. Lett. **116**, 132302 (2016)

99. **“Production of K* (892)^0 and ϕ (1020) in p–Pb collisions at $\sqrt{s_{\rm NN}}$ = 5.02 TeV”**

J. Adam,...,P. Sahoo *et al.* (ALICE Collaboration), Eur. Phys. J. C **76**, 245 (2016)

100. **"Multiplicity dependence of charged pion, kaon, and (anti)proton production at large transverse momentum in p-Pb collisions at $\sqrt{s_{\rm NN}}$ = 5.02 TeV"**
J. Adam,...,P. Sahoo *et al.* (ALICE Collaboration), Phys. Lett. B **760**, 720 (2016)

101. **"Multipion Bose-Einstein correlations in pp,p -Pb, and Pb-Pb collisions at energies available at the CERN Large Hadron Collider"**
J. Adam,...,P. Sahoo *et al.* (ALICE Collaboration), Phys. Rev. C **93**, 054908 (2016)

102. **"Multi-strange baryon production in p-Pb collisions at $\sqrt{s_{\mathbf{NN}}} = 5.02$ TeV"**
J. Adam,...,P. Sahoo *et al.* (ALICE Collaboration), Phys. Lett. B **758**, 389 (2016)

103. **"Centrality dependence of the charged-particle multiplicity density at midrapidity in Pb-Pb collisions at $\sqrt{s_{\rm NN}}$ = 5.02 TeV"**
J. Adam,...,P. Sahoo *et al.* (ALICE Collaboration), Phys. Rev. Lett. **116**, 222302 (2016)

104. **"Charge-dependent flow and the search for the chiral magnetic wave in Pb-Pb collisions at $\sqrt{s_{\rm NN}}$ = 2.76 TeV"**
J. Adam,...,P. Sahoo *et al.* (ALICE Collaboration), Phys. Rev. C **93**, 044903 (2016)

105. **"Measurement of an excess in the yield of J/ψ at very low $p_{\rm T}$ in Pb-Pb collisions at $\sqrt{s_{\rm NN}}$ = 2.76 TeV"**
J. Adam,...,P. Sahoo *et al.* (ALICE Collaboration), Phys. Rev. Lett. **116**, 222301 (2016)

106. **“Pseudorapidity and transverse-momentum distributions of charged particles in proton–proton collisions at $\sqrt{s}$ = 13 TeV”**

J. Adam,...,P. Sahoo *et al.* (ALICE Collaboration), Phys. Lett. B **753**, 319 (2016)

107. **“Inclusive quarkonium production at forward rapidity in pp collisions at $\sqrt{s} = 8$ TeV”**

J. Adam,...,P. Sahoo *et al.* (ALICE Collaboration), Eur. Phys. J. C **76**, 184 (2016)

108. **“Charged-particle multiplicities in proton–proton collisions at $\sqrt{s} = 0.9$ to 8 TeV”**

J. Adam,...,P. Sahoo *et al.* (ALICE Collaboration), Eur. Phys. J. C **77**, 33 (2017)

109. **“Measurement of electrons from heavy-flavour hadron decays in p-Pb collisions at $\sqrt{s_{\rm NN}}$ = 5.02 TeV”**

J. Adam,...,P. Sahoo *et al.* (ALICE Collaboration), Phys. Lett. B **754**, 81 (2016)

110. **“Azimuthal anisotropy of charged jet production in $\sqrt{s_{\rm NN}}$ = 2.76 TeV Pb-Pb collisions”**

J. Adam,...,P. Sahoo *et al.* (ALICE Collaboration), Phys. Lett. B **753**, 511 (2016)

111. **“Direct photon production in Pb-Pb collisions at $\sqrt{s_{\rm NN}}$ = 2.76 TeV”**

J. Adam,...,P. Sahoo *et al.* (ALICE Collaboration), Phys. Lett. B **754**, 235 (2016)

112. **“Centrality evolution of the charged-particle pseudorapidity density over a broad pseudorapidity range in Pb-Pb collisions at $\sqrt{s_{\rm NN}}$ = 2.76 TeV”**

J. Adam,...,P. Sahoo *et al.* (ALICE Collaboration), Phys. Lett. B **754**, 373 (2016)

113. **"Measurement of D_s^+ production and nuclear modification factor in Pb-Pb collisions at $\sqrt{\mathrm{s_{NN}}} = 2.76$ TeV"**
J. Adam,...,P. Sahoo *et al.* (ALICE Collaboration), JHEP **1603**, 082 (2016)

114. **"Multiplicity and transverse momentum evolution of charge-dependent correlations in pp, p–Pb, and Pb–Pb collisions at the LHC"**
J. Adam,...,P. Sahoo *et al.* (ALICE Collaboration), Eur. Phys. J. C **76**, 86 (2016)

115. **"Transverse momentum dependence of D-meson production in Pb-Pb collisions at $\sqrt{\mathrm{s_{NN}}} = 2.76$ TeV"**
J. Adam,...,P. Sahoo *et al.* (ALICE Collaboration), JHEP **1603**, 081 (2016)

116. **"Coherent ψ(2S) photo-production in ultra-peripheral Pb Pb collisions at $\sqrt{s}_{\mathrm{NN}} = 2.76$ TeV"**
J. Adam,...,P. Sahoo *et al.* (ALICE Collaboration), Phys. Lett. B **751**, 358 (2015)

117. **"Precision measurement of the mass difference between light nuclei and anti-nuclei"**
J. Adam,...,P. Sahoo *et al.* (ALICE Collaboration), Nature Phys. **11**, 811 (2015)

118. **"Study of cosmic ray events with high muon multiplicity using the ALICE detector at the CERN Large Hadron Collider"**
J. Adam,...,P. Sahoo *et al.* (ALICE Collaboration), JCAP **1601**, 032 (2016)

119. **"Centrality dependence of pion freeze-out radii in Pb-Pb collisions at $\sqrt{s}_{NN} = 2.76$ TeV"**
J. Adam,...,P. Sahoo *et al.* (ALICE Collaboration), Phys. Rev. C **93**, 024905 (2016)

120. **"Event shape engineering for inclusive spectra and elliptic flow in Pb-Pb collisions at $\sqrt{s_{\rm NN}} = 2.76$ TeV"**
J. Adam,...,P. Sahoo *et al.* (ALICE Collaboration), Phys. Rev. C **93**, 034916 (2016)

121. **"Elliptic flow of muons from heavy-flavour hadron decays at forward rapidity in Pb–Pb collisions at $\sqrt{s_{\rm NN}} = 2.76$ TeV"**
J. Adam,...,P. Sahoo *et al.* (ALICE Collaboration), Phys. Lett. B **753**, 41 (2016)

122. **"Production of light nuclei and anti-nuclei in pp and Pb-Pb collisions at energies available at the CERN Large Hadron Collider"**
J. Adam,...,P. Sahoo *et al.* (ALICE Collaboration), Phys. Rev. C **93**, 024917 (2016)

123. **"ϕ-meson production at forward rapidity in p-Pb collisions at $\sqrt{s_{\rm NN}}$ = 5.02 TeV and in pp collisions at $\sqrt{s}$ = 2.76 TeV"**
J. Adam,...,P. Sahoo *et al.* (ALICE Collaboration), Phys. Lett. B **768**, 203 (2017)

124. **"Centrality dependence of inclusive J/ψ production in p-Pb collisions at $\sqrt{s_{\rm NN}} = 5.02$ TeV"**
J. Adam,...,P. Sahoo *et al.* (ALICE Collaboration), JHEP **1511**, 127 (2015)

125. **"Differential studies of inclusive J/ψ and psi(2S) production at forward rapidity in Pb-Pb collisions at $\sqrt{s_{\rm NN}} = 2.76$ TeV"**
J. Adam,...,P. Sahoo *et al.* (ALICE Collaboration), JHEP **1605**, 179 (2016)

126. **"$^{3}_{\Lambda}\mathrm{H}$ and $^{3}_{\bar{\Lambda}}\overline{\mathrm{H}}$ production in Pb-Pb collisions at $\sqrt{s_{\rm NN}}$ = 2.76 TeV"**
J. Adam,...,P. Sahoo *et al.* (ALICE Collaboration), Phys. Lett. B **754**, 360 (2016)

127. **“Forward-central two-particle correlations in p-Pb collisions at $\sqrt{s_{\rm NN}}$ = 5.02 TeV”**
J. Adam,...,P. Sahoo *et al.* (ALICE Collaboration), Phys. Lett. B **753**, 126 (2016)

128. **“One-dimensional pion, kaon, and proton femtoscopy in Pb-Pb collisions at $\sqrt{s_{\rm NN}}$ =2.76 TeV”**
J. Adam,...,P. Sahoo *et al.* (ALICE Collaboration), Phys. Rev. C **92**, 054908 (2015)

129. **“Search for weakly decaying $\overline{\Lambda \mathrm{n}}$ and $\Lambda\Lambda$ exotic bound states in central Pb-Pb collisions at $\sqrt{s_{\rm NN}}$ = 2.76 TeV”**
J. Adam,...,P. Sahoo *et al.* (ALICE Collaboration), Phys. Lett. B **752**, 267 (2016)

130. **“Centrality dependence of the nuclear modification factor of charged pions, kaons, and protons in Pb-Pb collisions at $\sqrt{s_{\rm NN}} = 2.76$ TeV”**
J. Adam,...,P. Sahoo *et al.* (ALICE Collaboration), Phys. Rev. C **93**, 034913 (2016)

131. **“Centrality dependence of high-p$_T$ D meson suppression in Pb-Pb collisions at $\sqrt{s_{\rm NN}} = 2.76$ TeV”**
J. Adam,...,P. Sahoo *et al.* (ALICE Collaboration), JHEP **1511**, 205 (2015)

132. **“Measurement of jet quenching with semi-inclusive hadron-jet distributions in central Pb-Pb collisions at $\sqrt{s_{\rm NN}} = 2.76$ TeV”**
J. Adam,...,P. Sahoo *et al.* (ALICE Collaboration), JHEP **1509**, 170 (2015)

133. **“Measurement of charm and beauty production at central rapidity versus charged-particle multiplicity in proton-proton collisions at $\sqrt{s} = 7$ TeV”**

J. Adam,...,P. Sahoo *et al.* (ALICE Collaboration), JHEP **1509**, 148 (2015)

134. **"Inclusive, prompt and non-prompt J/ψ production at mid-rapidity in Pb-Pb collisions at $\sqrt{s_{\rm NN}}$ = 2.76 TeV"**
J. Adam,...,P. Sahoo *et al.* (ALICE Collaboration), JHEP **1507**, 051 (2015)

135. **"Measurement of pion, kaon and proton production in proton–proton collisions at $\sqrt{s} = 7$ TeV"**
J. Adam,...,P. Sahoo *et al.* (ALICE Collaboration), Eur. Phys. J. C **75**, 226 (2015)

136. **"Coherent ρ^0 photoproduction in ultra-peripheral Pb-Pb collisions at $\sqrt{s_{\rm NN}} = 2.76$ TeV"**
J. Adam,...,P. Sahoo *et al.* (ALICE Collaboration), JHEP **1509**, 095 (2015)

137. **"Rapidity and transverse-momentum dependence of the inclusive J/ψ nuclear modification factor in p-Pb collisions at $\sqrt{s_{N\ N}}$ = 5.02 TeV"**
J. Adam,...,P. Sahoo *et al.* (ALICE Collaboration), JHEP **1506**, 055 (2015)

138. **"Measurement of dijet k_T in p–Pb collisions at $\sqrt{s}_{NN}$=5.02 TeV"**
J. Adam,...,P. Sahoo *et al.* (ALICE Collaboration), Phys. Lett. B **746**, 385 (2015)

139. **"Measurement of charged jet production cross sections and nuclear modification in p-Pb collisions at $\sqrt{s_{\rm NN}} = 5.02$ TeV"**
J. Adam,...,P. Sahoo *et al.* (ALICE Collaboration), Phys. Lett. B **749**, 68 (2015)

140. **"Measurement of jet suppression in central Pb-Pb collisions at $\sqrt{s_{\rm NN}}$ = 2.76 TeV"**

J. Adam,...,P. Sahoo *et al.* (ALICE Collaboration), Phys. Lett. B **746**, 1 (2015)

141. **"Two-pion femtoscopy in p-Pb collisions at $\sqrt{s_{\rm NN}} = 5.02$ TeV"**
J. Adam,...,P. Sahoo *et al.* (ALICE Collaboration), Phys. Rev. C **91**, 034906 (2015)

142. **"Forward-backward multiplicity correlations in pp collisions at $\sqrt{s}$ = 0.9, 2.76 and 7 TeV"**
J. Adam,...,P. Sahoo *et al.* (ALICE Collaboration), JHEP **1505**, 097 (2015)

143. **"Centrality dependence of particle production in p-Pb collisions at $\sqrt{s_{\rm NN}}$= 5.02 TeV"**
J. Adam,...,P. Sahoo *et al.* (ALICE Collaboration), Phys. Rev. C **91**, 064905 (2015)

144. **"Inclusive photon production at forward rapidities in proton-proton collisions at $\sqrt{s}$ = 0.9, 2.76 and 7 TeV"**
B. B. Abelev,...,P. Sahoo *et al.* (ALICE Collaboration), Eur. Phys. J. C **75**, 146 (2015)

145. **"Charged jet cross sections and properties in proton-proton collisions at $\sqrt{s} = 7$ TeV"**
B. B. Abelev,...,P. Sahoo *et al.* (ALICE Collaboration), Phys. Rev. D **91**, 112012 (2015)

146. **"Production of inclusive Υ(1S) and Υ(2S) in p-Pb collisions at $\sqrt{\rm s_{NN}} = 5.02$ TeV"**
B. B. Abelev,...,P. Sahoo *et al.* (ALICE Collaboration), Phys. Lett. B **740**, 105 (2015)

147. **"Event-by-event mean $p_{\rm T}$ fluctuations in pp and Pb-Pb collisions at the LHC"**
B. B. Abelev,...,P. Sahoo *et al.* (ALICE Collaboration), Eur. Phys. J. C **74**, 3077 (2014)

148. **"Exclusive** J/ψ **photoproduction off protons in ultra-peripheral p-Pb collisions at** $\sqrt{s_{\rm NN}} = 5.02$ **TeV"**
B. B. Abelev,...,P. Sahoo *et al.* (ALICE Collaboration), Phys. Rev. Lett. **113**, 232504 (2014)

149. **"Multiplicity dependence of jet-like two-particle correlation structures in p–Pb collisions at** $\sqrt{s_{NN}}$**=5.02 TeV"**
B. B. Abelev,...,P. Sahoo *et al.* (ALICE Collaboration), Phys. Lett. B **741**, 38 (2015)

150. **"Production of** $\Sigma(1385)^{\pm}$ **and** $\Xi(1530)^{0}$ **in proton-proton collisions at** $\sqrt{s}$ = **7 TeV"**
B. B. Abelev,...,P. Sahoo *et al.* (ALICE Collaboration), Eur. Phys. J. C **75**, 1 (2015)

151. **"Multiparticle azimuthal correlations in p -Pb and Pb-Pb collisions at the CERN Large Hadron Collider"**
B. B. Abelev,...,P. Sahoo *et al.* (ALICE Collaboration), Phys. Rev. C **90**, 054901 (2014)

152. **"Elliptic flow of identified hadrons in Pb-Pb collisions at** $\sqrt{s_{\rm NN}} = 2.76$ **TeV"**
B. B. Abelev,...,P. Sahoo *et al.* (ALICE Collaboration), JHEP **1506**, 190 (2015)

153. **"Suppression of** $\Upsilon(1S)$ **at forward rapidity in Pb-Pb collisions at** $\sqrt{s_{\rm NN}} = 2.76$ **TeV"**
B. B. Abelev,...,P. Sahoo *et al.* (ALICE Collaboration), Phys. Lett. B **738**, 361 (2014)

154. **"Beauty production in pp collisions at** $\sqrt{s}$ = **2.76 TeV measured via semi-electronic decays"**
B. B. Abelev,...,P. Sahoo *et al.* (ALICE Collaboration), Phys. Lett. B **738**, 97 (2014)

155. **"Measurement of electrons from semileptonic heavy-flavor hadron decays in** pp **collisions at** $\sqrt{s} = 2.76$ **TeV"**

B. B. Abelev,...,P. Sahoo *et al.* (ALICE Collaboration), Phys. Rev. D **91**, 012001 (2015)

156. **“Suppression of ψ(2S) production in p-Pb collisions at $\sqrt{s_{\rm NN}}$ = 5.02 TeV”**
B. B. Abelev,...,P. Sahoo *et al.* (ALICE Collaboration), JHEP **1412**, 073 (2014)

157. **“Neutral pion production at midrapidity in pp and Pb-Pb collisions at** $\sqrt{s_{\rm NN}} = 2.76\,\rm TeV$**”**
B. B. Abelev,...,P. Sahoo *et al.* (ALICE Collaboration), Eur. Phys. J. C **74**, 3108 (2014)

158. **“Measurement of prompt D-meson production in $p-Pb$ collisions at $\sqrt{s_{NN}}$ = 5.02 TeV”**
B. B. Abelev,...,P. Sahoo *et al.* (ALICE Collaboration), Phys. Rev. Lett. **113**, 232301 (2014)

159. **“Transverse momentum dependence of inclusive primary charged-particle production in p-Pb collisions at** $\sqrt{s_{\rm NN}} = 5.02$ **TeV”**
B. B. Abelev,...,P. Sahoo *et al.* (ALICE Collaboration), Eur. Phys. J. C **74**, 3054 (2014)

160. **“Azimuthal anisotropy of D meson production in Pb-Pb collisions at** $\sqrt{s_{\rm NN}} = 2.76$ **TeV”**
B. B. Abelev,...,P. Sahoo *et al.* (ALICE Collaboration), Phys. Rev. C **90**, 034904 (2014)

161. **“Measurement of visible cross sections in proton-lead collisions at $\sqrt{s_{\rm NN}}$ = 5.02 TeV in van der Meer scans with the ALICE detector”**
B. B. Abelev,...,P. Sahoo *et al.* (ALICE Collaboration), JINST **9**, P11003 (2014)

162. **“Freeze-out radii extracted from three-pion cumulants in pp, p–Pb and Pb–Pb collisions at the LHC”**

B. B. Abelev,...,P. Sahoo *et al.* (ALICE Collaboration), Phys. Lett. B **739**, 139 (2014)

163. **"$K^*(892)^0$ and $\phi(1020)$ production in Pb-Pb collisions at $\sqrt{sNN}$ = 2.76 TeV"**
B. B. Abelev,...,P. Sahoo *et al.* (ALICE Collaboration), Phys. Rev. C **91**, 024609 (2015)

164. **"Measurement of quarkonium production at forward rapidity in pp collisions at $\sqrt{s} = 7$ TeV"**
B. B. Abelev,...,P. Sahoo *et al.* (ALICE Collaboration), Eur. Phys. J. C **74**, 2974 (2014)

165. **"Performance of the ALICE Experiment at the CERN LHC"**
B. B. Abelev,...,P. Sahoo *et al.* (ALICE Collaboration), Int. J. Mod. Phys. A **29**, 1430044 (2014)

Conference proceedings:

1. **"Study of Thermodynamic and. Transport Properties of Strongly Interacting matter in a Color String Percolation Model at RHIC"**

   P. Sahoo, S. K. Tiwari, S. De and R. Sahoo, DAE Symp. Nucl. Phys. **62**, 884 (2017).

2. **"The q-Statistics and QCD Thermodynamics at LHC"**

   T. Bhattacharyya, A. Khuntia, P. Sahoo, P. Garg, P. Pareek, R. Sahoo and J. Cleymans, Acta Phys. Polon. Supp. **9**, 177 (2016)

3. **"Speed of Sound in a System Approaching Thermodynamic Equilibrium"**

   A. Khuntia, P. Sahoo, P. Garg, R. Sahoo and J. Cleymans, DAE Symp. Nucl. Phys. **61**, 842 (2016).

4. **"Hard scattering contribution to particle production in high energy heavy-ion collisions"**

   P. Pareek, A. N. Mishra, P. Sahoo and R. Sahoo, DAE Symp. Nucl. Phys. **59**, 738 (2014).

Contents

Figures

Tables

Chapter 1

Introduction

"The scientist only imposes two things, namely truth and sincerity, imposes them upon himself and upon other scientists."

– Erwin Schrödinger

This thesis deals with resonance production in high energy pp collisions at the Large Hadron Collider (LHC) facility and study of particle production in color string percolation approach. To understand the philosophy of the work presented in this thesis, we start with a brief description of Standard Model, Quantum Chromodynamics (QCD) and Quark Gluon Plasma (QGP) and its signatures. Afterwards, the motivation for carrying out various measurements related to resonance production in ultra-relativistic pp and A+A collisions at LHC are discussed. Then the motivation for the study of the phenomenological work on particle production using color string percolation model is covered in this chapter along with the hypothesis of limiting fragmentation for particle production in high-energy nuclear collisions.

1.1 The Standard model

The basic questions are always been asked by the mankind that, "What are the constituents of matter and what are their properties?". Many experiments are done to explain it and demonstrate the atom, its subatomic particles called nucleons (such as protons and neutrons) and further constituents of nucleons are called quarks. Quarks and gluons combinely called partons. As the search turned to go into smaller scales, experiments needed to become even larger in the form of high-energy particle accelerators. On the pursuit of these fundamental questions numerous scientific fields are created. These fields include Quantum Mechanics, Quantum Chromodynamics (QCD), Quantum Electrodynamics (QED), Electro-Weak Theory (EWT), High-Energy Physics, and Particle Physics [1].

The Standard model of particle physics is a theoretical attempt to explain the fundamental properties of matter and their interaction, which was developed mostly by Glashow, Salam and Wienberg in 1970s [2–4]. According to this model, both the elementary fermions like quarks and leptons are classified in three families or generations each, as shown in Fig. 1.1. The up (u) and down (d) quarks belong to the first family. The charm (c) and strange (s) quarks; top (t) and bottom (b) quarks belong to second and third family of the standard model, respectively. The leptons are also categorised in the same way into three generations, electron, muon and tau and their corresponding neutrinos. The fermions (leptons and quarks) and their corresponding anti-particles have half integral spin quantum number. The fermions obey Fermi-Dirac statistics and Pauli's exclusion principle. The four fundamental forces in nature for the existence of the universe are:

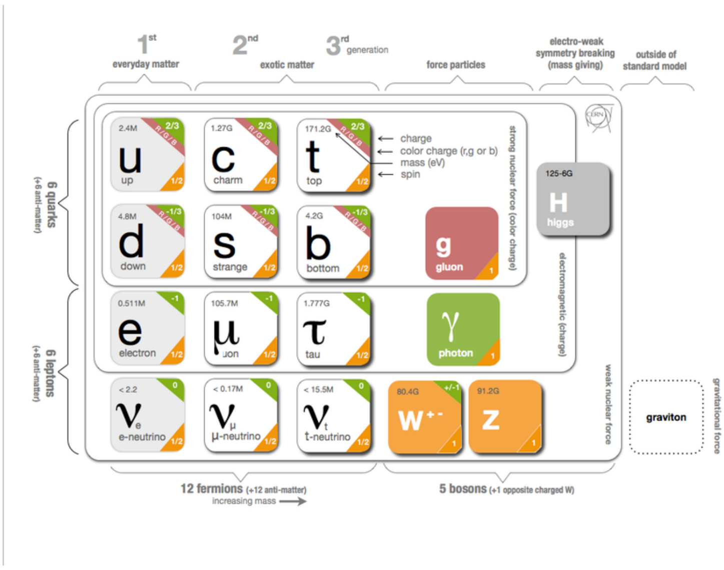

Figure 1.1: The Standard model of particle physics (Image Credit: CERN).

(i) Strong (ii) Weak (iii) Electromagnetic and (iv) Gravitational forces. All the fundamental forces and their corresponding mediators, which are called gauge bosons are included in the standard model of particle physics except the gravitational force and its mediator, graviton. The gauge bosons (g, γ, $W^{\pm}$, Z^0) from standard model have spin 1. Gluons (g) and γ are the mediator for the strong and electromagnetic interactions, respectively. $W^{\pm}$ and Z^0 bosons are mediator for the weak interactions. We know that the Standard model cannot be the full story as it is unable to explain all the phenomena existing in the Universe. The existence of dark matter, the matter-antimatter asymmetry in our Universe and neutrino masses and oscillations are the main evidences of the existence of physics beyond the Standard model or New physics.

1.2 Quantum chromodynamics (QCD)

The theory of strong interaction is called Quantum Chromodynamics (QCD). It describes the interaction between quarks and gluons which are having the colour quantum numbers. They constitute to form the colourless hadrons. The QCD effective potential, or the so-called Cornell potential between partons is given as,

$$V_{QCD}(r) = -\frac{4}{3}\frac{\alpha_S}{r} + kr, \tag{1.1}$$

where α_S is the strong coupling constant, which is otherwise called as running coupling constant, k is colour string tension constant and r is the distance between interacting partons. The potential indicates that, quarks exhibit the property of color confinement, which means a quark cannot be found in isolation. The effective strength of strong interaction for a physical process is given by the QCD running coupling constant as,

$$\alpha_S(Q^2) = \frac{12\pi}{(33 - 2n_f)ln(Q^2/\Lambda^2_{QCD})}, \tag{1.2}$$

where Q^2 is momentum transfer between quarks or gluons, n_f is the number of quark flavours. And Λ_{QCD} is the scale at which the perturbatively-defined coupling diverges and its value is around 200 MeV. Qualitatively it indicates the order of magnitude at which $\alpha_S(Q^2)$ become strong. As we go low in values of Q the coupling constant $\alpha_S(Q^2)$ grows and perturbation theory breaks down around the scale comparable to the masses of light hadrons, i.e. around 1 GeV. The growth of the coupling at low scales could be an indication of quark and gluon confinement inside hadrons [5]. Confinement is the reason for the bound state of quarks which are called as hadrons. The hadrons particularly, protons and neutrons together with electrons make up of the visible matter of the Universe. With color confinement property, asymptotic freedom is another property of QCD retained for quarks [6]. For the processes with high momentum transfer (large Q^2), the coupling constant becomes small and the quarks and gluons behave as free particles in QCD vacuum. This is known as asymptotic freedom. Figure 1.2 shows behaviour of strong running coupling constant (α_S) with respect to momentum transfer (Q) and the values estimated by different experiments.

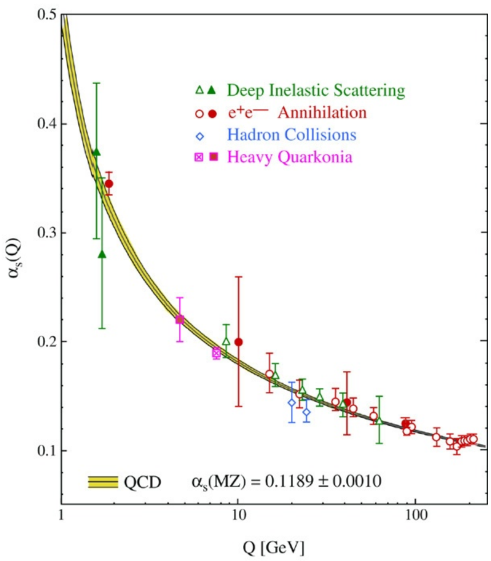

Figure 1.2: QCD running coupling constant (α_S) as a function of momentum transfer (Q) [7].

1.3 Quark gluon plasma (QGP)

From the potential described in the previous section, reveals that, at certain extreme conditions like: high temperatures or high baryon densities the quarks and gluons confined inside hadrons can be de-confined. By increasing the temperature or by compressing, a transition from normal hadronic matter to a novel phase of matter composed of free quarks and gluons can be reached. The de-confined state of quarks and gluons is called as Quark-Gluon Plasma (QGP) [8]. This can be achieved experimentally in the fixed target or collider experiments. In laboratory, QGP can be experimentally created by ultra-relativistic heavy-ion collisions. Lattice-QCD (lQCD) prediction says that, at lower baryon chemical potential, μ_B (which is defined as the amount of energy required to add or remove a baryon from the system) the QCD phase transition from hadronic to partonic phase occurs [9]. The lQCD calculation considering massless quarks and gluons at zero chemical potential ($\mu_B = 0$) and at high-temperature limit, the temperature T dependence of the energy density (ε) scaled by T^4 is shown in Fig 1.3. ε/T^4 is proportional to number of degree of freedom for the sys-

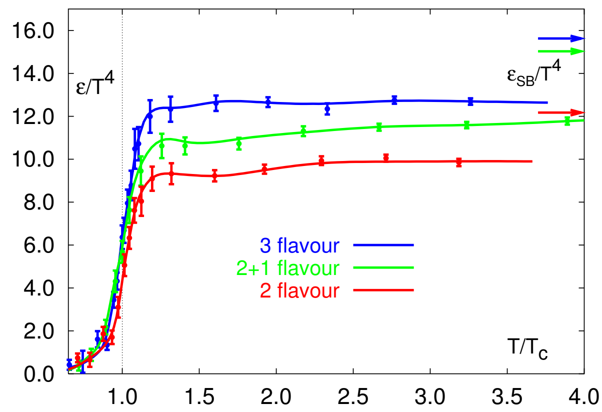

Figure 1.3: lQCD predictions of ε/T^4 as a function of temperature normalized by the critical temperature (T_C). The horizontal arrows show the Stefan-Boltzmann limit [10].

tem. It is observed that at T around critical temperature ($T_C \sim 154$ TeV (for 3 – flavour QCD)) it shows a sharp increase, which slowly saturates at higher temperatures below the Stefan-Boltzmann limit [10]. The equation of state shows three different behaviours depending on the temperature: i) for $T < T_C$, hadron degree of freedom is prominent and partons are confined inside the hadrons, ii) around $T \sim T_C$, an abrupt rise in degrees of freedom of the system is observed which indicates a change of phase, and iii) for $T > T_C$, partons are de-confined, the quarks and gluons can travel in a volume larger than the size of hadrons.

1.3.1 The QCD phase diagram

The conjectured QCD phase diagram for different phases of QCD matter and possible phase transition is shown in Fig. 1.4. One of the most widely studied phase diagram in science is that of water, where electromagnetic interaction is the underlying interaction. A similar phase diagram for a system of strongly interacting matter, based on the strong interaction is also established. This diagram shows variation of temperature (T) versus the baryon chemical potential μ_B. The analysis of particle yields in the heavy-ion collisions and their comparison to statistical models suggests that T and μ_B vary in opposite manner with center-of-mass energy ($\sqrt{s_{NN}}$) at the chemical freeze-out [11]. The μ_B decreases with $\sqrt{s_{NN}}$ while T increases with increase in $\sqrt{s_{NN}}$. By changing the collision energy, one can vary the two axes of the phase diagram, i.e. T and μ_B, and experimentally get access to a large part of the phase space. The Beam Energy Scan (BES) program at the RHIC, BNL has been designed based on the above discussed idea for the study of the phase structure of the QCD phase diagram and in particular the search for a critical point [12, 13]. The phase diagram shows a rich phase structure, in spite of that experimentally only some part is accessible which corresponds to some of the following distinct structures: de-confined phase of quarks and gluons, hadronic phase, critical point and a crossover at low μ_B and very high temperature.

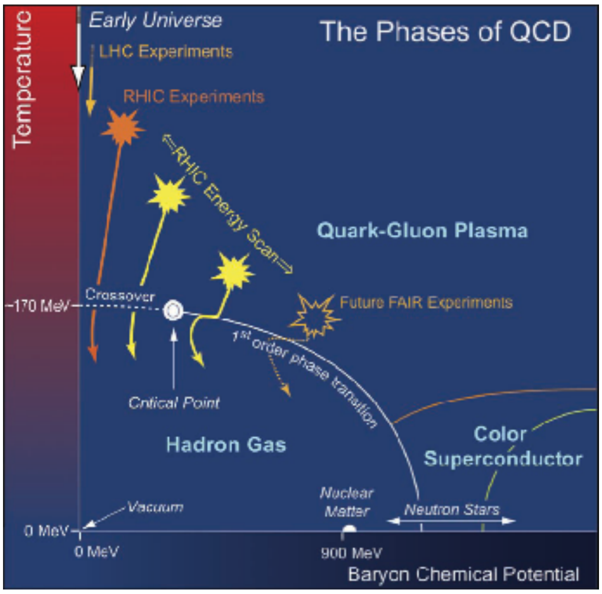

Figure 1.4: Sketch of QCD phase diagram with boundaries that define various states of QCD matter [14].

1.3.2 Ultra-relativistic collisions

The experimental search for de-confined state of quarks and gluons started with the first heavy-ion collisions in Alternating Gradient Synchrotron (AGS) at Relativistic Heavy Ion Collider (RHIC), Brookhaven National Laboratory (BNL) and thereafter in Super Proton Synchrotron (SPS) at the Large Hadron Collider (LHC), previously known as LEP (Large Electron-Proton collider). In the high-energy heavy-ion collision experiments, two nuclei are accelerated in ultra-relativistic velocities, as a result these nuclei get Lorentz contracted along the direction of motion and look like disks. The overlap region of the nuclei depend upon the impact parameter. The impact parameter is the perpendicular distance between the centre of the two colliding nuclei. The nucleons in the overlap region are called participants and those which are outside the overlap region and do not participate in production are called spectators. A schematic diagram of different stages of the heavy-ion collision is shown in Fig. 1.5. Figure 1.6 shows the longitudinal space-time evolution of a relativistic nucleus-nucleus collision, via pre–equilibrium to the formation of final state hadrons. When the nuclei collide, inelastic interactions among partons start. The partons

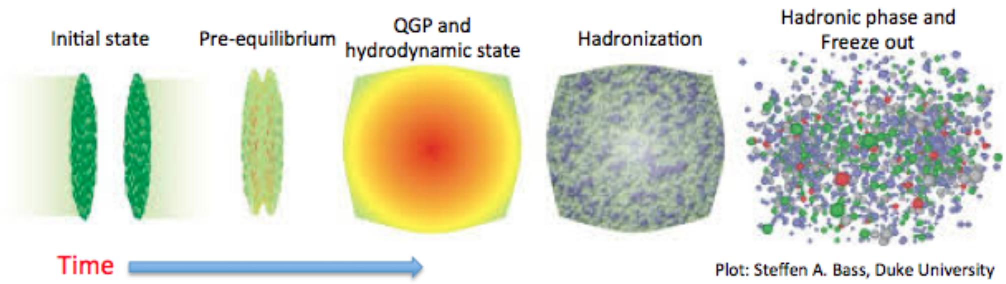

Figure 1.5: A schematic picture of the time evolution of heavy-ion collision. (Image credit: Prof. Steffen A. Bass)

loose energy to form matter, which is created in the vicinity of the collisions and thus the system produced is commonly known as a fireball. Depending on the energy of the colliding nuclei, the participant nucleons are either opaque or transparent to each other. The QGP state is only formed when the fireball has sufficient energy density and temperature.

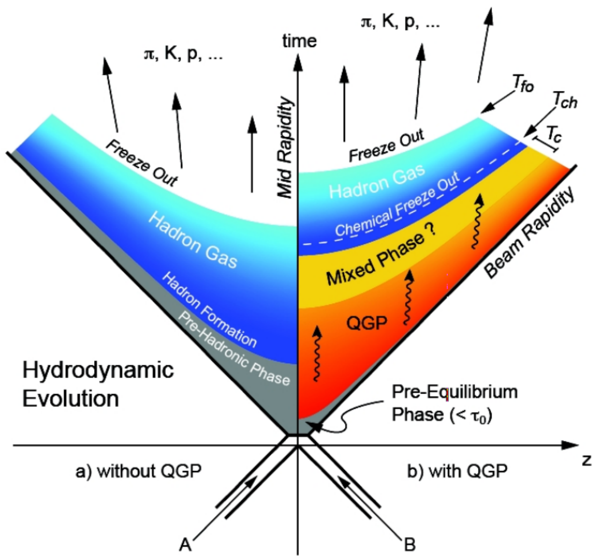

Figure 1.6: A schematic diagram of the longitudinal space-time evolution of relativistic nucleus-nucleus collision [15].

The space-time evolution of ultra–relativistic collisions where there is a possibility of QGP formation and the state without QGP formation is depicted in Fig 1.6. Consider a heavy-ion collision at z = 0, t = 0. In case of high-energy central heavy-ion collisions, which is characterised by the impact parameter ($b \sim 0$), almost all the nucleons involve in the interactions. So, a very hot and dense matter tends to produce. In the right side of the Fig 1.6 it is shown the evolution of the heavy-ion collision in the case of QGP formation is shown.

- **Pre-equilibrium stage:** The inelastic interaction among partons give rise to an abundant production of de-confined quarks and gluons for $t \leq 1\ fm/c$, which is called pre-equllibrium state. High transverse momentum, $p_T \gg 1$ GeV/c particles are produced in this stage. At higher energies such particles can also be produced in subsequent stages.

- **QGP evolution:** When the fireball reaches the critical energy density and temperature, the fully de-confined state of partons form a quark-gluon plasma state. Lattice QCD calculation show that the QGP phase is achieved beyond a critical energy density of 1 GeV/fm^3 or beyond T_C, which is different for 2-flavour and 3-flavour QCD [10]. The elastic and inelastic interactions between partons in QGP lead to the thermalization phase. Due to the inelastic interactions the flavour composition of the system changes. Because of the high internal pressure and temperature, the system begins to expand rapidly and cools down and starts converting into a hadron gas. This is the mixed phase.

- **Hadron gas and freezeout:** When it reaches again the critical energy density, the hadronization begins and quarks and gluons of the QGP matter condensate to produce new hadrons. There are two possible reaction mechanisms for hadronization, one is fragmentation i.e. when a high p_T parton fragments into lower p_T hadrons and another is coalescence through which lower momenta partons combine to form higher p_T hadrons. Hadronization from fragmentation dominates at higher energies, while coalescence at lower energies. Hadrons continue to interact among themselves elastically and inelastically until the chemical freeze-out temperature (T_{ch}). At the chemical freeze-out the inelastic processes cease, chemical composition of the produced particles get fixed i.e. the particle ratios are frozen but they can interact among themselves via elastic scattering. Now when the mean distance between the hadrons become greater than the system size, elastic scatterings between hadrons cease and the transverse momentum spectra of the resulting matter also become fixed. This is called kinetic freeze out and the corresponding temperature is known as kinetic freeze out temperature (T_{fo}). After freeze-out the particles come out of the fireball and are detected by the surrounding detectors.

The left side of the Fig. 1.6 shows, if the matter produced in the heavy-ion or hadron-hadron collisions does not meet the high density/high temperature conditions for QGP formation, the system will is left with only hadronic degrees of freedom. For non-central heavy-ion collisions and low-energy pp collisions this type of evolution is expected to occur. Just after the collisions a pre-hadronic phase is created then the nucleons can recombine into new hadrons. The produced hadrons can be detected after the hadron gas phase freeze-out. The life-time of such a fireball is comparably less than the life-time of the fireball produced in high-energy central heavy-ion collisions.

1.3.3 Signatures of QGP

The produced de-confined QGP medium exists only for a few microseconds. It is nearly impossible to directly observe QGP state within such a small lifetime. However various indirect measurements can be used as diagnostic tools for confirmation of QGP. There is no unique signal which will alone lead to the identification of quark-gluon plasma. Instead, a number of different signals come out from the medium which may be treated as QGP signatures [16]. Certain probes, which are generated prior to the thermalization of the de-confined state, can bring out information about the existence of QGP state and its properties. A Large Ion Collider Experiment (ALICE) [17] at LHC is specifically designed for the creation of QGP and study its properties. Various signatures like jet quenching, azimuthal anisotropy, J/ψ suppression, strangeness enhancement of QGP formation are discussed below in details.

- **J/ψ suppression:** The bound state of charmonium quark and its anti-quark, $c\bar{c}$ (J/ψ) is usually formed at the early stages of the hadronic and nuclear collisions. So, the J/ψ becomes an excellent probe to study the early dynamics of the medium formed in heavy-ion collisions. Theoretical calculations suggest that the production of J/ψ in heavy-ion collisions, where a QGP state is expected will be suppressed as compared to pp collisions, where no medium formation is expected to be formed [18]. The QGP medium screen the colour charge of the quark which reduces the J/ψ production. The J/ψ suppression is clearly observed in heavy-ion collisions, whereas the disassociated charm quarks at the same time increases the open charm production ($D^0, D^{\pm}$). The J/ψ suppression is first observed in SPS [19] and then in RHIC [20, 21] energies confirming to the QGP medium formation. Figure 1.7 shows the nuclear modification factor (R_{AA}) of J/ψ meson in Pb–Pb collisions at $\sqrt{s_{NN}}$ = 2.76 TeV and 5.02 TeV as a function of centrality measured in ALICE at LHC. The results of Au+Au collisions at $\sqrt{s_{NN}}$ = 0.2 TeV from the PHENIX collaboration at RHIC is also shown. The suppression in LHC energies is found to be less than that of RHIC and SPS energies [20]. This enhancement in the J/ψ yield at LHC is explained by the recombination of charm quarks during the hadronization process. So the suppression in R_{AA} at $\sqrt{s_{NN}}$ = 5.02 TeV is less compared to $\sqrt{s_{NN}}$ = 2.76 and 0.2 TeV.

- **Strangeness enhancement:** The strange particle production is a probable signal to the formation of QGP, as the strange quantum number is absent in the colliding matter. An enhanced production of strange quarks in heavy-ion collisions compared to hadronic collisions has been proposed as a signature of a QGP medium [22]. The threshold energy for the production of strange hadrons is around 300–400 MeV. Strange particle production mechanism and production rates

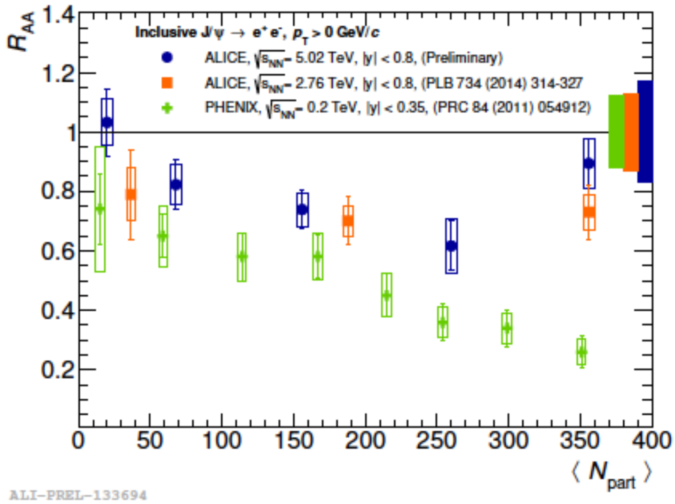

Figure 1.7: The R_{AA} of J/ψ as function of centrality in Pb–Pb collisions at $\sqrt{s_{NN}}$ = 2.76 TeV and 5.02 TeV at ALICE and the measurement is compared with the PHENIX result of Au+Au collisions at $\sqrt{s_{NN}}$ = 0.2 TeV.

are different in a hadron gas as compared to QGP medium. To quantify the strangeness enhancement, one needs to study and compare the abundance of strangeness between plasma and hadronic phases. Due to the high gluon density in QGP, the formation of $s\bar{s}$ pair from the channel $g\bar{g} \to s\bar{s}$ is dominate over annihilation of light quarks, $q\bar{q} \to s\bar{s}$ channel. In contrast to pp collisions, where QGP medium formation is not expected, annihilation of light quarks to strange quark is the main channel for the production of strangeness. The enhancement factor E is defined as,

$$E = \frac{2}{\langle N_{part} \rangle} \left[\frac{\frac{dN^{AA}}{dy}|_{y=0}}{\frac{dN^{pp}}{dy}|_{y=0}} \right]. \tag{1.3}$$

Here $\langle N_{part} \rangle$ is the number of participants, which is a measure of collision centrality. $\frac{dN^{AA}}{dy}|_{y=0}$ and $\frac{dN^{pp}}{dy}|_{y=0}$ are the yields in heavy-ion and pp collisions, respectively. In Fig. 1.8 the yield of hyperons enhancement factor (E) as a function of centrality $N_{\rm part}$ is shown for ALICE [23] and is compared with measurements from STAR and NA57 collaborations [24, 25]. The observed abundant production of

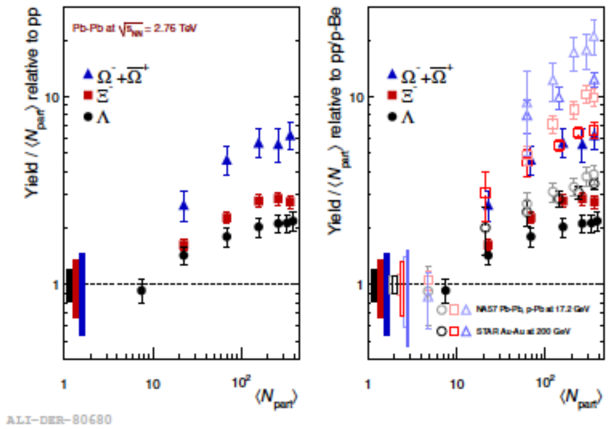

Figure 1.8: The yield of multi-strange hadrons in Pb-Pb relative to pp collisions measured in ALICE (left panel) and NA57, STAR (right panel) as function of centrality, $\langle N_{\rm part} \rangle$) [23–25].

strange particle in Pb–Pb with respect to pp and p–Be collisions indicates the formation of de-confined state of matter in LHC energies. It is also found out that the enhancement factor is higher for particles containing more strange quark i.e. $E(\Lambda) < E(\Xi) < E(\Omega)$ [23–25].

- **Jet quenching:** One of the most exciting results obtained at RHIC with a hint of QGP medium formation is the discovery of suppression in the production of high transverse momentum (p_T) mesons. In relativistic heavy-ion collisions, when a partons from colliding nucleus interacts, then various partons with very high-p_T are produced which fly off to all possible directions from the collision points and finally fragment into narrow cones of hadrons, called jets. These highly energetic shower of secondary quarks, antiquarks and gluons are commonly referred as jet. When some of these jet partons enter in the thermalized QGP type of medium, they interact with the medium particles and loose energies and momenta before hadronizing. The suppression is observed in nucleus-nucleus collisions compared to corresponding data from pp collisions scaled with the number of binary collisions [26, 27]. This phenomena is called as the jet quenching and has been interpreted in terms of energy loss of partons in QGP. The high-p_T partons are created early in the collisions carrying large energy. The energy loss by these energetic partons traversing the hot and dense medium formed is predicted to be proportional to both the initial gluon density [28, 29] and the lifetime of the dense matter [30]. The suppression of high-p_T mesons are usually expressed in terms of the nuclear modification factor (R_{AA}),

$$R_{AA}(p_T) = \frac{1}{\langle T_{AA} \rangle} \times \left[\frac{(\frac{d^2N}{dp_T dy})_{AA}}{(\frac{d^2N}{dp_T dy})_{pp}} \right]. \tag{1.4}$$

This is the ratio between the invariant yield in nuclear-nuclear (A+A) collisions to that of pp collisions scaled with the average nuclear overlap function, $\langle T_{AA} \rangle = \langle N_{coll} \rangle / \sigma_{inel}$, where $\langle N_{coll} \rangle$ and σ_{inel} are number of binary collisions and inelastic pp cross section, respectively. $R_{AA} = 1$, suggests that the nuclear collisions are simply linear superposition of pp collisions and there is no QGP medium formation. However, any deviation from the unity value at high-p_T is an indication of quenching in high-density medium.

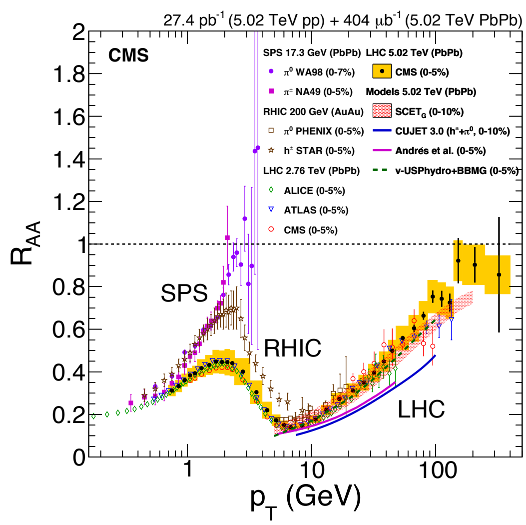

Figure 1.9: $R_{AA}(p_T)$ for neutral pions (π^0), charged hadrons ($h^{\pm}$), and charged particles in central heavy-ion collisions at SPS, RHIC and the LHC [31].

In Fig. 1.9 the combined results of R_{AA} for Au+Au and Pb+Pb collisions are shown. The high-p_T suppression of hadrons in dense QGP medium is shown along with results of jet quenching in both RHIC and LHC energies. They are compared with theoretical predications. Any primordial high-p_T parton losses its energy while passing through the hot dense medium causing high-p_T suppression in heavy-ion collisions [31].

- **Elliptic flow and QGP:** Elliptic flow is another important observable to understand the collective behaviour of the system and is also sensitive to the initial condition and degrees of freedom in the fireball. So, the collective expansion of matter created in ultra-relativistic collisions due to presence of pressure gradients which results from the spatial anisotropy of the initial density profile resulting in final state momentum anisotropy. This phenomenon is called collective flow. The azimuthal momentum anisotropy is defined as the fourier expansion in the azimuthal angle ϕ as [32, 33],

$$\frac{dN}{p_T dp_T d\phi dy} = \frac{dN}{2\pi p_T dp_T d\phi dy}\left[1 + 2\sum_{1}^{\infty} v_n cos[n(\phi - \psi)]\right]. \quad (1.5)$$

Where v_n's are various order of flow harmonics, v_1 is the directed flow, v_2 is the elliptic flow, v_3 is triangular flow and so on. And ψ is orientation of reaction plane. Reaction plane is the plane formed by the beam direction and impact parameter vector.

The differential elliptic flow of charged particles presented in left panel of Fig. 1.10 shows that, the dense media produced at RHIC and LHC are of similar nature. The 30% higher value of v_2 at LHC is due to availability of larger phase space which increases the high-p_T particles at LHC. The large elliptic flow suggests larger rescattering among partons. This also indicates an early thermalization of high-p_T partons. All these evidence signifies a strong signature for formation of QGP. Right panel of Fig. 1.10 shows the v_2 scaled with the number of constituent quarks (NCQ) as a function of $(m_T - m_0)/n_q$, where $m_T = \sqrt{{m_0}^2 + {p_T}^2}$ and m_0 is the rest mass for different identified particles in minimum bias Au+Au collisions at $\sqrt{s_{NN}} = 62.4$ GeV measured in STAR [34]. Form all v_2 to fit function ratios the number

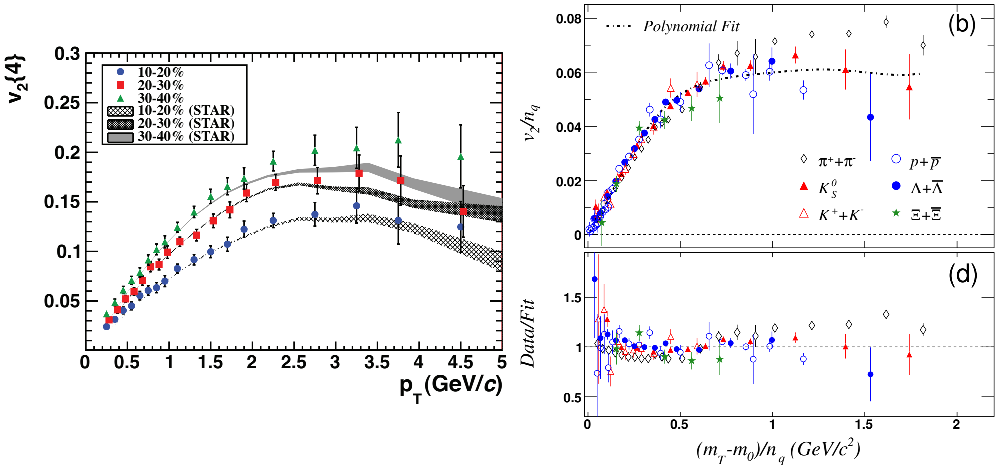

Figure 1.10: Left: The differential elliptic flow of charged particles. The Pb + Pb collisions at $\sqrt{s_{NN}} = 2.76$ TeV shown in coloured symbols are compared to Au+Au collisions at $\sqrt{s_{NN}} = 200$ GeV, which are in shaded regions [31]. Right: v_2/n_q versus $(m_T - m_0)/n_q$ of identified hadrons in Au+Au collisions at $\sqrt{s_{NN}} = 62.4$ GeV [34].

of constituent quark scaling is observed, which suggests hadron formation via quark coalescence. The NCQ scaling of v_2 says that, the relevant degrees of freedom in the early system may be sub-hadronic (e.g. constituent quarks). It also puts light on the strongly coupled matter with sub-hadronic degrees of freedom which may be created in heavy-ion collisions at RHIC [35–37].

- **Electromagnetic Probes:** Photons and di-leptons are used as electromagnetic probes, to get more information about the QGP properties [38–40]. As they do not have strong final state interactions, so they act as an ideal penetrating probe of strongly-interacting QCD matter [41]. In the heavy-ion collisions the photons and di-leptons can be produced in the initial hard collisions by the various processes like: annihilation ($q\bar{q} \rightarrow \gamma g, q\bar{q} \rightarrow \gamma\gamma$), Bremsstrahlung ($qg \rightarrow gq^* \rightarrow q\gamma g$), fragmentation ($qg \rightarrow qg^* \rightarrow q\gamma X$), compton ($qg \rightarrow \gamma q$) and pair production ($q\bar{q} \rightarrow l\bar{l}$) or they are radiated from the partons and hadrons in thermal equilibrium or via the decay of hadrons. Except the decay photons, others are called direct/prompt photons. The high-p_T isolated direct photons can be used for calculation of the momentum of the associated partons, which allows to study the parton energy loss in the medium. The information of the initial state and its possible modifications in nuclei is carried by the prompt photons. Hence they can be used as probes of gluon saturation. The thermal photons are emitted in the dense matter and carry the temperature information of QGP.

The properties of the QGP medium created at RHIC and LHC need more understanding. The dynamics of resonance production can be used as a powerful tool to understand the QGP medium formed at the LHC, which is one of the main motivations of this thesis work. The details will be discussed in the next sections.

1.4 Resonance production in ALICE at LHC

Resonance particles are extremely short lived particles and they decay via the strong interaction. The lifetime of these particles are of the order of 10^{-23} seconds or $\tau \sim 1$ fm/c. These particles could only fly upto 10^{-15} meters or say about the diameter of a proton, before decaying. The typical lifetime of the resonances measured experimentally in heavy-ion collisions varies from 1 – 47 fm/c . The lifetime of the fireball created in heavy-ion collisions at LHC is $\mathcal{O} \sim 10$ fm/c [42]. So, the resonances can be used as excellent probes for the study of system evolution in different time scales and to understand various in-medium phenomena.

In this thesis, $K^{*\pm}$ resonance is studied in details. $K^{*\pm}$ is a vector meson (spin 1) containing a strange quark and having lifetime, $\tau_{K^{*\pm}} \sim$ 4.0 fm/c [43], which is comparable to the fireball created in Pb–Pb collisions [42]. Due to this short lifetime of $K^{*\pm}$, it decays to charged pion ($\pi^{\pm}$) and neutral kaon (K^0_S). Again K^0_S undergoes weak decay to two charged pion pair daughters inside the hadronic medium separated between chemical and kinetic freeze-out as shown in the Fig. 1.11. There are mainly three possible cases: (i) $K^{*\pm}$ decays inside the medium but the decay daughters

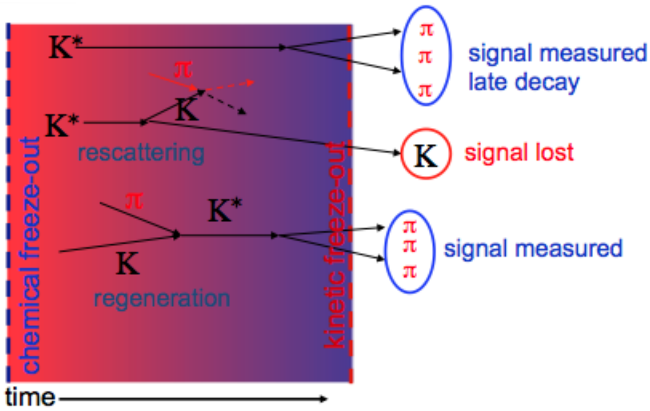

Figure 1.11: Schematic diagram showing chemical and kinetic freeze-out with possible pion and kaon interactions in the hadronic medium.

remain unaffected by the medium particles or called late decay, and signal is measured, (ii) $K^{*\pm}$ decays in the medium and the decay daughters interact with the medium particles which modifies their momenta and the signal is lost and lastly, (iii) in-medium pions and kaons interact among themselves to form the $K^{*\pm}$ resonance state, which must be a fake signal. In the second case, the $K^{*\pm}$ signal is lost from being observed in experiments because of the *re-scattering* of daughter particles. In the last case shown in the figure, the $K^{*\pm}$ yield increases due to the *regeneration* of the in-medium pion and kaon interactions. The parent $K^{*\pm}$, which is reconstructed via invariant mass method is affected due to the interplay of these two competing processes (re-scattering and regeneration). These two processes mainly depend on the in-medium hadron interactions cross sections, chemical and kinetic freeze-out time interval and source size [44, 45]. The re-scattering and regeneration effects can be disentangled and quantified by calculating the resonance to stable particle yield ratios ($K^{*\pm}/K$) in pp and A+A collisions. The ϕ/K ratio also reveals more information as the ϕ mesons have similar masses and spin but very contrasting lifetimes i.e τ_{ϕ} = 46.3 $\pm$ 0.4 fm/c [43] than that of $K^{*\pm}$. That means the ϕ mesons are most unlikely to decay inside the medium and the yield is less affected by re-scattering and regeneration processes.

In particular, the measurement of $K^{*\pm}$ resonance for minimum-bias pp collision at $\sqrt{s} = 5.02$ and 8 TeV is studied in this thesis. A detailed introduction and motivation is also described in chapter 3. The production of resonances with pp collisions at ALICE can be studied to understand the underlying event in the collisions, because a majority of the final state particles originate from these resonances [46]. These can be used to tune QCD inspired models such as PYTHIA [47, 48] and PHOJET [49], which are tuned to LHC energy. Measurements of resonances in the smaller systems like, pp, p+A and d+A collisions serve as baselines for heavy-ion studies and to disentangle between initial and final state effects.

1.5 Color string percolation model (CSPM)

In the early 1990s, several theoretical/phenomenological models correctly estimated the multiplicities and the $\langle p_T \rangle$ of hadrons spectra in pp collisions, which nicely agrees with experimental results [50]. Most of these models used color strings to represent the strong force interactions during collisions. For studying the hadron spectra created in Au+Au collisions, these models were scaled up the results calculated in pp collisions to predict the multiplicities and the $\langle p_T \rangle$ in Au+Au collisions. However, when the model results were compared to the various experimental results in Au+Au collisions, it was found that the observed multiplicity, μ was less than the model predictions, and the $\langle p_T \rangle$ was higher than the models estimates. A string fusion model is one of the first models to correctly account for this discrepancy [51]. Figure. 1.12 and Fig. 1.13 show the agreement of the model predictions of multiplicities and transverse momentum spectra for Au+Au collisions at $\sqrt{s_{NN}} = 130$ and 200 GeV. This model allows the color strings to interact with one another and proposes that this interaction modifies the total color charge present in the collision. It has again evolved into the Color String Percolation Model (CSPM), which uses a string fusion scenario and relates it to a phase transition predicted by percolation theory.

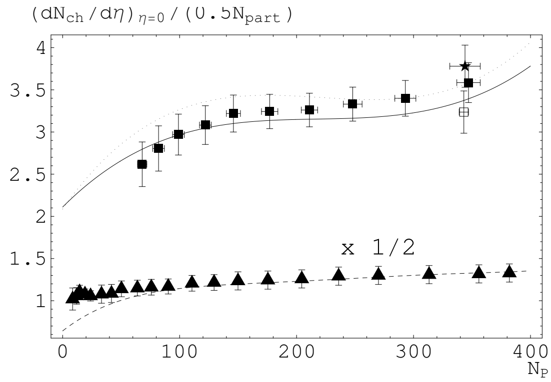

Figure 1.12: Results of color string percolation model predicting multiplicity. The number of participants are from the SPS WA98 data (filled triangles), the RHIC PHENIX (filled square), PHOBOS (open square) data at $\sqrt{s_{NN}}$ = 130 GeV, and with RHIC PHENIX data at $\sqrt{s_{NN}}$ = 200 GeV (filled stars). The dashed, solid, and dotted lines are predictions for the relevant energies [51].

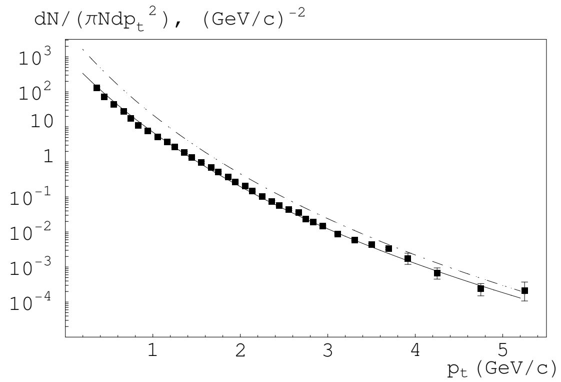

Figure 1.13: Results of color string percolation model predicting transverse momentum. The solid line corresponds to the expected p_T distribution with CSPM for most central (0 - 5%) Au+Au collisions. The filled boxes are the PHENIX experimental data at RHIC. The dotted-dashed line is the expected distribution if color suppression is not accounted for [51].

From all these evidences a genuine interest evolves to study the particle production for heavy-ion collisions at RHIC BES energies in the quest of deeper understanding of QCD matter produced using CSPM. The transition of QCD matter from hadronic confined phase to QGP de-confined phase is fascinating. Theoretically, there are several signatures of first order phase transition and the critical point has also been proposed [52]. One can use the color string percolation approach to investigate the particle production through the percolation of color strings and the phase structure of the hadronic matter [53].

In addition, **thermodynamical and transport quantities** like, energy density, shear viscosity, trace anomaly, speed of sound, entropy density and bulk viscosity of the matter produced in heavy-ion collisions provide unique opportunity to study the fundamental form of matter. According to the linear theory of non-equilibrium thermodynamics for a system slightly away from equilibrium, the thermodynamic fluxes are proportional to the thermodynamic forces. The proportionality constants are known as the transport coefficients [54]. That implies: Thermodynamic flux = Transport coefficient × Thermodynamic force. Like, $Momentum\ (\pi_{ij}) = -Viscosity\ (\eta) \times Gradient\ of\ Velocity\ (\frac{\partial v_i}{\partial x_j})$, $Heat\ (h_i) = -Heat\ conductivity\ (k) \times Gradient\ of\ Temperature\ (\frac{\partial T}{\partial x_i})$ and $Current\ density\ (J_{ij}) = -Electrical\ conductivity\ (\sigma) \times Gradient\ of\ Potential\ (\frac{\partial V_i}{\partial x_j})$ etc. So study of these well known observable for strongly interacting matter produced in heavy-ion collisions using CSPM has drawn considerable interest in this thesis. The energy and centrality dependent study of percolation parameters and various thermodynamical observables at RHIC energies are also examined. In chapter 4 some insight of the percolation theory and its uses in strongly interacting matter is elaborately discussed. The introduction to color string percolation, the string dynamics, relationship between strings and the initial temperature and particle production in CSPM is discussed in details. In addition to it, a detailed formalism and methodology of CSPM is also reviewed.

Apart from these studies, we also have tried to investigate one of the most intriguing topics, multiparticle production in high-energy collisions. A brief introduction and motivation is given in the next section.

1.6 Limiting fragmentation

The hypothesis of limiting fragmentation (LF) or it is called otherwise, as extended longitudinal scaling, is an interesting phenomena in high energy multiparticle production process [55, 56]. The hypothesis says, the produced particles, in the rest frame of one of the projectile become independent of centre of mass energies, thus following a possible scaling (as a function of $\eta' = \eta \pm y_{\mathrm{beam}}$). The observables namely charged particle multiplicity ($\mathrm{N_{ch}}$) and densities of pseudorapidity ($dN_{ch}/d\eta$ and $dE_T/d\eta$), bring important information on the underlying dynamics of strong interactions. It is observed that, the measured values of charged particle pseudorapidity density and elliptic flow were found to be independent of energy over a broad range of pseudorapidities when viewed in the rest frame of one of the colliding nuclei [57]. The photon multiplicity is found to increase from peripheral to central collisions [58], however when the photon pseudorapidity density normalized by $\langle N_{part}/2\rangle$, it shows longitudinal scaling, independent of beam energy and collision centrality as shown in left panel of Fig. 1.14. The charged particles also exhibit energy independent limiting fragmentation behaviour [59]. This has been observed in central Au+Au collisions in BRAHMS and PHOBOS experiments as shown in right panel of the Fig. 1.14. In view of this we have tried to see the LF scaling in differential cross-section per unit pseudorapidity of charged particle ($d\sigma^{AA}/d\eta$) taking the inelastic cross-section (σ_{in}) into account, which is not a constant from lower RHIC energy to highest LHC energy but is a slowly growing function. This hypothesis of limiting fragmentation is studied at the LHC energies taking the energy dependence of σ_{in} and is compared with AMPT model estimations.

1.7 A Multi-phase Transport Model

A Multi-phase Transport Model (AMPT) [60] study is performed to understand the particle production mechanism to examine the extended longitu-

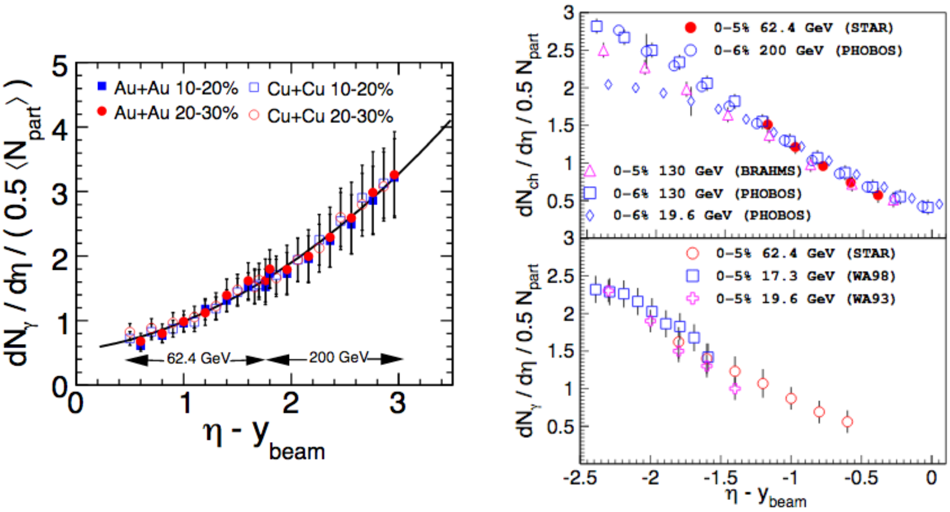

Figure 1.14: Left: Photon pseudorapidity distributions normalized by the average number of participating nucleon pairs for different collision centralities are plotted as a function of pseudorapidity shifted by the y_{beam} for Au+Au and Cu+Cu collisions at $\sqrt{s_{NN}}$= 62.4 and 200 GeV [58]. Right: Variations of $dN_{ch}/d\eta$ (top panel) and for $dN_\gamma/d\eta$ (bottom panel) normalized to N_{part} with $\eta - y_{beam}$ for different energies central collisions [59].

dinal scaling behaviour for various RHIC and LHC energies. The AMPT model uses HIJING (Heavy-Ion Jet INteraction Generator) for generating the initial conditions, Zhang's Parton Cascade (ZPC) model for partonic scatterings, the Lund string fragmentation or a quark coalescence model for hadronization. The hadronic matter interaction is described by a hadronic cascade based on a relativistic transport (ART) model. A analysis is performed to compare the pseudorapidity density of charged particles $dN_{ch}/d\eta$ of perfectly tuned AMPT results with the experimental data and to examine the longitudinal scaling.

1.8 Organisation of the thesis

The thesis is organised as follows: after the theoretical motivation on resonance study, CSPM model and particle production in present Chapter, in Chapter 2 the experimental facilities at the LHC are explained. The ALICE experiment and its different detectors are discussed in details. In Chapter 3 the details of data analysis methodology for the measurement of $K^{*\pm}$

is discussed. Chapter 4 covers the transport properties in heavy-ion collisions at RHIC energies using color string percolation model (CSPM). The transport properties are obtained and compared with the other theoretical calculations. The centrality dependent behaviour of percolation parameters, thermodynamic and transport properties in the framework of CSPM is also studied. In Chapter 5, the phenomenon of limiting fragmentation for nucleus-nucleus (A+A) collisions in the pseudorapidity distribution of charged particles and differential cross-section of charged particles at various energies is studied. At last, in Chapter 6 the results are summarised with important findings.

Chapter 2

Experimental Setup

"Attempt the impossible in order to improve work".

— Bette Davis

It is an instinct of the human being striving to understand more about the world we live in, simply for the sake of pure knowledge. The scientific knowledge has later transformed the way of living through technological applications. In the quest of knowledge, human beings could build scientific and complex technological wonders in the modern world. The Large Hadron Collider (LHC) [61] is the world's largest particle accelerator. It is based at CERN, Geneva, the acronym represents in French as "Conseil Europèen pour la Recherche Nuclèaire or European Council for Nuclear Research. In order to understand the origin and evolution of the universe, while addressing many fundamental questions like, origin of mass, understanding the quark confinement etc; the LHC plays a vital role in the frontiers of high-energy nuclear physics.

In this chapter, an introduction to the LHC and its different experiments are given in detail. A brief description of the ALICE (A Large Ion Collider Experiment) detector system and in particular the detectors used for particle identification for the data analysis in this thesis are given in the following sections. The last part of the chapter is dedicated to the online computing, data processing and reconstruction system based on the AliROOT framework.

2.1 The Large Hadron Collider (LHC)

The LHC machines are as gigantic as the Eiffel tower of Paris. However it is built within the tolerances smaller than a human hair. It is a particle accelerator composed of two rings installed in an underground tunnel having a circumference of 26.7 km lies between 47-170 m below the Earth surface with a slight inclination across the Switzerland and France border. It was installed in the existing CERN LEP (Large Electron-Proton collider) tunnel, which was built between 1984 – 1989 [61]. The CERN accelerator complex that acts as injector for the LHC is linked to LHC by two transfer tunnels of length 2.5 kms somewhere around ALICE and LHCb detector at TI2 and TI8, respectively.

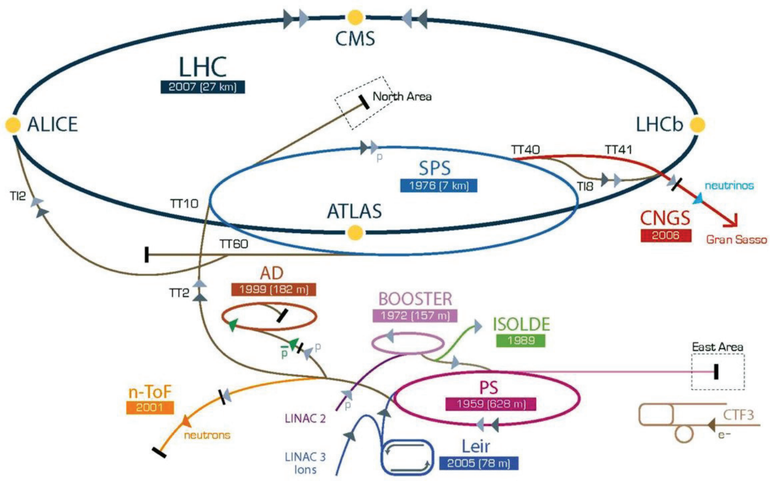

Figure 2.1: CERN accelerator complex showing the PS (Proton Synchrotron), SPS (Super Proton Synchrotron) rings and the four main LHC experiments (ALICE, ATLAS, CMS and LHCb) around the LHC ring [63].

The LHC is designed to allow pp collisions upto $\sqrt{s}$ = 14 TeV and Pb+Pb collisions upto $\sqrt{s_{\rm NN}}$ = 5.5 TeV. The design luminosity for pp collisions is $\mathcal{L} = 10^{34}$ cm^{-2}s^{-1} and for heavy ion collision is $\mathcal{L} = 10^{27}$ cm^{-2}s^{-1}. In Table 2.1 the details of Run I and Run II collision system, collision energy, luminosity and the year of data taking are tabulated [62]. The LHC is preparing for a major upgrade of its apparatus, during the long shutdown (LS2) in the 2018-2019 before Run III data taking. The main physics goals of Run III is to increase the luminosity, an increase of statistics by about two orders of magnitude for better measurement of heavy-flavour hadrons, quarkonia (heavy quark-anti-quark bound state), and low-mass dileptons at low transverse momenta, together with novel measurements of jets and their constituents and a significant improvement in vertexing and tracking efficiency at low transverse momentum etc. Figure 2.1 shows a schematic view of LHC accelerator complex.

Table 2.1: Table of collision systems, collision energies, year of data taking and luminosity during RUN I and RUN II till now.

System	Years	$\sqrt{s_{NN}}$(TeV)	L_{int}
Pb-Pb	2010-2011	2.76	$\sim$75 μb^{-1}
	2015	5.02	$\sim$205 μb^{-1}
Xe-Xe	2017	5.44	$\sim$0.3 μb^{-1}
p-Pb	2013	5.02	$\sim$15 μb^{-1}
	2016	5.02, 8.16	$\sim 3\ nb^{-1}$,$\sim 25\ nb^{-1}$
p-p	2009-2013	0.9,2.76	$\sim$200 μb^{-1}, $\sim$100 nb^{-1}
		7, 8	$\sim$1.5 pb^{-1}, $\sim$2.5 pb^{-1}
	2015, 2017	5.02	$\sim$1.3 pb^{-1}
	2015-2017	13	$\sim$25 pb^{-1}

The particles pre-accelerate through several processes before entering the LHC to achieve ultra-relativistic energies. In the pp collisions isolated protons are produced by stripping the electrons from hydrogen atoms. Then the protons beam is accelerated in Linear Accelerator 2 (LINAC 2) upto 50 MeV. The beam is further accelerated upto 1.4 GeV in Proton Synchrotron Booster (PSB) before injecting it to the Proton Synchrotron (PS) ring, where the protons reach an energy upto 26 GeV. After PS, the beam is then injected to Super Proton Synchrotron (SPS), which accelerates the protons to 450 GeV. The high energy proton beam is then injected to the beam pipes of LHC to reach the final energy. Different stages of accelerators are shown in Fig. 2.1. Likewise in Pb–Pb collision all the 82 electrons are stripped off from the lead atoms to create isolated lead ions, they undergo a complex step by step procedure: heated by microwaves several times, stripped by nanometer foils etc. Then the ion beam is injected to Linear Accelerator 3 (LINAC 3) and then they are injected to Low Energy Ion Ring (LIER). In LIER the lead ions are transformed from long pulses to short and dense bunches which are suitable for injection to the LHC.

The LHC facility consists of both high energy nuclear and particle physics experiments with four main detectors named as ATLAS, CMS, LHCb and ALICE. ATLAS (A Toroidal LHC Apparatus) [64] and CMS (Compact Muon Solenoid) [65] are general purpose detectors. The main purpose of these detectors are to search for Super Symmetric particles (SUSY), dark matter, evidence of extra dimensions and characterisation of the recently discovered Higgs boson [66, 67], resonances etc. The LHCb (LHC beauty) [68] is a special purpose forward detector placed very close to the beam direction and is used for the study of CP violation in the b-quark sector and matter anti-matter asymmetry in the universe. ALICE (A Large Ion Collider Experiment) is the only detector which is specifically designed to study evolution dynamics and characterisation of Quark Gluon Plasma (QGP) [69, 70]. Recently the general purpose detectors have also shown interest in the study of heavy ion collisions. The ALICE experiment and its different sub-detectors are discussed in details in the following sections.

2.2 A Large Ion Collider Experiment (ALICE)

The ALICE [70] is the experiment designed to study the physics of strongly interacting matter at extreme energy densities and high temperature, evolution dynamics of the nuclear matter in order to probe the de-confinement phase transition and chiral symmetry restoration. The dimension of ALICE detector is $16 \times 16 \times 26\ m^3$ and approximate weight is 10,000 ton. ALICE has right-handed Cartesian coordinate system with origin (x, y, z) = (0, 0, 0) at interaction point which is nominally at the centre of the detector. The x-axis points towards the LHC centre and y-axis points vertically upward. The polar angle, θ between z and y-axis increases from +z to -z direction and the azimuthal angle, ϕ is between the x and y-axis. The schematic layout of the ALICE detector is shown in Fig 2.2.

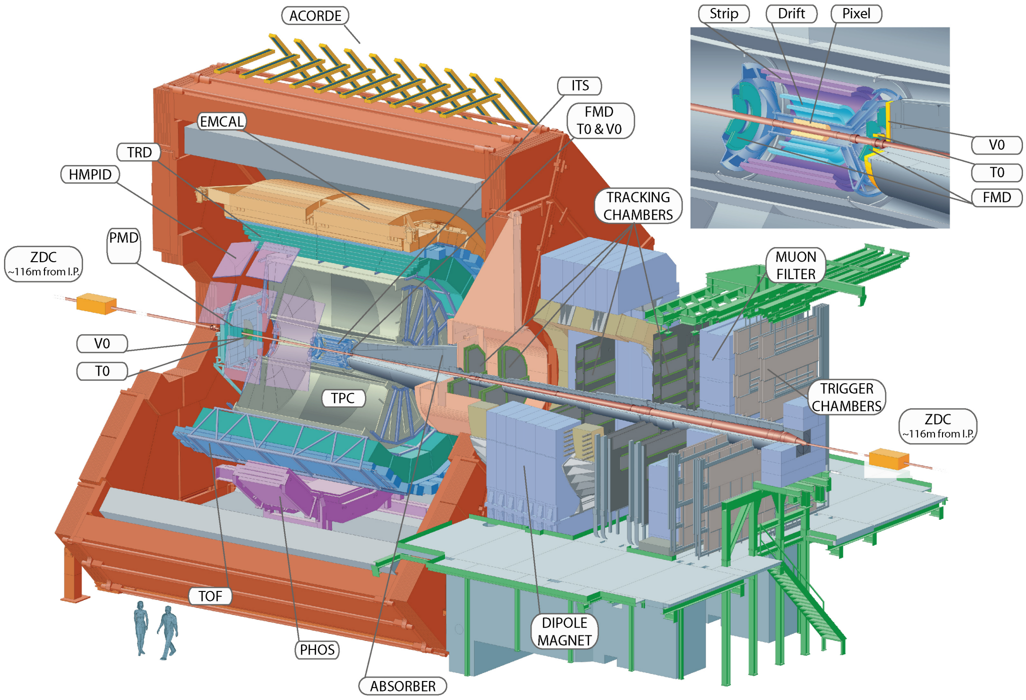

Figure 2.2: Schematic layout of ALICE detector setup [70].

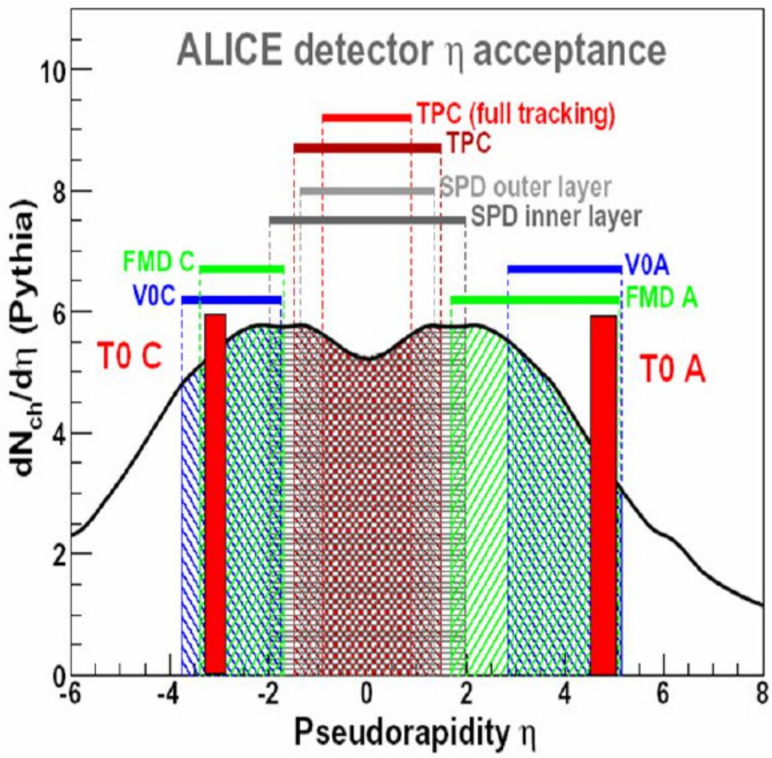

Figure 2.3: Pseudorapidity coverages of different sub-detectors of ALICE [71].

Table 2.2: The Alice detectors. Central and Forward detectors with there radial and longitudinal coordinates r, z measured with respect to the ALICE interaction point (IP2). The detectors marked with an asterisk (*) are used for triggering [69].

Detector	Acceptance		Position	Technology	Main purpose
	Polar	Azimuthal			
			Barrel Detectors		
SPD*	$\|\eta\| < 2.0$	full	r = 3.9 cm	Si pixel	tracking, vertex
	$\|\eta\| < 1.4$	full	r = 7.6 cm	Si pixel	tracking, vertex
SDD	$\|\eta\| < 0.9$	full	r = 15.0 cm	Si drift	tracking, PID
	$\|\eta\| < 0.9$	full	r = 23.9 cm	Si drift	tracking, PID
SSD	$\|\eta\| < 1.0$	full	r = 38 cm	Si strip	tracking, PID
	$\|\eta\| < 1.0$	full	r = 43 cm	Si strip	tracking, PID
TPC	$\|\eta\| < 0.9$	full	$85 < r/cm < 247$	Ne drift+MWPC	tracking, PID
TRD*	$\|\eta\| < 0.8$	full	$290 < r/cm < 368$	TR+Xe drift+MWPC	tracking, $e^{\pm}$ id
TOF*	$\|\eta\| < 0.9$	full	$370 < r/cm < 399$	MRPC	PID
PHOS*	$\|\eta\| < 0.12$	$220^0 < \phi < 320^0$	$460 < r/\mathrm{cm} < 478$	$PbWO_4$	photons
EMCal*	$\|\eta\| < 0.7$	$80^0 < \phi < 187^0$	$430 < r/\mathrm{cm} < 455$	Pb+scint.	photons and jets
HMPID	$\|\eta\| < 0.6$	$1^0 < \phi < 59^0$	$r = 490$ cm	C_6F_{14} RICH+MWPC	PID
ACORDE*	$\|\eta\| < 1.3$	$30^0 < \phi < 150^0$	$r = 850$ cm	scint.	cosmics
			Forward Detectors		
PMD	$2.3 < \eta < 3.9$	full	$z = 367$ cm	Pb+PC	photons
FMD	$3.6 < \eta < 5.0$	full	$z = 320$ cm	Si strip	charged particles
	$1.7 < \eta < 3.7$	full	$z = 80$ cm	Si strip	charged particles
	$-3.4 < \eta < -1.7$	full	$z = -70$ cm	Si strip	charged particles
V0*	$2.8 < \eta < 5.1$	full	$z = 329$ cm	scint.	charged particles
	$-3.7 < \eta < -1.7$	full	$z = -88$ cm	scint.	charged particles
T0*	$4.6 < \eta < 4.9$	full	$z = 370$ cm	quartz	time, vertex
	$-3.3 < \eta < -3.0$	full	$z = -70$ cm	quartz	time, vertex
ZDC*	$\|\eta\| > 8.8$	full	$z = \pm 113$ m	W+quartz	forward neutrons
	$6.5 < \|\eta\| < 7.5$	$\|\phi\| < 10^0$	$z = \pm 113$ m	brass+quartz	forward protons
	$4.8 < \eta < 5.7$	$\|2\phi\| < 32^0$	$z = 7.3$ m	Pb+quartz	photons
MCH	$-4.0 < \eta < -2.5$	full	$-14.2 < z/m < -5.4$	MWPC	muon tracking
MTR*	$-4.0 < \eta < -2.5$	full	$-17.1 < z/m < -16.1$	RPC	muon trigger

The ALICE detector system consists of mainly two parts and a set of small detectors for triggering and event characterisation. The central barrel part, which covers the pseudo-rapidity density $|\eta| < 0.9$ and full azimuth mainly perform vertexing, tracking, PID (Particle IDentification), calorimetry etc. while the forward detectors, which consist of forward muon spectrometer ($|\eta| \sim 2.5 - 4$), are dedicated to study quarkonia. The Photon Multiplicity Detector (PMD) is used for the measurement of photon multiplicity, fluctuations and azimuthal anisotropy. In Table 2.2 all the 17 central and forward detectors are listed along with the polar and azimuthal coverage, radial/transverse and longitudinal position coordinates, the basic technology used for the detector. The ALICE detector has a large η coverage, which is shown in the Fig. 2.3 with each detector acceptance. For this thesis work, ITS (Inner Tracking System) and TPC (Time Projection Chamber), which are the main charged-particle central detectors are used. The detailed description of these two detectors are discussed in the following sub-sections. Apart from these detectors there are several central barrel detectors, which are fixed inside the L3 magnet with 0.5 T magnetic field.

TRD (Transition Radiation Detector) [72] consists of six layers of Xe-CO_2 filled Multi-Wire Proportional Chambers (MWPC) in the radial position, $2.90 < r < 3.68$ m from the interaction point, with a fiber radiator in front of each chamber. It has the pseudorapidity acceptance region, -0.84 $< \eta <$ 0.84 and full azimuthal coverage. The charged particle and electron identification is done via transition radiation and dE/dx. It is almost 100% efficient in separating electrons from pions. It is also used for triggering and tracking of electrons and jets.

On top of TRD, Time of Flight (TOF) [73] detector is placed, which is another full azimuth barrel detector having the inner radius of 3.7 m in the pseudo-rapidity range of $|\eta| <$0.9. Its working principle is based on the Multigap Resistive Plate Chamber (MRPC) technology, for the charged particle identification in the intermediate momenta. The charged particle ionizes the gas creating an avalanche of electrons, which moves towards the electrode. The avalanche is stopped by the resistive plates in each gap. The induced charge gives very fast signal with overall time resolution of about 86 ps. The estimation of mass (m) is done by measuring the time (t) taken by the particle to travel from interaction vertex to the TOF detector, like, m = $p/\gamma\beta c$, where p is the momentum of the particle, β is the ratio of velocity to the speed of light c. $\gamma = 1/\sqrt{1-\beta^2}$ is the Lorentz factor.

The PHOS (Photon Spectrometer) [74] is an electromagnetic calorimeter of high granularity, which is used as a triggering detector. It is situated at a radial distance of 4.6 m, within pseudo-rapidity of $|\eta| < 0.12$ and azimuthal acceptance of $260^0 < \phi < 320^0$. It has 5 modules of 17280 detection channels made up of lead-tungstate($PbWO_4$) crystals. PHOS is dedicated for the study of the properties of the initial phase of the collision like initial temperature by measuring direct and thermal photons, measuring high-p_T pions and eta mesons. The PHOS is optimised to measure photons, π^0's and η mesons in higher-p_T range.

The EMCal (Electromagnetic Calorimeter) [75] is positioned at a radial distance of 4.5 m, approximately opposite to PHOS within pseudorapidity of $|\eta| < 0.7$ and azimuthal acceptance of $80^0 < \phi < 187^0$. It is a lead-scintillator having supermodules packed with cell structure called 'towers' of size 6×6 cm. When the electrons and photons enter the EMCal, they produce an electromagnetic shower and deposit their energy in the EMCal towers, which is reconstructed using cluster finding algorithms. Apart from acting as a triggering detector, the important physics goal of the EMCAL detector is to study jet quenching over the large kinematic range and to measure high momentum photons and electrons.

The HMPID (High Momentum Particle Identification Detector) [69, 76] consists of 7 identical ring-imaging Cherenkov (RICH) modules filled with a liquid C_6F_{14} radiator coupled to MWPC based photon detectors with CsI photocathode. The HMPID detector extends charged hadron identification in ALICE to higher momenta. The particle identification is based on the principle of the Cherenkov angle measurement produced by charged tracks, which emit conical electromagnetic radiation. Using HMPID, the identified hadrons can be measured above transverse momenta of 1 GeV/c, for example: the charged pions and kaons can be identified up to 3 GeV/c and 5 GeV/c, respectively. The ALICE Cosmic Ray Detector (ACORDE) [77] is placed on top of the L3 magnet at a radial distance of 8.5 m, within $|\eta| < 1.3$ and $30^0 < \phi < 150^0$. It is a plastic scintillation detector. ACORDE is used for cosmic-ray studies, alignment and calibration of different ALICE detectors.

The ALICE forward detectors are dedicated for the measurement of photons and charged particles in the forward rapidity region. These are used for triggering and for the determination of centrality and event plane angle in Pb + Pb collisions. A brief discussion on the forward detecters are given in the following paragraphs.

The PMD (Photon Multiplicity Detector) [78, 79] is a pre-shower detector in the forward rapidity region (2.9 < η <3.9) to measure photon multiplicity on even-by-event basis. It can also be used for estimation of reaction plane. The PMD is placed at about 3.6 m from IP along the +ve z-axis. It has a lead converter of $3X_0$ (radiation length) thickness, which is sandwiched between two planes of gaseous proportional counters of high granularity. It has honeycomb structured gas proportional counters with wire readout in it.

The FMD (Forward Multiplicity Detector) [80] consists of five detector rings in the region -3.4 < η < -1.7 and 1.7 < η < 5.0, having 20 and 40 sectors each with full azimuthal coverage. The main purpose of the FMD system is to provide (offline) precise charged particle multiplicity as well as the reaction plane for each event. A common phase space of PMD and FMD allows us to study charge-neutral correlations and fluctuations.

The ALICE VZERO (V0) [80, 81] is a small-angle plastic scintillator hodoscope detector installed on both sides of the ALICE collision vertex. The detector covers a pseudo-rapidity range of 2.8 < η < 5.1 (V0A) and -3.7 < η < -1.7 (V0C). V0A and V0C are placed opposite to each other at a distance of 328 cm and 88 cm from interaction point (IP), respectively. This detector provides minimum-bias triggers for the central barrel detectors in pp and A+A collisions. V0 serves as an indicator of the centrality of the collision via the particle multiplicity recorded in an event.

The T0 [80] detector consists of two arrays of Cherenkov counters T0C and T0A located on the both sides of the interaction point (IP) at a distance of 70 cm and 360 cm from IP. The coverage of T0C and T0A are at $-3.8 < \eta < -2.97$ and $4.61 < \eta < 4.92$, respectively. The detector can measure the collision time precisely up to 25 ps. This time is used as a start time for the TOF measurement and to measure the vertex position. The T0 detector is also used to generate minimum bias and multiplicity triggers.

The Zero Degree Calorimeter (ZDC) [82] is used to detect spectator nucleons that leave the IP along the beam direction. The ZDC are placed on both sides of the IP at a distance of 116 m from IP. It consists of four caloriemeters, two to detect neutrons (ZN) and two to detect protons (ZP). Due to the dipole magnets the spectator protons defect the spectator neutrons which basically fly away zero degree with beam axis. The ZDCs are arranged with heavy metal plates and matrix of quartz fibres. The tungsten and brass metal plates are used for neutrons and protons, respectively. The main function of ZDC is to determine the centrality and reaction plane (necessary for elliptic flow analysis) of an event in heavy-ion collisions and it is also used as level-1 (L1) trigger.

The muon spectrometer [83] has the coverage $-4.0 < \eta < -2.5$ in pseudo-rapidity region and $\phi = 2\pi$ in azimuth. The prime purpose of it is to measure heavy-quark vector-mesons, J/ψ, ψ', υ, υ' etc., as these particles decay into muons ($\mu^+\mu^-$). A front absorber made up of carbon, concrete and steel is used to shield hadrons and photons from the interaction vertex, and filters the background particles giving a cleaner sample of muons.

2.3 Central barrel detectors

2.3.1 Inner Tracking System (ITS)

The Inner Tracking System [84] in ALICE consists of six cylindrical layers of silicon detectors encircling the interaction point to cover full azimuth around the beam pipe. ITS lies within the radii 3.9 cm − 43 cm from the interaction point. Fig. 2.4 shows the geometrical layout of the ITS. The prime purpose of ITS is to determine the primary and secondary vertices necessary for the reconstruction of charm and hyperon decays. ITS also helps in particle identification and tracking of low-momentum particles and to improve the momentum measurements of the TPC.

For Pb-Pb collisions at $\sqrt{s_{NN}} = 5.5$ TeV the multiplicity density can go up to 100 particles per cm^2. To accurately measure the track distance

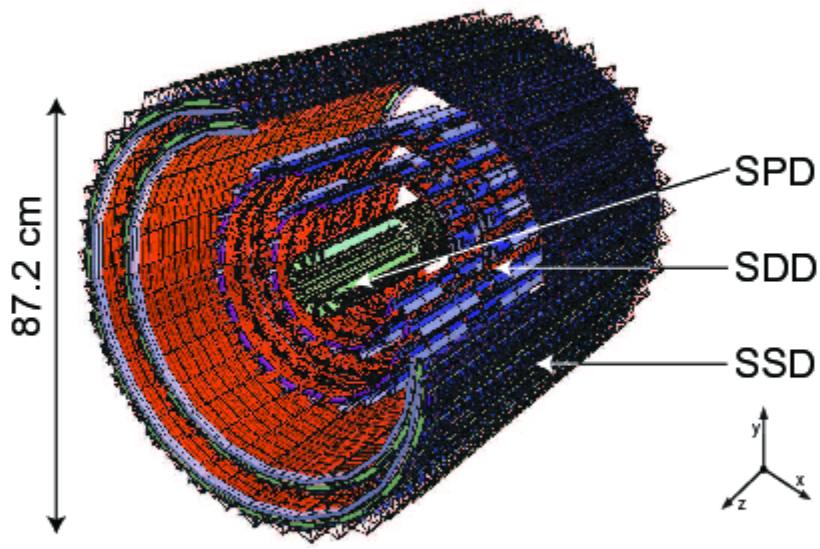

Figure 2.4: Layout of ALICE Inner Tracking System [84].

of closest approach, the first two layers Silicon Pixel Detectors (SPD) are used. The SPD is a two-dimensional matrix or else called detecter ladder of reverse-biased silicon based p-n junction diode. Each SPD cell, which is typically a rectangle of a few tens of μm to few hundreds of μm in dimension is connected to the readout electronics. To optimise the SPD detector to work closer to the IP, where the particle density is the highest, it is made with highly granular silicon pixels of dimensions. The readout information are binary in nature. A threshold is applied to the pre-amplified signal and each cell gives a logical output if the signal exceeds the threshold. These layers determine the quality of the position of the primary vertex, measurement of the impact parameter of secondary tracks from the weak decays of strange, charm and beauty particles. In such a high particle density the determination of the vertex position is challenging. To find the z-coordinate of the interaction point with a high precision ($\sim 10\ \mu m$) the hits in the two pixel layers are correlated without tracking. This precision downgrade the efficiency at lower multiplicity. The track finding in this environment is even more challenging, which is based on Kalman filter algorithm, widely used for high-energy physics detectors. From the outermost pad rows of the TPC seed-finding starts, then it proceeds with the Kalman filter through all the TPC preparing for the track reconstruction.

Explicitly using the vertex constraint, one try to match the tracks from TPC with the hits from SSDs to the vertex. The neural network algorithm is used for finding low momentum tracks, p_T 100 MeV/c. It is also used as level-2 (L2) trigger. SPD is placed in the pseudo-rapidity range of $|\eta| < 2$ with full azimuthal coverage and it operates in a relatively high-radiation environment.

The two middle layers are made up of Silicon Drift Detectors (SDD). They couple a very good multi-track capability with dE/dx information. The SDD ladders are mounted on linear structures. The layers are at the average radius of 14.9 and 23.8 cm and are composed of 14 and 22 ladders, respectively. SDD measure the transport time of the charge deposited by a traversing particle to localize the impact point in one of the dimensions, thus enhancing resolution and multi-track capability at the expense of speed. This is very suitable for high particle multiplicities coupled with relatively low event rates. A linear SDD, has a series of parallel p+ field strips, connected to a voltage divider on both surfaces of the high-resistivity n-type silicon wafer. The field strips provide the bias voltage to the volume of the detector and they generate an electrostatic field parallel to the wafer surface, resulting in the creation of a drift region. When a charged particles cross the detector, electron-hole pairs are created. The holes move to the p+ electrode and the electrons are driven by the drift field towards the edge of the detector, where they are collected by an array of anodes composed of n+ pads. The small capacitance of the anodes produce low noise and good energy resolution.

The two outer layers are equipped with double-sided Silicon micro-Strip Detectors (SSD) where the track density has fallen to one particle per cm^2. The inner radius of SSD is 39 cm. And it consists of 300 mm thick, 40 mm long, double sided silicon strip sensor with p and n in opposite side with a separation of 95 mm. These are supported by lightweight carbon fibre structures. The patterns are identical on the p- and the n-sides of the detector. In order to limit the number of ambiguities for the high particle densities, the stereo angle is set small. The detectors are mounted with the strips parallel to the magnetic field to get the best position resolution obtained in the bending direction. The four outer layers are crucial to connect the tracks from TPC to the ITS. SSD uses dE/dx measurement in the very low transverse momentum region (non-relistivistic) for particle identification. It gives good tracking and PID performance at low-p_T by measuring the transport time of the electrons and holes which are created in the process of ionisation, while the particle passes through the 300 mm thick p-n junction.

2.3.2 Time Projection Chamber (TPC)

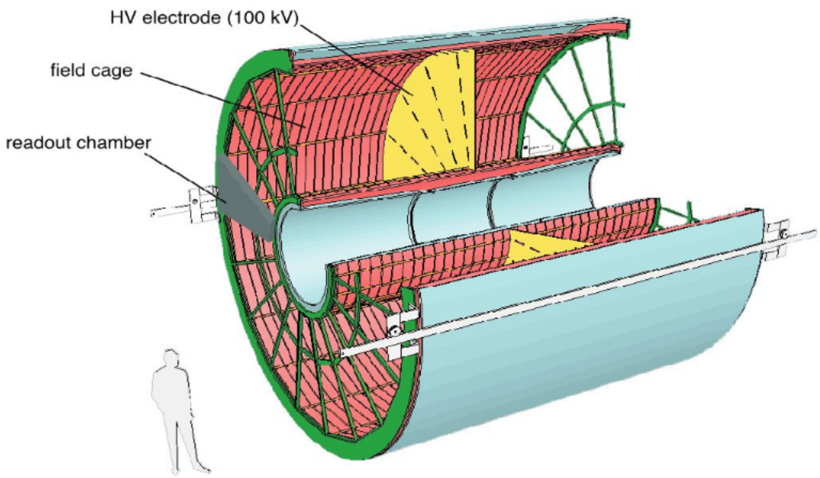

Figure 2.5: The ALICE Time Projection Chamber (TPC) [85].

In the central barrel detectors TPC is the main tracking detector with an acceptance covering pseudo-rapidity region of $|\eta| < 0.9$ and has full azimuthal coverage [86]. It is a large cylindrical gaseous detector placed around the ITS. The main purpose of TPC is tracking, particle identification and helps in vertex determination. It occupies an active volume of 88 m^3 covering length of 500 cm along the beam axis with inner and outer radius about 85 cm and 250 cm, respectively. Figure 2.5 shows the schematic view of ALICE TPC. The detector is filled with a gas mixture of $\mathrm{Ne} - \mathrm{CO_2}$ (90 : 10). A cylindrical conducting electrode is placed at the centre to maintain a uniform axial electrostatic field (drift field) of 400

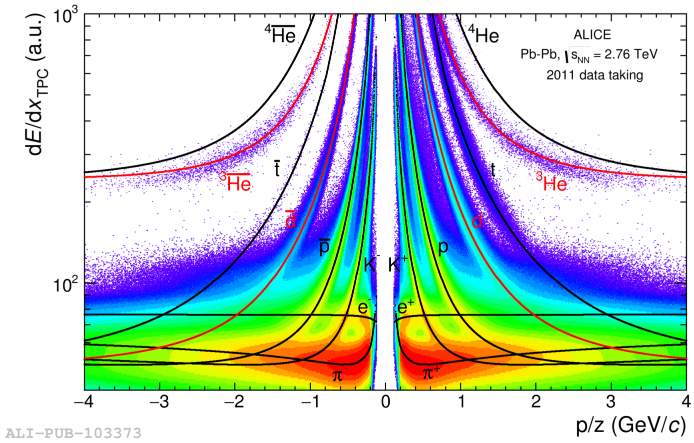

Figure 2.6: Specific energy loss (dE/dx) of the tracks as a function of rigidity (p/z) for different particles and anti-particles in Pb-Pb collisions at $\sqrt{s}_{NN}$= 2.76 TeV. The solid line represents the theoretical Bethe-Bloch dE/dx expectations.

V/cm along the beam direction. It has a homogeneous electric field and a high magnetic field used to bend the trajectory of the particle. A charged particle, while passes through the detector, ionizes the gas, then the free electrons drift towards the endplates of the cylinder under the influence of the electric field and the ions drifts towards the high voltage cathode placed at the centre of the TPC. The readout planes are installed at the two endplates consist of 72 MWPC (Multi-wired Proportional Chamber)-based readout chambers, with a total of about 550,000 readout cathode pads. The cylindrical position co-ordinates r and ϕ of the hit is measured by the position of signal cluster and z position of hit is measured by the arrival time of the signal cluster. The tracks are reconstructed and their momentum is calculated by the curvature of the path in presence of the magnetic field.

The TPC can reconstruct a primary track having momentum from 100 MeV/c to 100 GeV/c. Another main goal of TPC is the identification of each particle traversing through its active volume. This is done by measuring the specific energy loss (dE/dx), charge and momentum simultaneously. Using the Bethe-Bloch formula (Eq. 2.1), the energy loss of charged particles in the detector medium can be estimated as,

$$-\langle\frac{\mathrm{dE}}{\mathrm{dx}}\rangle = \frac{4\pi \mathrm{Ne}^4}{\mathrm{mc}^2\beta^2}\mathrm{z}^2\left(\ln\frac{2\mathrm{mc}^2\beta^2\gamma^2}{\mathrm{I}} - \beta^2 - \frac{\delta(\beta)}{2}\right) \tag{2.1}$$

Here m , e and N are the mass, charge and number density of electron, z and β is the charge and velocity of the traveling particle, $\gamma^2 = 1/(1-\beta^2)$ the Lorentz factor, and I is the mean excitation energy of the atom. The correction term for density effect [87] is $\delta(\beta)$. In the low-velocity region, the energy loss decreases due to the term $1/\beta^2$. At relativistic limit ($\beta \sim 0.97$) the ionization value becomes minimum and in this region, the particles are called minimum ionization particles. The energy loss, described by the Bethe-Bloch formula is parametrised for each particle species. The energy loss distribution for various mass particles are shown in Fig 2.6.

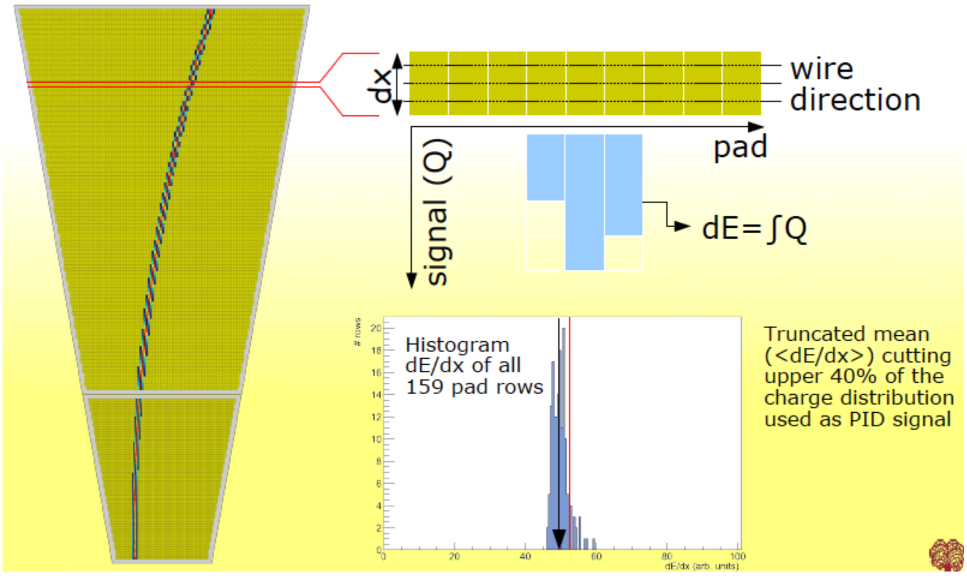

Figure 2.7: Schematic diagram of $\langle$dE/dx$\rangle$ measurements in TPC [88].

The Time Projection Chamber measures the charge deposited on 159 padrows. The ionization measured on the TPC pads involves six steps: energy loss, energy deposition, ionization, electron transport, amplification, and AD conversion, which considered from energy loss of particles to the ADC output measured in the TPC. TPC performs multiple measurements of energy loss in low density absorbers, then average of energy loss in different layers is computed. These measurements have large variations which is a Landau distribution. To get a high degree of precision the high energy tail of the Landau type energy-loss distribution is ignored or suppressed, by applying truncated mean method discarding the upper 40% charge cluster distribution [69, 89]. Figure. 2.7 shows a schematic diagram of the dE/dx measurement and the truncated mean method. The red line in the dE/dx vs. # of rows plot is the cut line to truncate the dE/dx distribution discarding the energy-loss part which is $\sim 40\%$ of the distribution from the higher-end tail side. The largest separation is achieved at low p_T ($p_T < 0.7$ GeV/c) but a good separation is also present in the relativistic region ($p_T > 2$ GeV/c).

2.4 ALICE Online system

The ALICE detector online control system constitutes Trigger system (TRG), Data AcQuisition (DAQ), High Level Trigger (HLT), Detector Control System (DCS) and Experiment Control System (ECS) [90, 91].

2.4.1 Trigger System (TRG)

The ALICE central trigger processor is designed to carefully choose a bunch of physics selected events from a big pile of data. It has three different levels of trigger such as level-0 (L0), level-1 (L1) and level-2 (L2) categorised depending upon different arrival times of the trigger inputs and the precise timing requirements of the detectors. The Low level trigger (L0), which is too fast to receive all the trigger inputs combines the information from the V0 (centrality), TOF, T0 (event vertex), SPD, EMCal, PHOS (photon), MTR (muons) and ACORDE (cosmic rays). The combined signal then is delivered 1.2 μs after the crossing of each bunch. Next Level 1 (L1) signal arriving at 6.5 μs picks up all remaining fast inputs from ZDC (MB interaction), EMCal (photons, neutral jets) and TRD (electrons, high-p_{T} particles, charged jets). A final level of the trigger (Level 2, L2) waits for the end to take decision after 100 ms which comes after the end of the TPC drift time. This interval can also be used for running trigger algorithms.

After the final trigger, the trigger system decides whether the event to be asserted, negated or not relevant. Then the data are recorded via Data AcQuisition (DAQ) system.

2.4.2 High Level Trigger (HLT)

The ALICE High Level Trigger (HLT) [92] collects information from all major detectors, resulting after a trigger selection and processes it to decide whether the event needs to be accepted or rejected. The on-line processing reduces the size of the event or sub-events without losing physics information by compressing the accepted and selected data.

2.4.3 Detector and Experiment Control System

To allow a safe and easy operation of the ALICE experiment the ALICE Detector Control System (DCS) is always operational throughout the operational phases including the shutdown periods also. DCS provides remote access to the experts to cope with different operational modes, and allows independent and concurrent operation of each sub-detector or any part of ALICE. The ALICE Experiment Control System (ECS) is a central control system which coordinates the operations by the online systems and where all operations are initiated.

2.5 Aliroot framework

Understanding Big Data in High Energy Physics is just like finding a needle in a haystack. So to analyse it, a set of the software tools are needed for data processing which is called a framework. The Aliroot [93] is one such tool which is based on the Object Oriented framework which is used for simulation, alignment, calibration, reconstruction, visualisation and analysis of the experimental data. It uses ROOT, which is a scientific software framework mainly written in C++ and integrated with other languages like

Python and R. In addition to the package for physics analysis, the software for the simulation of events and detector is also required to provide an environment for the development of software packages helpful for event generation. The example of typical event generators are PYTHIA [94, 95], PHOJET [96], HIJING [97] etc. and some hybrid event generators like: EPOS, DIPSY etc.

The particles generated from the event generator packages are then propagated through the detector's material. The Monte Carlo transport packages GEANT3 [98], GEANT4 [99], FLUKA [100] etc. are used to simulate the particle transport through the virtually developed ALICE detector. All the physics interactions like in a real experiment are simulated during the propagation of the particles. Each detector stores the hit position and time information, energy deposition at a given point. The hit information is converted into digits by considering the detector and associated electronic response. At the end of the process, each digits of the corresponding detectors are stored as the raw data. Then for the track reconstruction of the raw or simulated data, the very first thing to do is to obtain clusters information from the digits. The cluster information, tracking is performed by combining the most probable path for the particle in the detector. The track reconstruction is done by Kalman filter algorithm [101]. After TPC and ITS tracking which are main responsible detector for tracking, the space points are also extended in different other detectors like TRD, TOF, HMPID, EMCAL, PHOS, etc. Finally considering all these detectors simultaneously, track parameters for track reconstruction are extracted with and without primary vertex. After the reconstruction, the first version of the data is stored as an Event Summary Data (ESD), where complete information for each event is kept. A compressed version of ESD data with only relevant information for the analysis is stored as Analysis Object Data (AOD). These ESD and AOD data are used for the real physics analysis purposes.

The framework has paramount features due to its modularity, reusability and reliability. The modularity features allow replacement and/or changes of well defined parts of the system with minimal or even no impact on the rest of the analysis framework. The re-usability protects the framework and regain it at any time whenever the analyser wants. All the features are cross checked and are universal in nature, so it is more reliable as compared to a personal framework.

Chapter 3

Measurement of $K(892)^{*\pm}$ mesons production in minimum-bias pp collisions

Postulates of T.D. Lee:

"Without experimentalists, theorists tend to drift".

"Without theorists, experimentalists tend to falter".

Measurement of strange hadrons like the vector meson K^* permits us to study strangeness production and to test hadronization of strange particles using event generators. Due to the short lifetime of K^* (both neutral K^{*0} and charged $K^{*\pm}$) they are sensitive to probe the dynamical evolution of the fireball created in heavy-ion collisions. In fact, even if they are produced at the hadronization of the QGP, they decay in the hadronic medium during the expansion of the system. The effects of the hadronic final-state interactions like, rescattering and absorption could lead to a distortion of the resonance spectra [102, 103]. The reconstruction of invariant mass of charged K^* is quite challenging as neutral K is used for its identification along with pions. The analysis method for the measurement of $K^{*\pm}$ in minimum-bias pp collisions are discussed in this chapter. The flow chart for a quick overview of the sequential movement of the analysis is shown in Fig. 3.1.

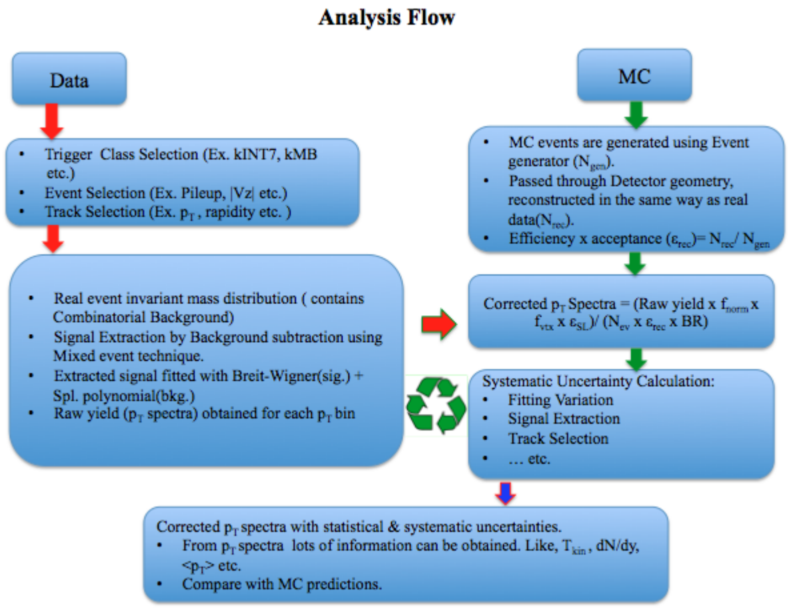

Figure 3.1: Analysis flow chart.

3.1 Introduction

In this thesis, measurement of $K(892)^{*\pm}$ mesons, produced in minimum-bias pp collisions at $\sqrt{s} = 5.02$ and 8 TeV using the ALICE detector is presented. $K^{*\pm}$ mesons along with other "Resonance particles" are discovered by experimental physicist *Prof. Luis Walter Alvarez* during 1960s [104]. For his achievements he was awarded with the most prestigious award, Nobel prize in 1968. In Fig. 3.2 the discovery of the invariant mass spectrum of $K^{*-} \rightarrow K^0_S + \pi^-$ from $K^- + p$ collision is shown [104]. The properties of the $K^{*\pm}$ and K^{*0} mesons are listed in Table 3.1 for the sake of a comparative analysis. The charged K^* has a mass and life time comparable with neutral K^*. The $K^{*\pm}$ mesons have strangeness content and are produced via strong interaction. After the production, it decays to a K^0_S and a charged pion. Then the K^0_S decays via weak interaction to two charged pions.

The study of resonance production in ultra-relativistic heavy-ion collisions provide information on the properties of the hadronic medium and different stages of its evolution. Due to the short life time, resonances allow to estimate the time span in the hadronic phase between the chem-

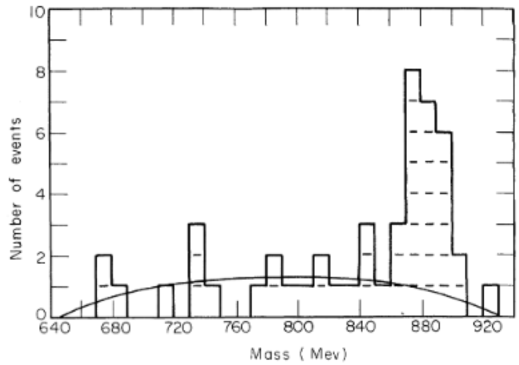

Figure 3.2: The invariant mass spectrum of $K^{*-} \rightarrow K_S^0 + \pi^-$ from $K^- + p$ collision. The solid line represents the phase-space curve normalized to background events [104].

Properties	$K^{*\pm}$	K^{*0}
Mass	$891.6 \pm 0.26\ MeV/c^2$	$895.81 \pm 0.19\ MeV/c^2$
Width	$50.8 \pm 0.9\ MeV/c^2$	$47.4 \pm 1.3\ MeV/c^2$
Quark Contents	$u\bar{s}, \bar{u}s$	$d\bar{s}, \bar{d}s$
Decay Mode	$K_S^0\pi^\pm$	$K^\pm\pi^\mp$
Life time	$\sim$ 4 fm/c	4.2 fm/c
Branching ratio	$\sim$ 0.33	$\sim$ 0.66

Table 3.1: Properties of neutral and charged K^*.

ical and the kinetic freezeout. The $K(892)^{*\pm}$ resonances are having lifetime ($\sim 4\ fm/c$), which is comparable to the lifetime of the fireball produced in the ultra-relativistic collisions. This helps us to understand the hadronic in-medium phenomenon like rescattering and regeneration effects. Quark-Gluon-Plasma (QGP) is believed to be formed in (central) heavy-ion collisions, where a very high temperature and energy density is created [105, 106]. The strangeness enhancement which is a signature of QGP can also be examined by the study of $K^{*\pm}$ production. The $K^{*\pm}$ is studied via their two step hadronic decay channel, $K^{*\pm} \rightarrow K_S^0 + \pi^\pm$ with branching ratio of 33.4% and K_S^0 decaying weakly via the decay topology $K_S^0 \rightarrow \pi^+ + \pi^-$ with a branching ratio $69.2 \pm 0.05\%$. Measurements of $K^{*\pm}$ in pp collisions serve as baseline to study Pb-Pb collisions for the corresponding energy and help in tuning of various Monte Carlo models. In addition, a multiplicity dependent $K^{*\pm}$ production in pp collision would help in understanding particle production and medium properties from pp to A–A collisions.

3.2 Analysis Details

3.2.1 Data sample and event selection

The production of $K^{*\pm}$ meson is measured at mid-rapidity ($|y| < 0.5$) in pp collisions at $\sqrt{s} = 5.02$ and 8 TeV using the ALICE detector [107, 108]. For pp minimum-bias collision energy $\sqrt{s} = 5.02$ TeV the data were collected during 2015 at the beginning of Run 2 operation at the LHC. For $\sqrt{s} =$ 8 TeV, data were collected in 2012 in different datasets during the Run 1 operation.

The data were collected with a minimum bias trigger requiring a hit in both VZERO detectors, in coincidence with the arrival of proton bunches from both directions. The VZERO detectors provide minimum-bias triggers to the central barrel detectors in pp and A-A collisions. The physics selection framework is widely used within ALICE to select events satisfying certain trigger criteria and reject beam-gas and pileup events. The physics selection is performed mainly in two steps: (1) selection of events with relevant trigger classes fired, (2) rejection of background, pileup events and poor quality events. Trigger is an electronic system which makes a decision whether the collision data are worth to save or not. The input to the trigger system is taken from triggering detectors, which send the signal to the trigger system when collision occurs. The output from the trigger system is sent to readout detectors which detect and save the collisions. The basic scheme for the signal propagation is: *triggering detector* $\longrightarrow$ *trigger* $\longrightarrow$ *readout detector*. In Fig. 3.3 the position of the VZERO detector is shown in the ALICE detector setup. The VZERO detector consists of two detectors V0A and V0C located 3.4 m away from the vertex on the opposite side of muon spectrometer and 0.9 m away from the vertex in front of the hadronic absorber, respectively. The kINT7 type minimum-bias trigger, which is used for these analyses is set depending on the two scintillation hodoscope, V0A and V0C timing decisions. This trigger reduces the contamination from single diffractive and electromagnetic events. After the selection of minimum-bias events, offline event selection criteria are used to reject the non-physics events. For Run 1 at $\sqrt{s}$ = 5.02 TeV and Run 2 at $\sqrt{s}$ = 8 TeV datasets, different offline event selection criteria are used. That means for 5.02 and 8 TeV different event selection criteria are used. After the application of the event selection criteria, around $\sim$ 110 M events are accepted for 5.02 TeV and $\sim$ 70 M events are accepted for 8 TeV for this analysis. The details of the event selection criteria for both the energies are noted below:

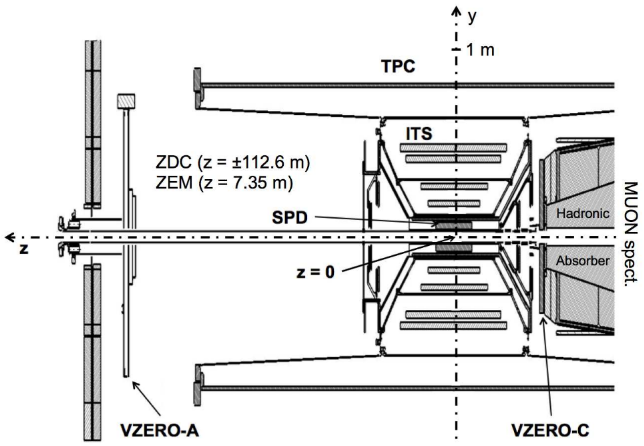

Figure 3.3: Position of the two VZERO arrays, within the general layout of the ALICE experiment [81].

Event selection criteria for Run 1 data: 8 TeV

1. Pileup rejection using AliAnalysisUtils::IsPileUpEvent().
2. Event has a track or SPD primary vertex is identified.
3. Vertex z position: $|v_z| < 10$ cm.

Event selection criteria for Run 2 data: 5.02 TeV

1. Pileup rejection using AliAnalysisUtils::IsPileUpEvent().
2. Event has a track or SPD primary vertex identified.

3. Vertex z position: $|v_z| < 10$ cm.

4. IsIncompleteDAQ check is used to reject events for which the event building does not work.

5. SPD Clusters vs. Tracklets Check using AliAnalysisUtils:: IsSPD-ClusterVsTrackletBG() with default parameters.

6. SPD vertex z resolution < 0.25 cm.

7. SPD vertex dispersion < 0.04.

8. z-position difference between track and SPD vertex < 0.5 cm.

3.2.2 Track and PID selection

The procedure for track finding in the central barrel detectors is shown schematically in Fig. 3.4. It starts with the clusterization step, in which the detector data are converted into "clusters" characterized by positions, signal amplitudes, signal times, etc. and their associated errors. The clusterization is performed separately for each detector. Then the preliminary interaction vertex is determined using clusters of SPD. Track finding and fitting is performed in TPC and ITS using the Kalman filter technique. The track information is stored for the analysis after the outward track propagation and inward propagation with final refits. The final interaction vertex, secondary vertex (V^0) and cascade decays findings are done thereafter. For specific analysis offline criteria are used for the track selection.

The $K^{*\pm}$ mesons are identified by reconstructing their decay products, a charged pion and K^0_S pair. Here K^0_S is a V^0 particle. The K^0_S is reconstructed from two weakly decayed pions. A schematic diagram of the two step decay process of K^{*+} is shown in Fig. 3.5. There are different criteria used to select strongly decayed primary pions and K^0_S. Selection criteria are also used for daughter tracks (pions) from weak decay of K^0_S. The details are described in the following subsections.

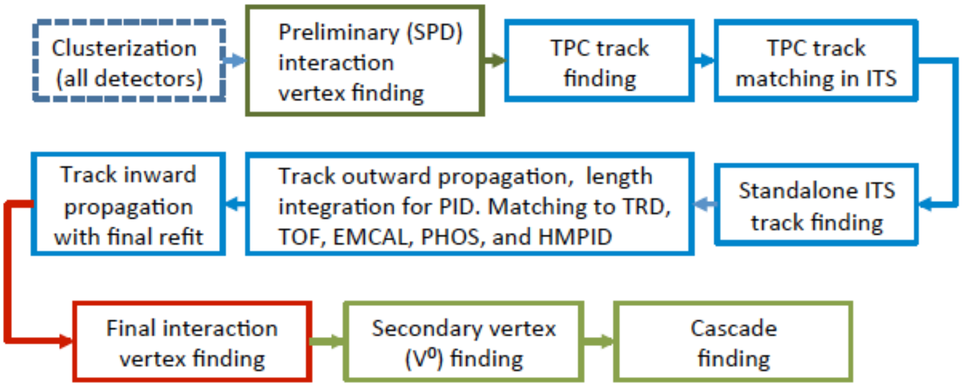

Figure 3.4: Event reconstruction flow [109].

3.2.3 Primary pion selection

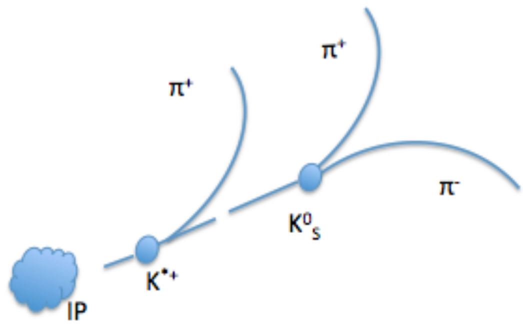

Figure 3.5: Schematic diagram of K^{*+} decay.

The maximum TPC coverage for tracking is $|\eta| < 0.9$ with full azimuthal acceptance. To avoid the edge effect of TPC, tracks are being imposed with the selection criteria $|\eta| < 0.8$. The track selection of primary particles require to have at least 70 pad rows measured along the track out of a maximum possible 159 pad rows in the TPC. A χ^2 per degrees of freedom from the Kalman fit procedure is set less than equal to 4. Each track should have at least one cluster hit in the SPD with a χ^2 per ITS less than 36. To get rid of contamination from beam-background events and secondary particles coming from weak decays the distance of closest approach between the track and the primary vertex has applied, which need to be less than 2 cm along the beam direction (DCAz) and less than 0.0105 + $0.035p_T^{-1.1}$(p_T in GeV/c) in the xy-plane (DCAxy). The ratio of number of crossed rows to number of findable clusters in TPC should be greater than 0.8. For the higher efficiency in the reconstruction of the track the p_T of each track is restricted to be greater than 0.15 GeV/c. Rejection of kink daughters, ITS and TPC refit are required for primary pion selection.

The charged particles are identified using TPC by measuring the specific ionisation energy loss (dE/dx). In the previous chapter this is discussed in detail. Pions and kaons can be differentiated below momentum, $p < 0.7$ GeV/c, and protons below, $p < 1$ GeV/c. The primary pions are identified through their energy loss dE/dx in the TPC. For this analysis a fixed $|N\sigma_{TPC}| < 3\sigma$ cut is applied throughout the whole momentum range for primary pions of both the energies $\sqrt{s} = 5.02$ and 8 TeV.

3.2.4 V^0 selection

Basically two types of selection criteria have been used in the analysis for the selection of V^0 particles (K_S^0) [110]. The criteria for daughter tracks (pions) from weak decay of K_S^0 ($c\tau = 2.68$ cm) are shown in Table 3.2. The selection criteria for V^0s are listed in Table 3.3. The topology for the decay of a V^0 particle is shown in Fig. 3.6. As V^0 is a neutral particle and hard to detect directly, some topological cuts are used to select the weakly decayed charged daughters (pions) of K_S^0 and also cuts are used for the selection of V^0 particle itself. For the selection of V^0 daughters, tracks need to have at least 70 reconstructed points in the TPC, out of the maximum 159 points. Rejection of kink daughters and TPC refit flag chosen to be ON and the tracks pseudo-rapidity should be within $|\eta| < 0.8$. A TPC crossed rows per findable clusters ratio less than 0.8 is applied. Now some restrictions have been applied to select V^0. The V^0 particles, which are reconstructed using the offline finder, are selected after coupling of the secondary tracks. The rapidity of the V^0 particles should be within $|y| < 0.5$. The DCA cut of 1σ is used between the positive and negative daughter tracks of V^0 to increase the possibility that, they originate from a single vertex. A 0.06 cm DCA to primary vertex cut is applied for the V^0 daughters to distinguish the tracks from primary one. The proper lifetime of the K^0_S is chosen to be less than 20 cm and a cosine of pointing angle ($cos\alpha$) > 0.97 is imposed. The Particle Identification (PID) criteria for all decay daughters are based on the requirement that, the specific energy loss (dE/dx) is measured in the TPC within five standard deviations (TPC) from the expected value $(\mathrm{dE/dx})_{\mathrm{exp}}$ [109].

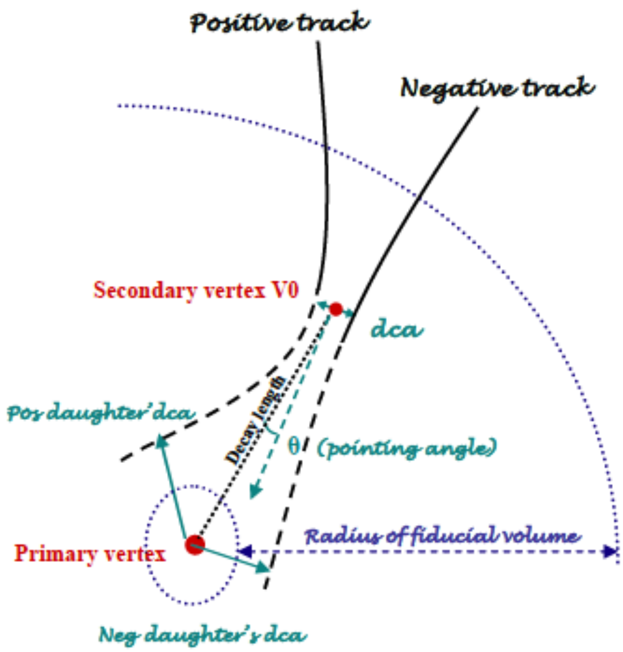

Figure 3.6: Topology of a decaying V^0 particle [111].

K^0_S **mass tolerance cut:** Instead of a fixed mass tolerance cut, we have now implemented a p_T dependent function for this cut. A simultaneous analysis has been done in [112] for the $K^{*\pm}$ measurement at $\sqrt{s} = 13$ TeV. To homogenise the analysis strategy across all the three energies for the paper on "Energy dependence of $K^*(892)^{\pm}$ production in pp collisions at $\sqrt{s} = 5.02$, 8 and 13 TeV" for ALICE collaboration [113] almost similar cutsets are used. Similarly, a same p_T dependent mass tolerance cut has to be set for the selection of K^0_S. The p_T dependent function is achieved by following the procedure described below. First, the invariant mass of K_S^0 has been drawn for 19 different p_T-bins ((0 - 0.3), (0.3 - 0.7), (0.7 - 1.2), (1.2 - 1.4), (1.4 - 1.6), (1.6 - 1.8), (1.8 - 2.0), (2.0 - 2.4), (2.4 - 2.8), (2.8 - 3.2), (3.2 - 3.6), (3.6 - 4.0), (4.0 - 5.0), (5.0 - 6.0), (6.0 - 7.0), (7.0 - 8.0), (8.0 - 10.0), (10.0 - 12.0, (12.0 - 15.0)) GeV/c for all the three energies $\sqrt{s}$ = 5.02, 8 and 13 TeV. For each p_T-bin, the mass and width parameters are extracted by fitting the invariant mass histogram of K_S^0 with a Gaussian function for the peak and a first order polynomial function for the background. The mass vs. p_T and width vs. p_T plots for all the 3 energies 5.02, 8 and 13 TeV are fitted with suitable functions. The mass vs. p_T for 13 and 8 TeV behave in a similar way, and hence a single function, which is a function of V^0 p_T, $f(v0p_T) = A + B \times log(v0p_T)$ is used for fitting and for 5.02 TeV another fit of the same functional form is used. In total 2-sets of parameters are extracted. Again the functional form has different dependency upto $v0p_T < 0.15$ GeV/c, it has the above mentioned functional form and a constant (pol0), for $v0p_T > 0.15$ GeV/c. The fittings are shown in Fig. 3.7a. The markers and fits are shown in the legends of the figure. The black solid line is the fitting function: $A + B \times log(v0p_T)$ to the mean of 13 and 8 TeV points, and the red dotted line is the fitting to 5.02 TeV. The width vs. p_T for all the energies follow a similar linear trend, so a polynomial function of first order has been fitted with the mean width of all the three energies. The pol1 function is shown by the red solid line in Fig. 3.7b.

Table 3.2: V^0 daughter tracks selection criteria.

Selection	Value
Number of TPC Crossed Rows	> 70
TPC Crossed Rows / Findable Ratio	> 0.8
TPC Refit flag	kTRUE
Track KinkIndex	> 0
Number of findable clusters	> 0
$\lvert\eta\rvert$	< 0.8

Then the parameters extracted from the function after fitting the

Table 3.3: The selection criteria parameters for K^0_S candidates. DCA stands for distance of closest approach, PV means primary vertex, PA is the pointing angle. The proper lifetime mL/p is calculated with m as the expected V^0 mass, L the linear (3D) distance between the primary vertex and the V^0 decay vertex, and p is the total momentum of the candidate. A window of about 4.3σ around nominal Λ mass value is selected for competing V^0 rejection. A cut on the mass is used to select K^0_S candidates.

Selection	Value
Offline or On-The-Fly	Offline
$\lvert y \rvert$	< 0.8
V0 2D decay radius	> 0.5 cm
DCA of daughter to PV	> 0.06 cm
DCA V0 daughters(σ)	< 1
V0 Cosine of Pointing Angle	> 0.97
Proper Lifetime (mL/p)	< 20 cm
Competing V0 Rejection(MeV/c^2)	± 4.3
Mass K^0_S window(σ)	± 4
TPC dE/dx selection	$< 5\sigma$

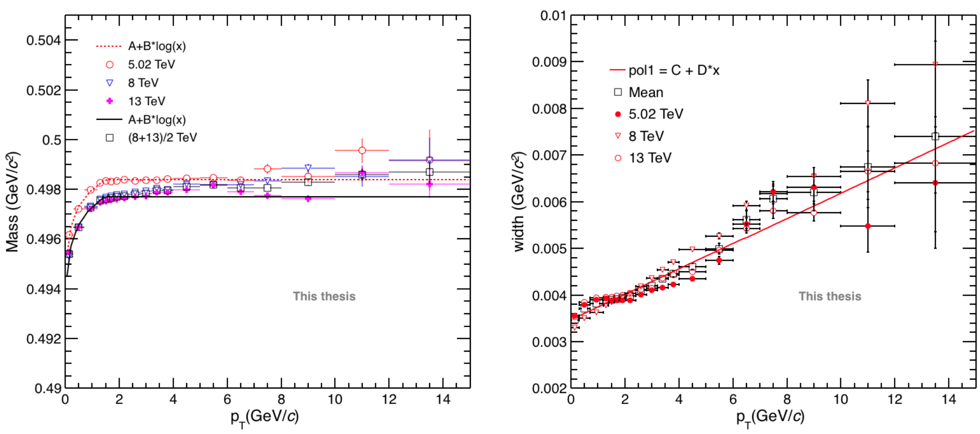

(a) K^0_S mass parameter vs. p_T.

(b) K^0_S width parameter vs. p_T.

Figure 3.7: Extracted mass and width parameter from K^0_S invariant mass fitting for setting the p_T dependant mass tolerance cut [107].

mass and width vs. p_T plots are used to prepare the parametric mass and width cut for the selection of K^0_S. The functional form is as follows:

if(v0pT<=1.5){

if(v0pT < 0.15) {//To take care of the log function at very low-p_T

Double_t lUpperLimitK0Short = A + B × log(v0pT) + fMassTolSigma × (C + D × v0pT) ;

Double_t lLowerLimitK0Short = A + B × log(v0pT) - fMassTolSigma × (C + D × v0pT); }

else {

Double_t lUpperLimitK0Short = A + B × log(1.5) + fMassTolSigma × (C + D × v0pT) ;

Double_t lLowerLimitK0Short = A + B × log(1.5) - fMassTolSigma × (C + D × v0pT); }

}

A 4σ cut on the mass tolerance of K_S^0 has been used for the default setting of the analysis. Figure. 3.8 shows the mass vs. p_T spread before and after the cut is applied. These cuts make sure that genuine K_S^0 particles are taken for the analysis.

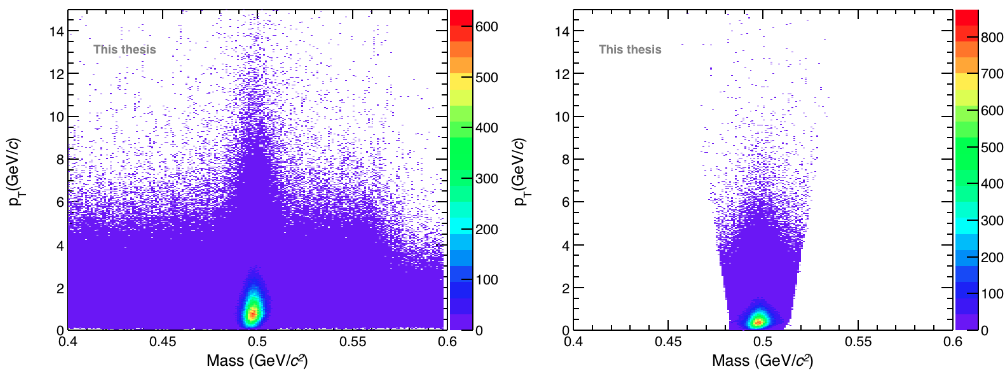

(a) Before (b) After

Figure 3.8: Plots showing the effect of p_T-dependent mass tolerance cut on K_S^0 selection [107].

3.3 Invariant mass reconstruction

The invariant mass distribution of $K^{*\pm}$ is reconstructed by the invariant mass of K_S^0 and pion pairs from the same events. The kinematics of the reconstruction of $K^{*\pm}$ and its V^0 (K^0_S) particle is,

$$M^2_{K^{*\pm}} = (E_{\pi^\pm} + E_{K^0_S})^2 - (|\overrightarrow{p}_{\pi^\pm}| + |\overrightarrow{p}_{K^0_S}|)^2, \tag{3.1}$$

$$M^2_{K^0_S} = (E_{\pi^+} + E_{\pi^-})^2 - (|\overrightarrow{p}_{\pi^+}| + |\overrightarrow{p}_{\pi^-}|)^2, \tag{3.2}$$

where $E_{\pi^\pm} = \sqrt{m^2_{\pi^\pm} + |\overrightarrow{p}_{\pi^\pm}|^2}$ and $E_{K^0_S} = \sqrt{m^2_{K^0_S} + |\overrightarrow{p}_{K^0_S}|^2}$.

The raw yield of $K^{*\pm}$ is estimated in the following 19 p_T-bins ((0 - 0.3), (0.3 - 0.7), (0.7 - 1.2), (1.2 - 1.4), (1.4 - 1.6), (1.6 - 1.8), (1.8 - 2.0), (2.0 - 2.4), (2.4 - 2.8), (2.8 - 3.2), (3.2 - 3.6), (3.6 - 4.0), (4.0 - 5.0), (5.0 - 6.0), (6.0 - 7.0), (7.0 - 8.0), (8.0 - 10.0), (10.0 - 12.0, (12.0 - 15.0)) GeV/c. To extract the yields of $K^{*\pm}$ mesons in each p_T-bin, the following procedure is used. The invariant mass distribution of $K^0_S\pi^\pm$ pairs from the same event is computed. Since the resonance decay products originate from a position which is indistinguishable from the primary vertex, a significant combinatorial background is present. The background estimation is done by event-mixing method. Each analyzed event is mixed with 10 other events to avoid mismatch due to different acceptances and to assure a similar event structure. This step also reduces statistical uncertainties. Events for mixing is grouped based on several criteria: the difference in vertex-z is required to be less than 1 cm ($\Delta z < 1$ cm), while the difference in the multiplicities is required to be less than 5 ($\Delta n < 5$), which ensure to build uncorrelated pairs. Then the mixed event background is normalised with the same event distribution in the region of invariant mass (1.1- 1.2) GeV/c^2, which is more than 5Γ (width of the $K^{*\pm}$) apart from the peak region. In this region the $K^0_S\pi^\pm$ pairs are very much uncorrelated. The same and mixed event pairs have almost same structure in this region. The signal is obtained after subtracting the normalised mixed event invariant mass distribution from the same event as given below:

$$N_{K^{*\pm}} = N_{K^0_S\pi^\pm}|_{real} - N_{factor} \times \sum_{l=2}^{11} N_{K^0_S\pi^\pm}|_{mixed}, \tag{3.3}$$

where $N_{factor} = \frac{N_{K^0_S\pi^\pm}|_{real}}{N_{K^0_S\pi^\pm}|_{mixed}}|_{(1.1-1.2\ GeV/c^2)}$

In Fig. 3.9 the invariant mass distribution ($M_{K^{*\pm}}$) from same and normalised mixed events are shown. The Fig. 3.9a is the invariant mass distribution of $M_{K^{*\pm}}$ from same event and mixed events for a single lower p_T-bin (0.7 -1.2 GeV/c) at $\sqrt{s}$ = 5.02 TeV. And Fig. 3.9b shows the plot for mid p_T-bin (2.0 -2.4 GeV/c) at $\sqrt{s}$ = 8 TeV.

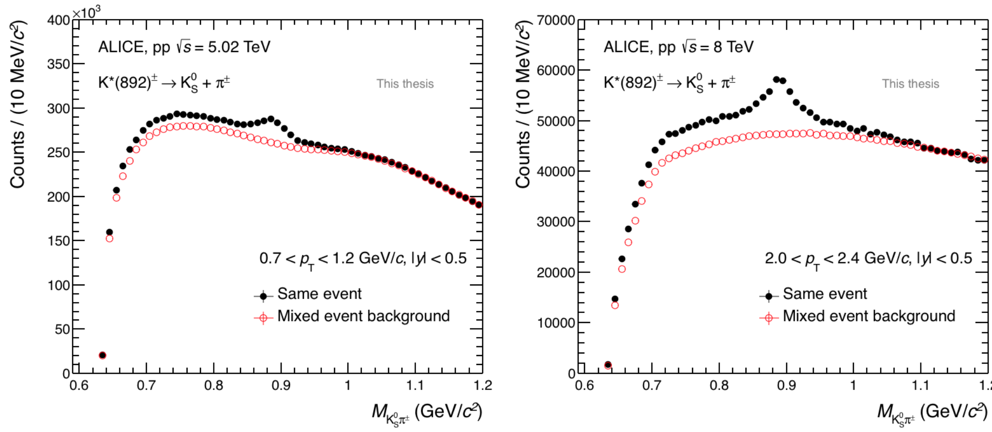

(a) For the bin 0.7 $< p_T <$ 1.2 GeV/c at $\sqrt{s}$ = 5.02 TeV.

(b) For the bin 2.0 $< p_T <$ 2.4 GeV/c at $\sqrt{s}$ = 8 TeV.

Figure 3.9: The $K^0_S\pi^\pm$ invariant mass distribution in $|y| < 0.5$ in pp collisions at $\sqrt{s}$ = 5.02 and 8 TeV. The background shape is shown by the open red circle and the black solid circles are from same events [113].

3.3.1 Residual Background

The invariant mass distribution is obtained after the subtraction of the combinatorial background, which is estimated by the event mixing from the same event distribution. However, after such an ideal background subtraction, a residual background will remain along with the $K^{*\pm}$ signal. A residual background function is required to obtain the signal. These correlated residual background has contributions from:

1. Misidentified resonances (Due to misidentification of daughter particles).
2. Other decay channels from the same resonance whose daughters overlap with the channel being studied.

3. Jets and minijets.

4. Multi-particle correlations (e.g. effect of elliptic flow).

3.3.2 $K^{*\pm}$ Yield extraction

To explain the background subtracted invariant-mass distribution a combined fit function is used. The combined function contains a peak function (Breit-Wigner) and a residual background function. The statistical significance ($\mathbb{S}$) which measures the strength of the signal, is given by,

$$\mathbb{S} = \frac{S}{S+B} = \frac{1}{\sqrt{1+1/R}}. \tag{3.4}$$

Here $R = S/B$ is the ratio of integral of signal (S) to background (B) in a common range around the signal peak. The significance is related to the signal over background ratio, that depends on the power of the kinematic selection cuts. It quantifies the signal over the statistical fluctuations of the background. It is used for achieving a high efficiency for signal as well as a high rejection power for background.

The residual background shape for the different p_T-bins are extracted from Monte Carlo simulated data. Different kind of functions were tested as residual background functions, e.g., second and third order polynomials. However the best parameterisation of the background is given by the function [114].

$$F_{BG}(M_{K^0_S\pi^\pm}) = [M_{K^0_S\pi^\pm} - (m_K + m_\pi)]^n exp(A + BM_{K^0_S\pi^\pm} + CM_{K^0_S\pi^\pm}). \tag{3.5}$$

The total fit function is given by,

$$\frac{dN}{dM_{K^0_S\pi^\pm}} = \frac{Y}{2\pi} \frac{\Gamma}{(M_{K^0_S\pi^\pm} - M_{K^{*\pm}})^2 + \frac{\Gamma^2}{4}} + F_{BG}(M_{K^0_S\pi^\pm}). \tag{3.6}$$

Here $M_{K^{*\pm}}$ and Γ are the PDG mass and width of the $K^{*\pm}$, respectively. $M_{K^0_S\pi^\pm}$ is the invariant mass and Y gives the Breit-Wigner area from 0 to ∞. The last term of Eq. 3.6 is the residual background function, which is an exponential of second order polynomial in the invariant mass (Eq. 3.5). $m_\pi = 139.57018$ GeV/c^2 and $m_K = 497.611$ GeV/c^2 are the pion and K^0_S mass and n, A, B and C are fit parameters. To have a good fit the width of $K^{*\pm}$ (50.8 MeV/c^2) is kept fixed to its PDG value. The fitting range is chosen accurately for each p_T-bin to improve the global χ^2 of the fit. For a large part of the p_T-bins the fit range is 0.66 - 1.1 GeV/c^2. The results of the fit for different p_T-bins are reported in Fig. 3.10.

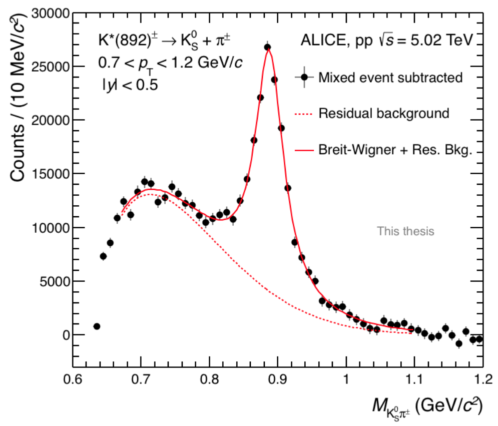

(a) For the bin $0.7 < p_T < 1.2$ GeV/c at $\sqrt{s} = 5.02$ TeV.

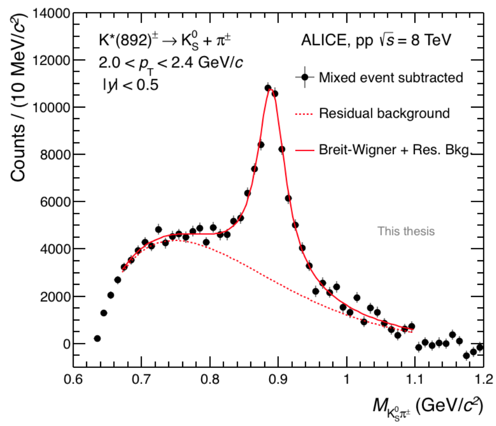

(b) For the bin $2.0 < p_T < 2.4$ GeV/c at $\sqrt{s} = 8$ TeV.

Figure 3.10: The $K^0_S\pi^\pm$ invariant mass distribution in $|y| < 0.5$ in pp collisions at $\sqrt{s} = 5.02$ and 8 TeV. The background shape is shown by the red dashed line and the signal by red solid line [113].

The raw yield of $K^{*\pm}$ is calculated using two different methods: the fit function (Y_{FI}) method or bin counting (Y_{BC}) method. The second method is used as default and the first is used for systematic study.

3.3.3 Function Integral (Y_{FI}):

The expression of raw yield using function integral method is given as,

$$Y_{FI} = Y - \int_0^{(m_\pi + m_K)} fit(m_{inv})dm_{inv}. \tag{3.7}$$

Here, Y of the fit is the integral of the peak function from 0 to ∞, the mass region $0 < M_{K^0_S\pi^\pm} < (m_\pi + m_K)$, is kinematically forbidden. The integral in the kinematically forbidden region is about 2% of the total integral for almost all the p_T-bins, with the exact ratio which depends on the peak parameters.

3.3.4 Bin Counting (Y_{BC}):

In case of bin counting method the raw yield (N_{BC}) is given by,

$$N_{BC} = N_{counts} - N_{RB}. \tag{3.8}$$

Here N_{counts} is calculated by integrating the invariant mass histogram in the region $I_{min} < M_{K^0_S\pi^\pm} < I_{max}$ with, $I_{min} = M_0 - \Gamma_0(0.79\ \mathrm{GeV}/c^2)$ and $I_{max} = M_0 + \Gamma_0\ (0.99\ \mathrm{GeV}/c^2)$. And N_{RB} is calculated by integrating the residual background with the same limit ($I_{min} - I_{max}$). Here M_0 and Γ_0 are the PDG mass and width of $K^{*\pm}$, respectively.

The error on N_{RB} is calculated by using the `ROOT` function "$fBgOnly \rightarrow IntegralError(I_{min}, I_{max}, Par[4], CM)$", where CM is the covariance matrix, fBgOnly is the residual background function and Par[4] is a vector with the value of the parameters of the residual background function. The error in N_{counts} is calculated by the `ROOT` function GetBinError, and the error for N_{BC} is calculated by the error propagation method. The errors are added in quadrature as they are un-correlated. The correction to the raw yield from the lower and upper tail regions are respectively given by,

$$N_{low} = \int_{m_\pi + m_K}^{(M_0 - \Gamma_0)} fit(m_{inv})\, dm_{inv} \tag{3.9}$$

and

$$N_{high} = \int_{(M_0 + \Gamma_0)}^{\infty} fit(m_{inv})\, dm_{inv}. \tag{3.10}$$

With these corrections the total raw yield (N_{raw}) is given by,

$$N_{raw} = N_{BC} + N_{low} + N_{high}. \tag{3.11}$$

Since N_{BC}, N_{low} and N_{high} are correlated, the total error for N_{raw} is calculated by adding the errors linearly.

3.4 Simulation

A simulated dataset is analyzed in order to extract "$K^{*\pm}$ reconstruction efficiency × acceptance", ($\varepsilon_{rec} \times A$). For $\sqrt{s}$ = 5.02 TeV two simulated datasets (ESD) are available, i.e., LHC16k5a production (Monash 2013 tune of PYTHIA 8) with 49 million events and LHC16k5b production (Perugia 2011 tune of PYTHIA 6) with 45 million events. For $\sqrt{s}$ = 8 TeV, only one production LHC15h1a1_1b_1c_1d_1h_1i with about ∼ 106 million events is available, which is a Monash 2013 tune of PYTHIA 8. Particle production and decays are simulated using the event generators PYTHIA 8, PYTHIA 6, PHOJET etc. To take care of the effect of detector geometry the particle interactions with the ALICE detector are simulated using the Monte Carlo transport packages GEANT3 [98], GEANT4 [99], FLUKA [100] etc. For both the real and the simulated data, same event selection criteria, track quality cuts and topological cuts are used. The particles produced by the event generator (without any detector effects) are referred as "generated particles". These generated particles are the input for the GEANT3 detector simulation. The tracks which are identified by the reconstruction algorithms after passing all the selection criteria are referred as "reconstructed tracks". A reconstructed $K^{*\pm}$ meson is a particle for which both the daughters have been reconstructed via GEANT3 simulations.

3.5 Correction and Normalization of Spectra

3.5.1 Acceptance × Efficiency

The reconstruction acceptance × efficiency, denoted by ε_{rec}, was calculated using available simulation and analysed datasets. In each transverse-momentum bin ε_{rec} is given by,

$$\varepsilon_{rec} = \frac{N_{Reconstructed}}{N_{Generated}}. \tag{3.12}$$

Here $N_{Generated}$ is the number of generated $K^{*\pm}$ mesons with $|y| < 0.5$ that decay to a K^0_S and a charged pion ($\pi^{\pm}$). $N_{Reconstructed}$ is the number of reconstructed $K^{*\pm}$ mesons in the same rapidity range $|y| < 0.5$. The $K^{*\pm}$ acceptance $\times$ efficiency distribution as a function of p_T is shown in the Fig. 3.11.

In left panel of Fig. 3.11 the efficiency of the two general purpose Monte Carlo (MC) production, PYTHIA 8 and PYTHIA 6 along with their average efficiency has been shown. For the correction of the raw yield at $\sqrt{s}$ = 5.02 TeV the average efficiency from the two MC production has been taken into account.

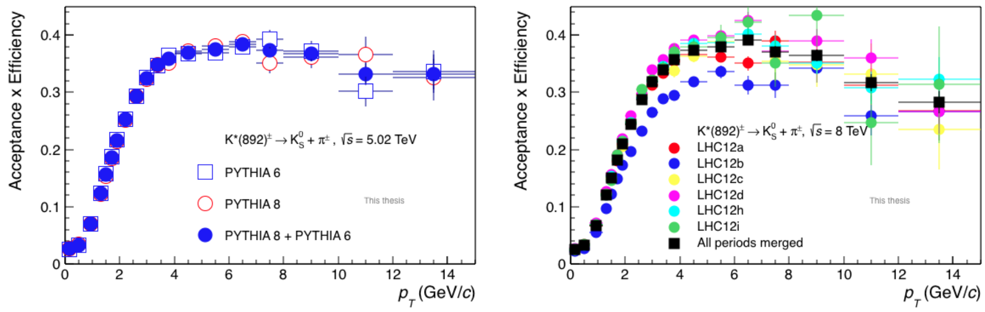

(a) Efficiency for $\sqrt{s}$ = 5.02 TeV.   (b) Efficiency for $\sqrt{s}$ = 8 TeV.

Figure 3.11: The efficiency in pp collisions at $\sqrt{s}$ = 5.02 and 8 TeV as a function of p_T [107, 108]. Details of the plots are described in the text.

Since the "generated" and "reconstructed" particles are coming from the same events and one is a subset of another, the numerator and denominator of Eq. 3.12 are correlated. The uncertainty in ε_{rec} has been calculated using the Bayesian approach [115]. The standard deviation of the efficiency ($\varepsilon_{rec} = k/n$) is a function of k and n, and is given as

$$\sigma_{\varepsilon} = \sqrt{\frac{k+1}{n+2}\left(\frac{k+2}{n+3} - \frac{k+1}{n+2}\right)}. \tag{3.13}$$

Here the numerator k is a subset of the denominator n. The fractional statistical uncertainty in ε_{rec} was added in quadrature with the statistical uncertainty of the uncorrected $K^{*\pm}$ yield to give the total statistical uncertainty of the corrected $K^{*\pm}$ yield. It has a strong dependence on transverse momentum at low-p_T.

The above mentioned procedure is applicable to $\sqrt{s}$ = 5.02 TeV, whereas the similar approach with a little modification has been used to calculate the final efficiency at $\sqrt{s}$ = 8 TeV. Since the $\sqrt{s}$ = 8 TeV case has 6 different simulation periods (LHC15h1a1 -..- LHC15h1i) corresponding to different data periods (LHC12a -..- LHC12i), we combine the efficiency calculated from each dataset to get the efficiency for all the periods. The final efficiency from all the 6-periods has been calculated by taking weighted average of the efficiency of each period. In Fig. 3.11b the efficiency for all the 6-analysed periods are shown. For 8 TeV, only one general purpose MC production of PYTHIA 8 is available. The efficiency for each data period and its associated uncertainty following the above mentioned procedure has been shown by solid circles of different colors along with the final efficiency which is used to correct the raw yield of $K^{*\pm}$ at 8 TeV. The final efficiency has been shown by the black solid square in the figure and is calculated by using the expressions,

$$\varepsilon_{allperiods} = \sum w_i \varepsilon_i(p_T). \tag{3.14}$$

And the uncertainty is calculated as,

$$\sigma_{\varepsilon_i} = \sqrt{\sum w_i \sigma_i(p_T)} \tag{3.15}$$

3.5.2 Reweighted Acceptance × Efficiency

If the generated spectrum has a different shape than the measured resonance spectrum, it is necessary to weight the generated and reconstructed spectra. The generated and measured $K^{*\pm}$ spectra have very different behaviours for the range $0.4 < p_T < 1$ GeV/c. Figure 3.12 shows the generated $K^{*\pm}$ spectra (average of the two p_T-spectra, i.e.

$(K^{*+} + K^{*-})/2)$ plotted with the efficiency corrected $K^{*\pm}$ spectrum. The Lévy-Tsallis fit of the measured spectrum is also shown in the same figure. The standard resonance macro for the reweighting is used (`ALICEPHYSICS/PWGLF/RESONANCES/macros/utils/ReweightEfficiency.C`).

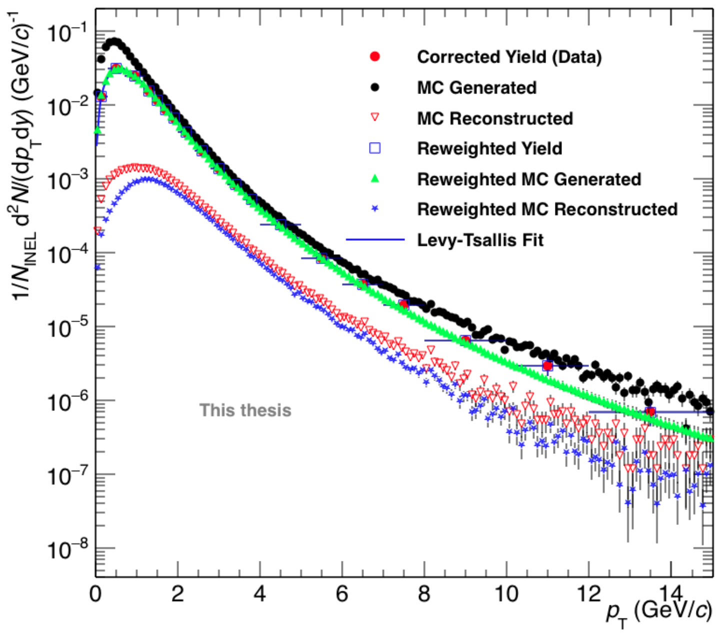

Figure 3.12: Corrected $K^{*\pm}$ spectrum (red circles) with Lévy-Tsallis fit (blue curve). The unweighted generated (black circles) distribution is compared to the reweighted distribution (Green solid triangle). The unweighted reconstructed (inverted triangle) distribution and the reweighted distribution (blue star) are also shown [107].

In this macro the generated and reconstructed spectra, which are used to estimate the ε_{rec} and to determine the weighting factor to correct ε_{rec} with the following iterative procedure.

1. The unweighted ε_{rec} is calculated using the generated and reconstructed $K^{*\pm}$ spectra.

2. This ε_{rec} is used to correct the measured $K^{*\pm}$ spectrum.

3. The corrected $K^{*\pm}$ spectrum is fitted using a Lévy-Tsallis function.

4. This Lévy-Tsallis fit is used to weight the simulated $K^{*\pm}$ spectra. A p_T-dependent weight is applied to the generated spectrum so that

it follows the fit. The same weight is applied to the reconstructed spectrum.

5. The (weighted) ε_{rec} is calculated.

6. Steps 2-5 are repeated (with the weighted ε_{rec} from step 5 used as the input for step 2) until the ε_{rec} values are observed to change by less than 0.1% between iterations. It was observed that two iterations are usually sufficient for this procedure to converge.

In the Fig. 3.13 the weighted and unweighted efficiencies are compared for both the energies. Their ratio is plotted in the lower panel. The difference in the reweighted efficiency to the unweighted efficiency can only be found for $p_T < 1$ GeV/c, which reflects the shape difference in the simulated spectra with the measured spectra.

3.5.3 Signal-loss correction

The signal-loss correction ε_{SL} accounts for the loss of $K^{*\pm}$ mesons incurred by selecting events that satisfy the kINT7 trigger, rather than all inelastic events. So, application of this factor allows the inelastic p_T-spectrum to be recovered. This is a p_T-dependent correction factor which is peaked at low-p_T, indicating that events that fail the kINT7 selection have softer $K^{*\pm}$ p_T-spectra than the average inelastic events. The expression of ε_{SL} is,

Numerator: The generated $K^{*\pm}$ mesons p_T-spectrum from inelastic events, with a cut on the z-position of the generated primary vertex $|v_{z,gen}| < 10$ cm.

Denominator: The generated $K^{*\pm}$ mesons p_T-spectrum after the kINT7 trigger is applied with all the event-selection cuts (including the cut on the z-position of the reconstructed primary vertex) have been applied. This is the same quantity in the denominator for the calculation of ε_{rec}.

For $\sqrt{s} = 5.02$ TeV, ε_{SL} is estimated using two different available productions: LHC16k5a (PYTHIA 8) and LHC16k5b (PYTHIA 6). The

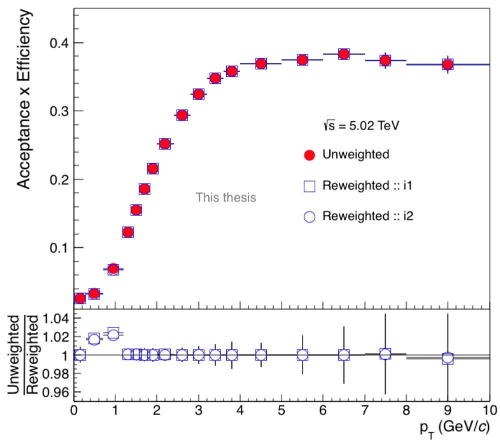

(a) Efficiency comparison at $\sqrt{s} = 5.02$ TeV.

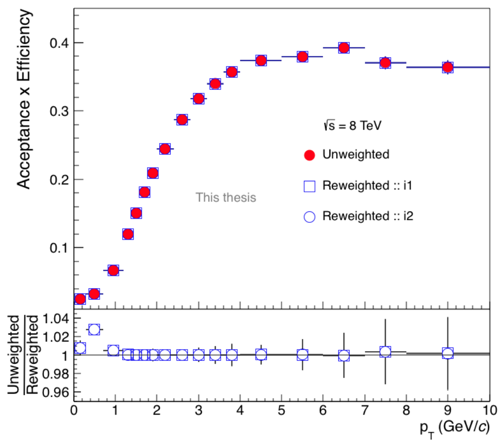

(b) Efficiency comparison at $\sqrt{s} = 8$ TeV.

Figure 3.13: Top panel of each figure shows the unweighted and reweighted efficiency in pp collisions at $\sqrt{s} = 5.02$ and 8 TeV. Lower panel of each figure demonstrate the ratio of the unweighted to the reweighted efficiency [107, 108].

two simulation productions produce slightly different ε_{SL} values. The correction from PYTHIA 8 production is used as default and for each p_T-bin an associated uncertainty has been set. The associated uncertainty is given as,

$$U_{\varepsilon_{SL}} = max\left[\frac{1}{2}\left[\varepsilon_{SL}(LHC16k5a) - 1\right], |\varepsilon_{SL}(LHC16k5a) - \varepsilon_{SL}(LHC16k5b)|\right]. \tag{3.16}$$

The maximum value between these quantities in Eq. 3.16 is assigned as the uncertainty of ε_{SL} for that particular p_T-bin. For $\sqrt{s} = 8$ TeV, ε_{SL} is calculated from the Monash 2013 tuned PYTHIA 8 MC production, LHC15h1a1_b1_c1_d1_h1_i1 following the same procedure. Here the uncertainty in ε_{SL} is $\frac{1}{2}\left[\varepsilon_{SL}(LHC15h1a1\_b1\_c1\_d1\_h1_i1) - 1\right]$. The obtained p_T distributions of the signal-loss correction with the different Monte Carlo production are shown in Fig. 3.14. Fig. 3.14a shows signal loss correction for $\sqrt{s}$ = 5.02 TeV and Fig. 3.14b for $\sqrt{s}$ = 8 TeV. At low-p_T region they are slightly different, maximum upto 3%. To be uniform with other resonance analyses at the same collision energy, the ε_{SL} distribution obtained with PYTHIA8 was used to estimate the $K^{*\pm}$ inelastic p_T-spectrum.

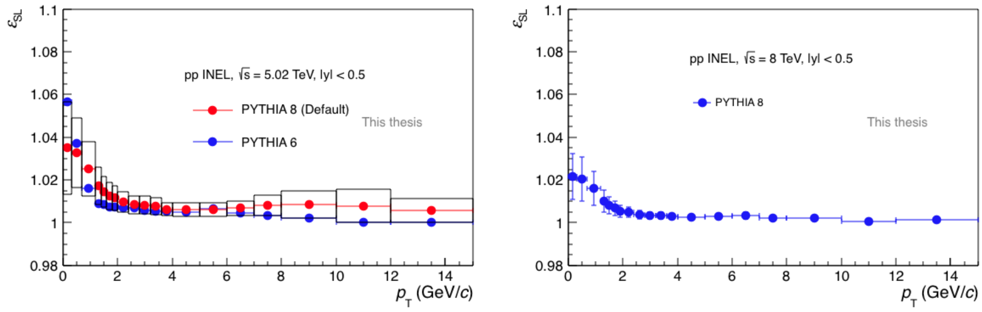

(a) For $\sqrt{s}$ = 5.02 TeV.

(b) For $\sqrt{s}$ = 8 TeV.

Figure 3.14: Signal-loss correction in pp collisions at $\sqrt{s}$ = 5.02 and 8 TeV [107, 108].

3.5.4 Inelastic Normalization

The inelastic normalization factor, f_{norm} is calculated in order to normalize the yield to the number of inelastic pp collisions. This is needed to convert a particle yield normalized to the number of triggered events to a yield normalized to the number of inelastic events. The full procedure and calculation is done in Ref. [116]. The inelastic normalization factor is the ratio of the V0 visible cross section to the inelastic cross section, which is given as

$$f_{norm} = \frac{\sigma_{V0AND}}{\sigma_{inel}}. \tag{3.17}$$

Here, σ_{V0AND} and σ_{inel} are the V0 visible cross section and pp inelastic cross section, respectively. The total number of inelastic events N_{inel} is given by

$$N_{inel} = N_{V0AND} \times \frac{\sigma_{inel}}{\sigma_{V0AND}}. \tag{3.18}$$

Here, N_{V0AND} is the total number of events from V0AND detector. To get N_{inel}, the measured p_T-spectrum is multiplied to the f_{norm} factor. For the energies $\sqrt{s} = 5.02$ and 8 TeV, σ_{V0AND} values are 51.2 mb $\pm$ 2.3 % and 55.8 mb $\pm$ 2.6 %, respectively. The inelastic cross sections for pp collisions at $\sqrt{s} = 5.02$ and 8 TeV are (67.6 ± 0.6) mb and (72.3 ± 0.3) mb respectively, and are taken from Ref. [117]. The uncertainties of both the terms for the calculation of f_{norm} are uncorrelated. The inelastic normalization factor for $\sqrt{s} = 5.02$ TeV is taken to be $f_{norm} = 0.7574 \pm 00190$ (2.51%) and for $\sqrt{s} = 8$ TeV is taken to be $f_{norm} = 0.7718 \pm 0.02075$ (2.69%). This factor takes into account the efficiency for trigger selection for inelastic pp collisions.

3.6 Systematic uncertainty study

The systematic uncertainty study is performed using the grouping procedure described in Ref. [118]. For the estimation of systematic uncertainties multiple variations are considered for each analysis setting. The sources of systematic uncertainty from the variations of settings are divided into groups, and other sources which are not correlated to the variations of analysis settings are remained ungrouped.

The measurements are performed with one or more analysis parameters changed, for example, PID cuts, a fitting range, the form of a fitting function etc. And the measurements are considered which are not statistically independent, i.e., obtained from the same data set or at least data sets with large amounts of overlap. The systematic uncertainties are calculated by finding the differences between the “default” measurement which is one measurement or an average and the other “alternate” measurements. However, an alternate measurement, which is statistically consistent with the default measurement should not be used in calculating a systematic uncertainty. Since the alternate and default measurements are not statistically independent, a check is needed to know whether they are consistent within their statistical uncertainties. It is not trivial to check if their uncertainties overlap. The "Barlow test" is performed to distinguish systematic uncertainties from statistical uncertainties [119].

Let us consider two cases, where one measurement is due to the default settings Y_{def} and another is due to the alternative systematic measurements Y_{sys}. The statistical error σ_{def} and σ_{sys} are associated with Y_{def} and Y_{sys}, respectively. The difference between the yields is denoted as $\Delta = Y_{def} - Y_{sys}$ and the quadrature difference of their statistical error is $\sigma_{cc} = \sqrt{\sigma_{def}^2 - \sigma_{sys}^2}$. Now, this Δ/σ_{cc} is calculated for each p_T-bin. In general, if two measurements are consistent, it is expected that the distribution of Δ/σ_{cc} when plotted, would have a mean near 0, a standard deviation near 1, and 68% of the entries would lie within $\Delta/\sigma_{cc} < 1$. But the values can be set according to the analyser with a slight deviations. So, in this work the values are different as mentioned in the following lines. For this analysis we consider a source as a systematic source if three out of four criteria of the distribution $|\Delta/\sigma_{cc}|$ have failed. The criteria are as follows:

1. $\langle \Delta/\sigma_{cc} \rangle < 0.1$
2. $\sigma_{cc} < 1.1$
3. fraction of entries within $\pm 1\sigma$: $I_1 > 55$
4. fraction of entries within $\pm 2\sigma$: $I_2 > 90$.

For the p_T-spectrum the following sources of systematic uncertainty were considered: signal extraction, primary track selection, PID cuts, topological cuts for K_S^0, event selection, material budget, hadronic interaction, signal-loss correction, global tracking uncertainty etc. The general strategy for evaluating systematic uncertainties for the p_T-spectrum is described in Ref. [118].

A smoothing procedure has also been applied thereafter as the systematic uncertainties exhibit a few large fluctuations from bin to bin. In the smoothing procedure the mean value of fractional uncertainties of the $(i-1)^{th}$ and $(i+1)^{th}$ bins is assigned to the i^{th} p_T-bin. The sources of systematic uncertainties are divided into four groups, i.e., PID Strategy, Primary track selection cuts, Topological track cuts, Signal extraction. A brief description of the sources of systematic uncertainties are given below.

Systematic due to PID strategy

The primary pions are selected using the TPC average energy loss ($\langle dE/dx \rangle$) within three standard deviation (σ). The number of standard deviation, N_σ is varied on both side of the default cut for this analysis, i.e., $|N_\sigma| < 2.5$ and $|N_\sigma| < 3.5$. During the Barlow test it is passed to the criteria, so it is not included in the systematic estimation for both the energies $\sqrt{s} = 5.02$ and 8 TeV.

Systematic due to primary cuts

The systematic uncertainty due to the primary track selection are estimated by changing some parameters one by one. For example, minimum number of rows crossed in TPC, ratio of number of crossed rows to number of findable clusters in TPC, TPC and ITS χ^2/clusters, DCA_z and DCA_{xy} cuts. For each cuts two or three variations are taken for the systematic calculation due to primary cuts. The systematic uncertainty due to primary cuts varies from 2 - 5% depending on p_T.

Systematic due to topological cuts

To estimate the systematic due to the V^0 selection, some parameters were varied one by one using the maximum and minimum variations adopted for studying K^0_S systematics. For example, fiducial volume (V^0 2D decay radius), cosine of pointing angle, DCA V^0 daughters, V^0 mass tolerance, lifetime and DCA V^0 to Primary Vertex. The systematic uncertainty due to topological cuts varies from 2 - 10% depending on p_T.

Systematic due to signal extraction

To estimate the systematic due to the signal extraction some parameters were varied one by one. The examples are normalisation range, residual background function and fit region etc. The systematic uncertainty due to signal extraction varies from 2 - 10% depending on p_T.

Systematic due to Global tracking efficiency

The tracking uncertainty, due to the uncertainty in ITS-TPC matching, for the $K^{*\pm}$ is derived as follows. The one-particle uncertainty u($p_{T\pi^\pm}$) is inherited from the analysis of unidentified charged hadron production in the same collision system [120]. A PYTHIA simulation is used to find the p_T distributions of the primary pions from the $K^{*\pm}$ decays. These p_T distributions, $p_{T\pi^\pm}$ were then used to obtain the weighted average of the tracking uncertainty for each $K^{*\pm}$ p_T-bin.

Let w($p_{TK^{*\pm}}$) be the ratio between the measured and generated $K^{*\pm}$ p_T spectra. Let $N(p_{TK^{*\pm}}, p_{T\pi^\pm})$ be the number of $K^{*\pm}$ with $p_{TK^{*\pm}}$ that decay to pions with $p_{T\pi^\pm}$. The one-particle tracking uncertainty is the ratio of two histograms (a weighted average):

Numerator: $\Sigma_{generated\ K^{*\pm}}(N(p_{TK^{*\pm}}, p_{T\pi^\pm}) \times w(p_{TK^{*\pm}}) \times u(p_{T\pi^\pm}))$,

Denominator: $\Sigma_{generated\ K^{*\pm}}(N(p_{TK^{*\pm}}, p_{K^{*\pm}T\pi^\pm}) \times w(p_{TK^{*\pm}}))$.

The distribution of the uncertainty due to the global tracking as a function of p_T is shown in Fig. 3.15. For $\sqrt{s}$ = 5.02 TeV, the above mentioned uncertainty is used. Since in case of $\sqrt{s}$ = 8 TeV, p_T dependent results for one-particle uncertainty is not available, a constant 3% uncertainty is taken .

Systematic due to material budget

The systematic uncertainty due to the ALICE material budget is estimated by taking material budget uncertainty of K^0_S from [121] and for pions taking

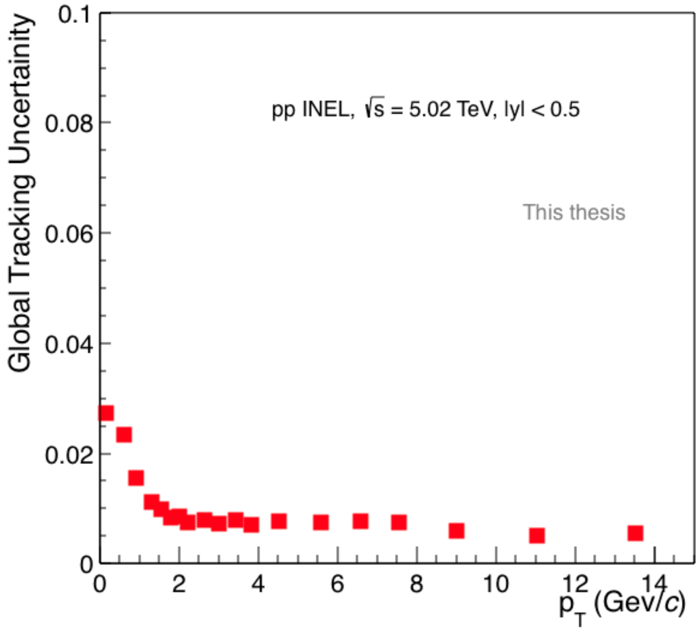

Figure 3.15: Global tracking uncertainty for $\sqrt{s}$ = 5.02 TeV as a function of p_T [107].

uncertainty from [122]. The uncertainty associated to ALICE material budget is about 4% for low-p_T ($<$ 2 GeV/c) and negligible at high-p_T. The estimated material budget uncertainty is shown in Fig. 3.16.

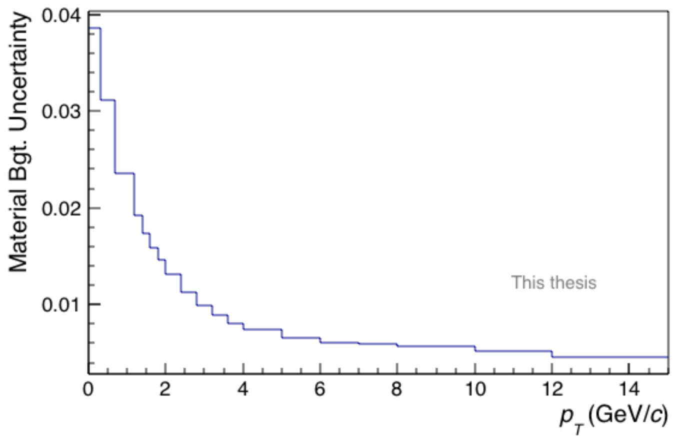

Figure 3.16: Estimated material budget uncertainty for $K^{*\pm}$ as a function of p_T [112].

Systematic due to primary vertex selection

This systematic uncertainty due to primary vertex selection takes into account for the differences observed in the yield due to variations in the z-position cut of the primary vertex. In the standard event cut set $|v_z| <$ 10 cm. Two variations were considered for the systematic study: $|v_z| < 8$ cm and $|v_z|$ <12 cm. The uncertainty is excluded from the calculation of total systematic uncertainties as it passes the Barlow test.

3.6.1 Total systematic uncertainty

The systematic uncertainties from different sources were added in quadrature to obtain the total systematic uncertainty. The p_T-distributions of the systematic uncertainty of the different sources previously described are shown in Fig. 3.17. In the same figure the p_T-distribution of the total systematic uncertainty estimated for the $K^{*\pm}$ production in pp collisions is shown. In Table 3.4 the fractional uncertainty is quoted in percentage for each uncertainty sources for the full p_T-range.

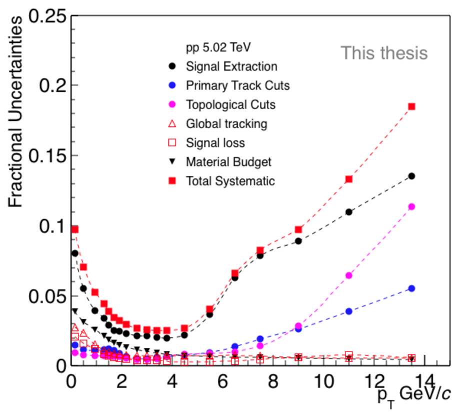

(a) For $\sqrt{s} = 5.02$ TeV.

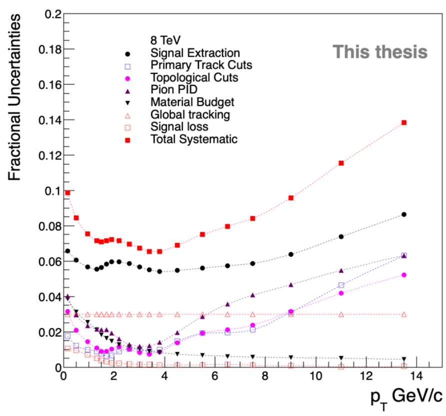

(b) For $\sqrt{s} = 8$ TeV.

Figure 3.17: Summary of fractional systematic uncertainty at $\sqrt{s} = 5.02$ and 8 TeV [107, 108].

Table 3.4: Main sources and weighted values of the relative systematic uncertainties (expressed in %) of the differential yield of $K^{*\pm}$ resonance at the two studied energies for full p_T-range.

$\sqrt{s}$ (TeV)	5.02	8
p_T (GeV/c)	0 - 15	0 - 15
Global tracking efficiency (%)	1	3
Signal extraction (%)	4.8	5.9
Primary pion identification (%)	1.5	1.05
K^0_S identification (%)	1.7	1.6
Material budget (%)	1.3	1.36
Signal Loss (%)	0.7	0.65
Total (%)	5.9	7.8

3.7 Corrected p_T-spectrum

The $K^{*\pm}$ meson spectra are normalized as follows. The differential transverse momentum spectrum for inelastic pp collisions are estimated by

$$\frac{d^2N}{dp_T dy} = \frac{N_{raw}}{N_{MB} \times BR \times \Delta p_T \times \Delta y} \frac{\varepsilon_{SL}}{\varepsilon_{rec}} \times f_{norm} \times f_{vertex}, \tag{3.19}$$

where $\Delta y = 1$, N_{MB} is the number of minimum-bias analysed events , branching ratio $= 0.66 \times 0.5 = 0.33$ for $K^{*\pm} \rightarrow K^0_S + \pi^{\pm}$ channel, ε_{rec} is the reweighted acceptance $\times$ efficiency. The signal-loss correction ε_{SL} accounts for the loss of $K^{*\pm}$ mesons incurred by selecting events that satisfy the kINT7 trigger, rather than all inelastic events. The factor f_{norm} is applied in order to normalize to the number of inelastic pp collisions. The factor f_{vtx}= 0.958 and 0.972 accounts for the signal loss introduced by the requirement that a primary vertex must be reconstructed for $\sqrt{s} = 5.02$ and 8 TeV, respectively. It is given by a ratio with **Denominator**: the number of triggered events (after application of the IsIncompleteDAQ cut and the pileup cuts); **Numerator**: the subset of the events in the denominator for which a good vertex was found (i.e., it passes the vertex quality cuts, but without the cut on the z-position of the vertex). Figure 3.18 shows the normalized p_T-spectrum for $K^{*\pm}$ for $\sqrt{s} = 5.02$ and 8 TeV in left and right panels, respectively.

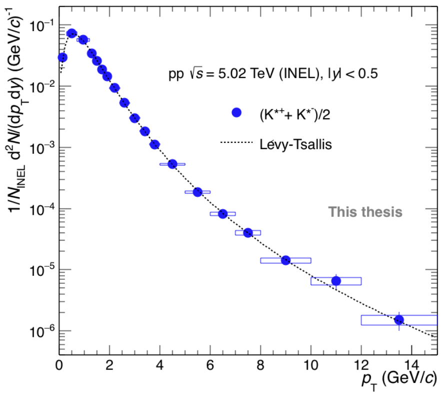

(a) For $\sqrt{s} = 5.02$ TeV.

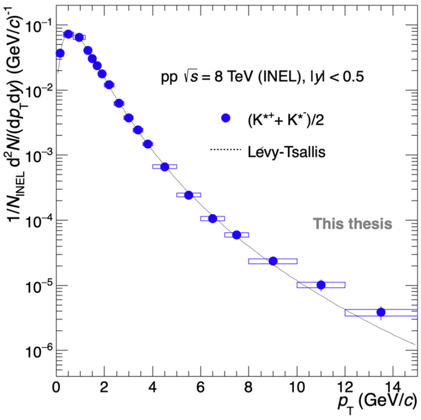

(b) For $\sqrt{s} = 8$ TeV.

Figure 3.18: Inelastic $K^{*\pm}$ spectrum with Lévy-Tsallis fit (black dotted curve), statistical (bars) and systematics (boxes) uncertainties at $\sqrt{s}$ = 5.02 and 8 TeV [107, 108].

3.8 Energy dependence of dN/dy, $\langle p_T \rangle$ and K^*/K

The corrected p_T-spectrum was fitted with a Lévy-Tsallis function, which describes both the exponential and power law shape of the spectrum at low and high transverse momentum, respectively. The Lévy-Tsallis function is defined as

$$\frac{1}{N_{evt}}\frac{d^2N}{dydp_T} = p_T\frac{dN}{dy}\frac{(n-1)(n-2)}{nT[nT+m(n-2)]}(1+\frac{\sqrt{m^2+p_T^2}-m}{nT})^{-n}. \quad (3.20)$$

Here m and p_T denote the mass and transverse momentum of $K^{*\pm}$, respectively. n is a fitting parameter and T is Tsallis temperature. This function describes both the exponential shape of the spectrum at low-p_T and a power-law at high-p_T. The p_T-integrated yield (dN/dy) is obtained by integrating the spectrum in the measured range. Calculated dN/dy and $\langle p_T \rangle$ along with K^*/K ratio for all the available results are given in Table 3.5, and are plotted in Fig 3.19 and Fig 3.20. Both dN/dy and $\langle p_T \rangle$ of $K^{*\pm}$ are observed to increase with collision energy and are consistent with neutral K^* measurement within uncertainties. The K^*/K do not show a strong dependence on the colliding system or the centre of mass system energy, with an exception of the central K^{*0}/K ratio both at RHIC and

LHC energies. The observed suppression of the K^{*0}/K ratio may be the result of rescattering and regeneration effects.

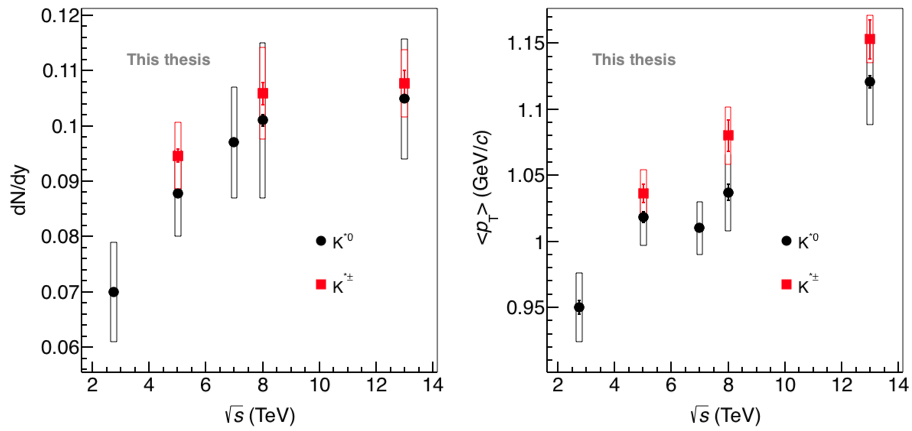

Figure 3.19: (left panel) $K^{*\pm}$ (red symbol) and K^{*0} (black symbol) yield is shown. (right panel) Mean transverse momentum as a function of pp collision energy is shown. K^{*0} results are taken from Ref. [113]. Statistical and systematic uncertainties are shown by error bars and empty boxes, respectively.

Table 3.5: The p_T integrated yield $dN/dy_{|y|<0.5}$, the mean transverse momentum $\langle p_T \rangle$ of $(K^{*+} + K^{*-})/2$ and $K^{*\pm}/K$ for pp collisions at $\sqrt{s} = 5.02$ and 8 TeV are tabulated here. The kaon yield $(K^+ + K^-)/2$ is taken from Ref. [123, 124]. The first error represents the statistical uncertainty and the second one is the systematic uncertainty.

$\sqrt{s}$ (TeV)	dN/dy	$\langle p_T \rangle$ (GeV/c)	$K^{*\pm}/K$
5.02	0.0946 ± 0.0012 ± 0.006	1.036 ± 0.007 ± 0.018	0.353 ± 0.005 ± 0.026
8	0.1058 ± 0.002 ± 0.0083	1.08 ± 0.01 ± 0.02	0.361 ± 0.007 ± 0.032

3.9 Comparison with K^{*0}

The first measurement of $K(892)^{*\pm}$ production in inelastic pp collisions at $\sqrt{s} = 5.02$, 8 and 13 TeV up to $p_T = 15$ GeV/c is reported here. Fig 3.21 shows the $K(892)^{*\pm}$ transverse momentum spectra at these three collision energies. In the same figure the $K(892)^{*0}$ transverse momentum spectra at the same collision energies are reported [125–127]. Considering the similarity of quark content, isospin and mass, the spectra of the charged and

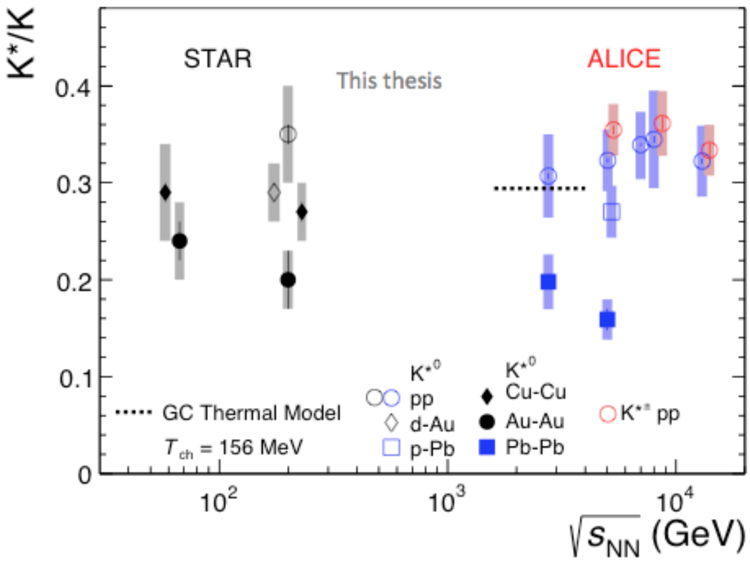

Figure 3.20: Ratios of $K^{*\pm}/K$ and K^{*0}/K in pp, central d–Au and central A+A collisions as a function of $\sqrt{s_{NN}}$ [113]. Error bars represent the statistical uncertainties and boxes represent the systematic uncertainties.

neutral meson are equal within the estimated uncertainties. We observe that, the spectrum is significantly harder at $\sqrt{s}$ = 8 and 13 TeV than at 5.02 TeV.

3.10 Energy dependence p_T-spectra of $K^{*\pm}$

The evolution of the transverse momentum spectra with collision energy is clearly seen in Fig. 3.22, where the ratios of the $K^{*\pm}$ transverse-momentum spectra at $\sqrt{s}$ = 8 and 13 TeV to 5.02 TeV are shown. The systematic uncertainties of the ratios are the quadrature sum of the uncertainties of the two energies. For p_T > 1 GeV/c a clear hardening of the spectra is observed when increasing the collision energy, while at low-p_T the same yield is measured, within the estimated uncertainties. This suggests that particle production mechanism in the soft energy region is independent of the collision energy, while the increase of the slope for p_T > 1 GeV/c suggests an increase of the relevance of the hard scattering processes with the collision energy. Predictions of the same ratios of $K^{*\pm}$ at $\sqrt{s}$ = 8 and 13 TeV to 5.02 TeV from PYTHIA6 - Perugia 2011, PYTHIA8 - Monash

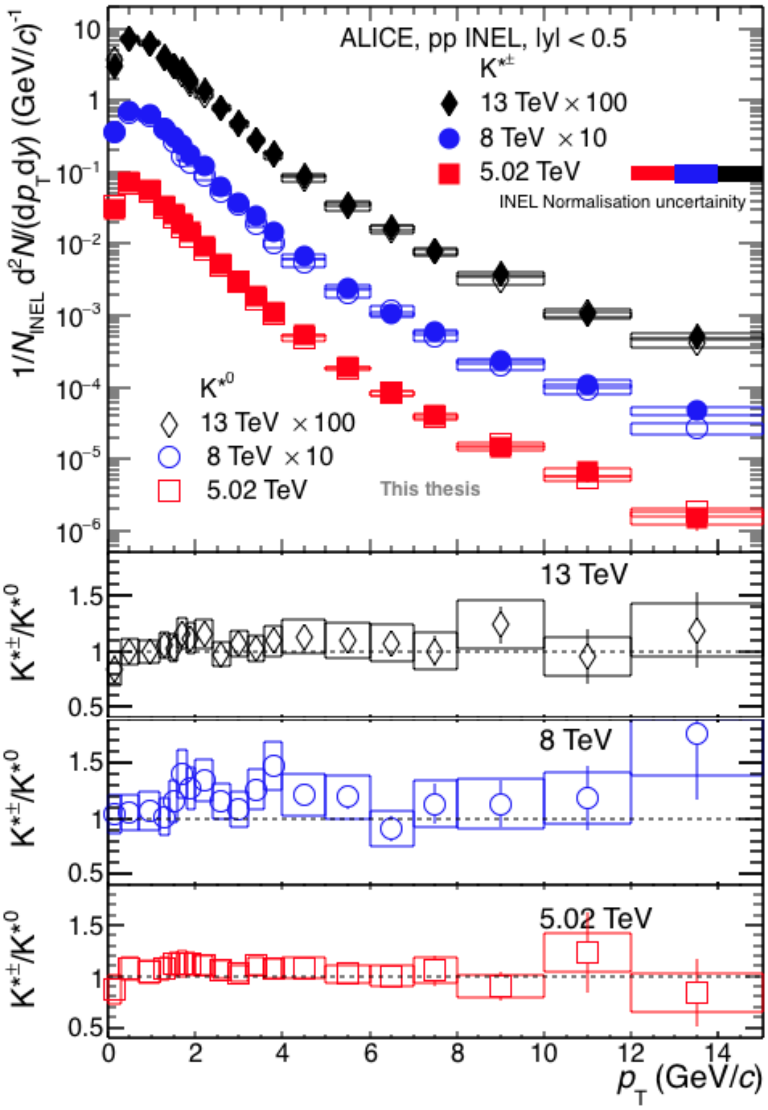

Figure 3.21: Inelastic $K^{*\pm}$ spectrum in solid symbols and K^{*0} spectrum in open symbols for pp collisions at $\sqrt{s}$ = 5.02, 8 and 13 TeV. Statistical and systematic uncertainties are shown by error bars and empty boxes, respectively. The normalization uncertainties are shown as colored boxes and they are not included in the point-to-point uncertainty. In the bottom panels the ratios of the measured p_T-spectra for $K^{*\pm}$ to K^{*0} at $\sqrt{s} = 5.02$ (red open square), 8 (blue open circle) and 13 (black open diamond) TeV are shown [113].

2013 and EPOSLHC are also shown in the figure. This shows that the ratio from EPOSLHC measurement is quiet similar to the ratio obtained from the measured spectra.

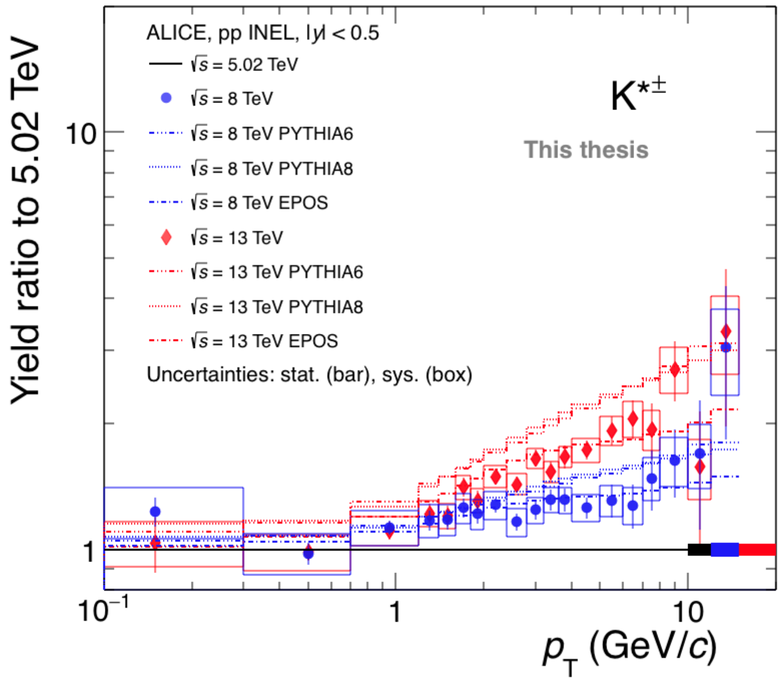

Figure 3.22: Ratios of transverse momentum spectra of $K^{*\pm}$ at $\sqrt{s} = 8$ and 13 TeV to 5.02 TeV. Statistical and systematic uncertainties are shown by error bars and empty boxes, respectively. The normalization uncertainties are shown as colored boxes around 1. Blue and red histograms represent the prediction of the same ratios from PYTHIA6 - Perugia 2011, PYTHIA8 - Monash 2013 and EPOSLHC [113].

3.11 Model comparison

The comparison between the measured p_T-spectra and the calculation of QCD-inspired event generators or microscopic models gives useful information on the hadron production mechanisms. Figs. 3.23 and 3.24 show the comparison of the measured $K^{*\pm}$ spectrum at $\sqrt{s} = 5.02$ and 8 TeV with PYTHIA6 (Perugia 2011 tune), PYTHIA8 (Monash 2013 tune) generators and EPOSLHC.

Modern event generators like PYTHIA combine perturbative picture of hard processes with non-perturbative picture of hadronization which is simulated using the Lund string fragmentation model [128]. In the presented PYTHIA tunes multiple parton-parton interactions in the same event and color reconnection mechanism are taken into account. These effects are important in hadron-hadron interactions at high energies. In particular, the color string formation between final partons may mimic effects similar to that induced by collective flow in heavy-ion collisions [129]. The PYTHIA6 tune Perugia 2011, takes into account first results from the LHC, in particular pp data at 0.9 and 7 TeV, increasing strange baryon production, i.e. a larger Λ/K ratio. Monash 2013 is an updated set of parameters for the PYTHIA8 event generator, with particular attention to heavy-quark fragmentation and strangeness production.

The event generator EPOSLHC differs significantly from PYTHIA in its modeling of hadronization and the underlying events. It is a microscopic model, which relies on parton-based Gribov-Regge theory and incorporates an hydrodynamical evolution if the energy density is high enough. It predicts increased baryon-to-meson ratios at intermediate p_T as a consequence of radial flow. Both PYTHIA8 and EPOSLHC are tuned to reproduce the first multiplicity and identified hadron production in pp collisions at $\sqrt{s} =$ 7 TeV.

From figures 3.23 and 3.24 one can see that an agreement of the models with data increases with the collision energy. The best agreement is reached by PYTHIA6 - Perugia 2011 and PYTHIA8 - Monash 2013 for the 13 TeV collisions [113]. For the three energies all the models overestimate the yield for $p_T < 0.5$ GeV/c, while it is underestimated in the intermediate p_T region. EPOSLHC overestimates the high-p_T region. However, EPOSLHC is able to reproduce well the increase of the yield with the energy, while PYTHIA6 and PYTHIA8 predict a larger hardening with the energy confirmed from Fig. 3.22.

3.12 Summary

In this thesis work, the first measurements for $K^{*\pm}$ resonance obtained in inelastic pp collisions at 5.02 and 8 TeV LHC energies have been presented. They complement and confirm the results at the same collision energies of the K^{*0} meson which differ only for its mass and quark content. The transverse momentum spectra have been measured at mid-rapidity in the range

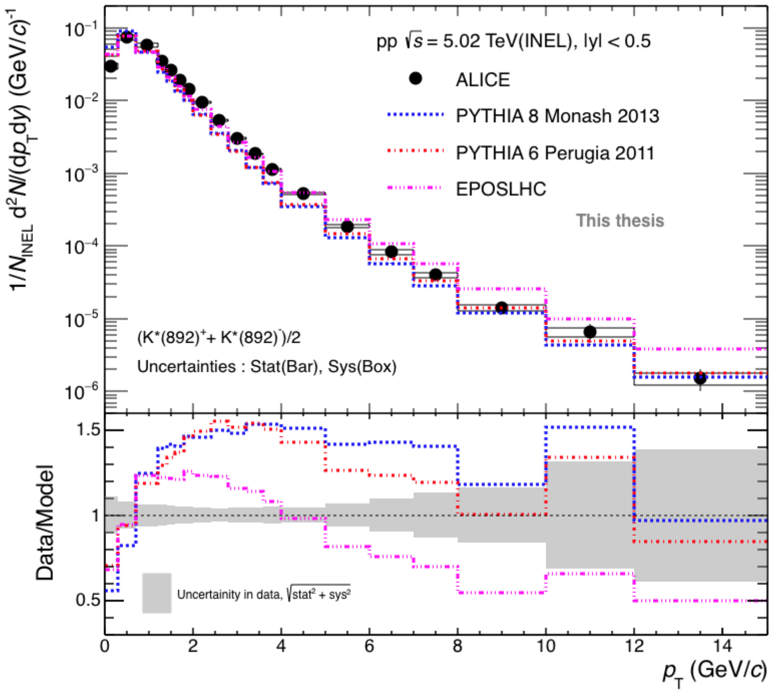

Figure 3.23: Comparison of the measured $K^{*\pm}$ inelastic spectrum shown by black markers in pp collisions at $\sqrt{s}$ = 5.02 TeV to the distributions predicted by PYTHIA8-Monash 2013 (blue lines), PYTHIA6-Perugia 2011 (red lines), and EPOSLHC (magenta lines). (Bottom panel) The ratio of the rebinned predictions to the measured distribution for $K^{*\pm}$ mesons. The shaded band shows the fractional uncertainty of the measured data points [107].

$0 < p_T < 15$ GeV/c and compared with QCD-inspired models (PYTHIA6, PYTHIA8) and hybrid model (EPOSLHC). The agreement of the models with data increases with the collision energy. A better agreement is reached by PYTHIA6 - Perugia 2011 and PYTHIA8 - Monash 2013 for 8 TeV collisions. However EPOSLHC is able to well reproduce the hardening of the p_T-spectrum with the increase of the collision energy. The $K^{*\pm}$ transverse momentum spectrum becomes harder while going from 5.02 TeV to higher collision energy and an increase in the $\langle p_T \rangle$ of about 11% is observed from 5.02 TeV to higher collision energy of 13 TeV. However the K^{*}/K yield ratio do not show a strong dependence on the collision energy. The evolution of the transverse momentum spectra with collision energy is clearly seen considering the ratios of the $K^{*\pm}$ transverse-momentum spectra at $\sqrt{s}$ = 8 and 13 TeV to 5.02 TeV. The observed increase of the slope for $p_T > 1$ GeV/c suggests an increase of the hard scattering processes with

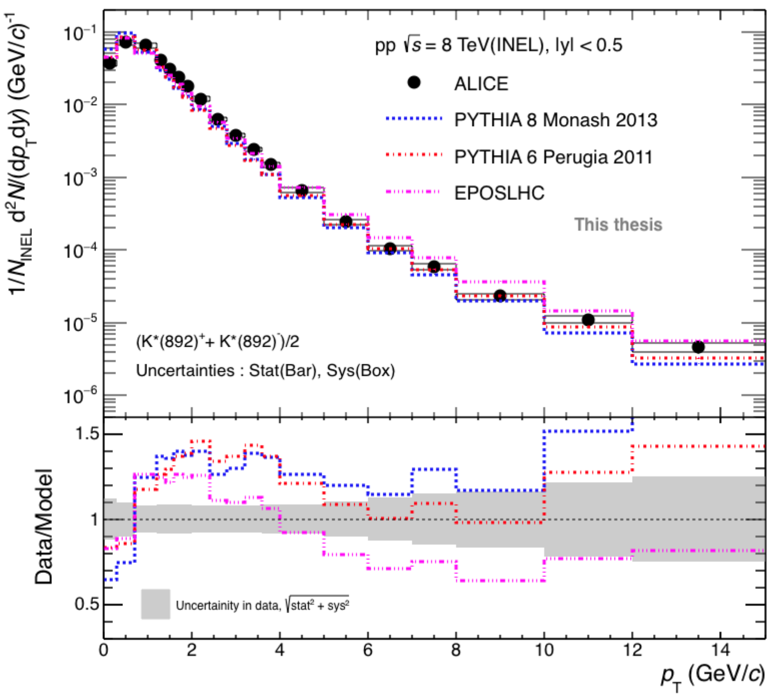

Figure 3.24: Comparison of the measured $K^{*\pm}$ inelastic spectrum shown by black markers in pp collisions at $\sqrt{s} = 8$ TeV to the distributions predicted by PYTHIA8-Monash 2013 (blue lines), PYTHIA6-Perugia 2011 (red lines), and EPOSLHC (magenta lines). (Bottom panel). The ratio of the rebinned predictions to the measured distribution for $K^{*\pm}$ mesons. The shaded band shows the fractional uncertainty of the measured data points [108].

the collision energy. While in the soft region it is found that the particle production mechanism is independent of the collision energy by the same yield value, within the estimated uncertainties.

Chapter 4

Particle production using color string percolation model

"In exclusion, you become trapped. In inclusion, you are liberated".

– Sadhguru

Theoretically, several signatures of first order phase transition and the critical point in QCD phase diagram have been proposed [52, 130, 131]. A non-monotonic variation of conserved quantum number fluctuations as a function of $\sqrt{s_{\rm NN}}$ is found near the expected critical point [132]. Transport properties of strongly interacting matter, such as shear and bulk viscosities are of particular importance to understand the nature of QCD matter. It is expected that the ratio of shear viscosity (η) to entropy density (s) would exhibit a minimum value near the QCD critical point [133]. The Beam Energy Scan (BES) program at RHIC is dedicated to locate the QCD critical point. In BES program, RHIC has collided heavy-ion (Au+Au) beams at $\sqrt{s_{\rm NN}}$ = 7.7 - 200 GeV. Recently, the STAR experiment has reported some interesting features regarding search for critical point around $\sqrt{s_{\rm NN}}$ = 19.6 GeV [132]. The higher moments of net-proton distribution show significant deviation from Poissonian expectation and Hadron Resonance Gas model prediction at $\sqrt{s_{\rm NN}}$ = 19.6 and 27 GeV [132]. Also, the two particle transverse momentum (p_T) correlation scaled with average transverse momentum ($\langle p_T \rangle$) fluctuation, which is related to the specific heat, C_V of the system, significantly decreases below $\sqrt{s_{\rm NN}}$ = 19.6 GeV [134]. Electrical conductivity ($\sigma_{\rm el}$) is another key transport coefficient in order to understand the behaviour and properties of strongly interacting matter. This plays an important role in the hydrodynamic evolution of the matter produced in heavy-ion collisions where charge relaxation takes place. In Ref. [135], the electrical conductivity is extracted from charge dependent flow parameters from asymmetric heavy-ion collisions. Experimentally, it has been observed that very strong electric and magnetic fields are created in the early stages (1-2 fm/c) of non-central collisions of nuclei at RHIC and LHC [135, 136]. The values of the electric and magnetic fields at RHIC are eE $\approx m_{\pi}^{2} \approx 10^{21}$ V/cm and eB $\approx m_{\pi}^{2} \approx 10^{18}$ G [136]. Such a large electrical field influences the medium, which depends on the electrical conductivity. $\sigma_{\rm el}$ is responsible for producing an electric current in the early stage of the heavy-ion collision. Therefore, it would be very interesting to study the thermodynamical quantities and transport properties of the QCD matter with special emphasis on RHIC BES energies.

This chapter is organised as follows. In section 4.1, an overview of percolation theory and its applicability in strongly interacting matter is discussed. In section 4.2, the dynamics of string interactions is introduced. Section 4.3 covers the formalism and methodology of color string percolation model (CSPM). Section 4.4 covers a study of the initial temperatures at RHIC energies as obtained using CSPM and a comparison with various chemical freeze-out results. In addition, the thermodynamical and transport quantities like energy density, shear viscosity, trace anomaly, speed of sound, entropy density, bulk viscosity, electrical conductivity of the matter produced in heavy-ion collision at RHIC by using the CSPM are discussed. The next section 4.5 is dedicated to the energy and centrality dependence study in CSPM. Finally, the findings of the work are summarized in section 4.6.

4.1 Percolation in strongly interacting matter

It is suggested that, the possible transition of strongly interacting matter from a hadron gas to a phase of quarks and gluons can be treated by percolation theory [137]. The percolation approach can provide both a qualitative picture of the transitions in strongly interacting matter and also reasonable quantitative values for the transition densities [138]. Hadrons are extended objects built-up of confined quark constituents. The interaction between quarks provide the scale for both the size of hadrons and for the range of nuclear (hadronic) forces. For example, lets assume quarks inside a hadron (eg. pion) are confined in an infinite square-well potential of radius R_Q. The radius of a hadron as seen in a scattering experiment is $2R_Q$. The quarks from each of the collision partners can interact with each other if the separation distance is, $r \leq 2R_Q$. This can be confirmed from the left panel of Fig. 4.1. The volume of a hadron is given by $V_H = 8V_Q$, where $V_Q = 4\pi R_Q^3/3$, which is called the size of the confinement sphere or hadronic "core". Now the matter produced from the interaction can be distinguished according to different density regions. The density of a many hadronic system is defined as, $\rho \sim N/V$, where N is the fractional volume occupied by the hadrons and V is the total volume. At equilibrium a free gas of hadrons, which is called "Hadron gas" is expected with no overlap of hadronic volumes. And as the density becomes high enough interactions happen between hadrons and it is called "Hadronic matter". In the hadronic matter state, as illustrated in the middle panel of the Fig 4.1, a multi-hadron system is formed. In the multi-hadron system, the quarks involved are still associated to a given hadron i.e there is no overlap in the "core" region. When the hadronic cores interconnected with overlapping of the cores the quarks are no longer connect to specific hadrons, this state is called "Quark matter" and is shown in the right panel of the Fig 4.1.

Now the question comes "What is percolation theory?" and its justification for the study of strongly interacting matter. To understand this let's

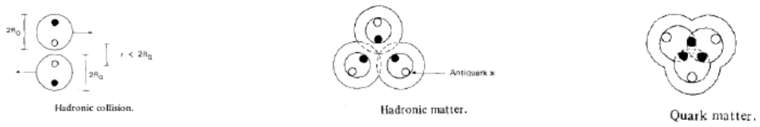

Figure 4.1: Different regimes of nuclear matter density [138].

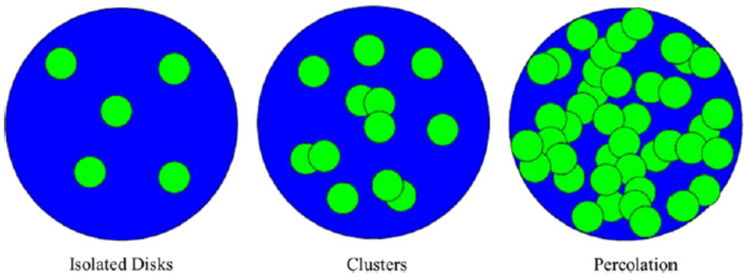

Figure 4.2: Left panel: Disconnected discs, Middle: Cluster formation, Right panel: Overlapping discs forming a cluster of communication [53].

take one example. Let us distribute small discs randomly on a large surface, allowing them to overlap. As the number of discs increases clusters of overlapping discs start to form. If we consider the discs as small water droplets, then how many drops are needed to form a puddle crossing the considered surface. So numerical studies indicate that this "percolation" will occur when 34% of the total space is covered by sum of the spaces of drops [138]. A schematic diagram is shown in Fig. 4.2 for understanding. So, if we place overlapping spheres in a large volume, the critical density for the percolating spheres is,

$$\rho_H = 0.34/V_H. \tag{4.1}$$

With an hadronic radius ($R_H = 2R_Q(R_Q$= radius of infinite square-well potential)) of 1 fm, one expects hadronic matter formation at densities,

$$\rho \geq \rho_H = 0.48\rho_0 \tag{4.2}$$

Here, $\rho_0 = 0.17$ GeV/fm^{-3} is the normal nuclear density. Similarly, core percolation starts at

$$\rho_Q = 0.34/V_Q. \tag{4.3}$$

so we expect quark matter formation for densities,

$$\rho \geq \rho_Q = 3.84\rho_0. \tag{4.4}$$

As quarks are confined inside hadrons, like protons and neutrons for example, taking proton charge radius to be 0.84 fm, the matter density of proton comes around 0.5 GeV/fm^3 which is almost 3-times the normal nuclear matter density. This goes inline with the expectations of the percolation theory for the density requirement for the formation of a quark matter. It appears physically reasonable that in both cases there will be a coexistence regime beyond the percolation point. So, for $\rho < \rho_H$ only hadron gas exist but slightly above $\rho \geq \rho_H$ coexistence of hadronic matter and hadron gas happens. Similarly just above $\rho \geq \rho_Q$ coexistence of hadronic matter and quark matter happen. There is a critical density for the phase transition of hadron gas to hadronic matter just above the ρ_H and similarly a critical density for the phase transition of hadronic matter to quark matter is just above ρ_Q, where the quarks can move freely beyond the hadronic dimensions [138].

A three-dimensional percolation has been applied to study the phase boundaries of high density matter. Above a certain high density, hadrons lose their identity. By raising either the temperature or the baryon density, quarks of a given hadron will be closer to some quarks (antiquarks) of other hadrons than their original partners in configuration space giving rise to a de-confined quark (antiquark) matter. At $\mu = 0$, the percolating density for mesons and low density baryons is, $\rho_c \sim 0.6\ fm^{-3}$ [53]. This is the critical density of the percolating clusters at the onset of the de-confinement transition. The percolation of color strings is an approach to investigate the formation of a strongly interaction matter. In the next section, the details of the color string interactions and dynamics is described.

4.2 String interactions and dynamics

From theoretical point of view, in addition to hydrodynamic studies, Color Glass Condensate (CGC), which is derived directly from QCD, gives reasonable description of several experimental observables [139]. An alternative approach to the CGC is the percolation of color strings [53]. It is a QCD inspired model but is not directly obtained from QCD. In CSPM, the color flux tubes are stretched between the colliding partons in terms of the color field. A schematic diagram is shown in Fig. 4.3. The strings produce $q\bar{q}$ pairs in finite space filled with the chromoelectric field similar to the Schwinger mechanism of pair creation in a constant electric field covering all the space [53]. A schematic diagram showing the production of new hadrons from breaking of the color strings are shown in Fig. 4.4. The number of strings grow with the energy and with the number of nucleons of participating nuclei. The color strings may be viewed as small discs in the transverse space filled with the color field created by colliding partons. With growing energy and size of the colliding nuclei the number of strings grow and start to overlap, and interact to form clusters in the transverse plane, similar to disks in two dimensional (2D) percolation theory [141].

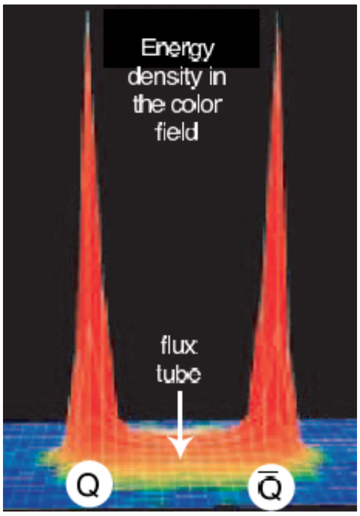

Figure 4.3: Color flux tube between projectile and target [140].

At a critical string density, a macroscopic cluster appears that marks the percolation phase transition which spans the transverse nuclear inter-

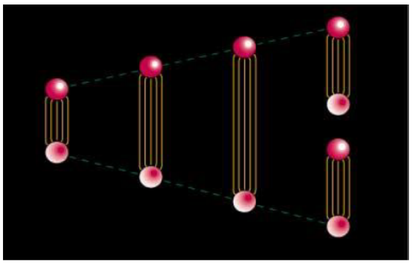

Figure 4.4: Production of new hadrons from color strings [140].

action area. The general result, due to the SU(3) random summation of charges, is a reduction in multiplicity and an increase in the string tension, hence increase in the average transverse momentum squared, $\langle p_T^2 \rangle$ [53].

However in CSPM, the Schwinger barrier penetration mechanism for particle production, the fluctuations in the associated string tension and taking into account the quantum fluctuations of the color field make it possible to define a temperature. Consequently, the particle spectrum is “born” with a thermal distribution. When the initial density of interacting colored strings (ξ) exceed the 2D percolation threshold (ξ_c) i.e. $\xi > \xi_c$, a macroscopic cluster appears, which defines the onset of color de-confinement. This happens at $\xi_c \geq 1.2$ [141, 142]. The critical density of percolation is related to the effective critical temperature and thus percolation may be the way to achieve de-confinement in the heavy-ion collisions [143]. It is observed that, CSPM can be successfully used to describe the initial stages in high energy heavy-ion collisions [53]. In our work [144], the thermodynamical variables and transport coefficients are obtained using CSPM. The results are compared with lQCD predictions [145]. CSPM has been successfully applied to small systems as well. It has been shown that de-confinement can be achieved in high multiplicity events $\bar{\mathrm{p}}\mathrm{p}$ collisions at $\sqrt{s} = 1.8$ TeV in E-735 experiment [146]. Thus CSPM is a new paradigm which has been successful in explaining the initial thermalization both in A + A and in high multiplicity $\bar{\mathrm{p}}\mathrm{p}$ collisions at $\sqrt{s} = 1.8$ TeV.

4.3 Formulation and methodology

In CSPM, the interactions of strings or in other words the overlapping of strings reduce the hadron multiplicity (μ) and increases the average transverse momentum squared, $\langle p_T^2 \rangle$ of these hadrons to conserve the total transverse momentum. The hadron multiplicity and $\langle p_T^2 \rangle$ are directly related to the field strength of the color sources and thus to the generating color. For a cluster of n individual strings, we have [147],

$$n = \frac{\mu}{\mu_0} \frac{\langle p_T^2 \rangle}{\langle p_T^2 \rangle_1}, \tag{4.5}$$

where μ_0 and $\langle p_T^2 \rangle_1$ are the multiplicity and the mean transverse momentum squared of particles produced from a single string [147], respectively. As the number of strings, n increases the macroscopic cluster suddenly spans the area. In 2D percolation theory, the dimensionless percolation density parameter is given by [51, 148]

$$\xi = \frac{N_S S_1}{S_n}, \tag{4.6}$$

where N_S and S_n being the total number of individual strings and interaction area, respectively. S_1 is the transverse area of a single string. We evaluate the initial value of ξ by fitting the experimental data of p_T spectra in pp collisions at $\sqrt{s} = 200$ GeV using the following function:

$$\frac{dN_{ch}}{dp_T^2} = \frac{a}{(p_0 + p_T)^\alpha}, \tag{4.7}$$

where, a is the normalisation factor and p_0, α are fitting parameters given as, $p_0 = 1.982$ and $\alpha = 12.877$ [53]. In order to evaluate the interactions of strings in A+A collisions, we use the above parameterisation as follows,

$$p_0 \to p_0 \left(\frac{\langle nS_1/S_n \rangle_{Au+Au}}{\langle nS_1/S_n \rangle_{pp}} \right)^{1/4}. \tag{4.8}$$

Here, S_n corresponds to the area occupied by the n overlapping strings. Using thermodynamic limit, *i.e.* n and $S_n \to \infty$ and keeping ξ fixed, we get

$$\langle \frac{nS_1}{S_n} \rangle = \frac{1}{F^2(\xi)}, \tag{4.9}$$

where, $F(\xi)$ is the color suppression factor which reduces the hadron multiplicity from $n\mu_0$ to the interacting string value, μ as

$$\mu = F(\xi)n\mu_0, \tag{4.10}$$

where,

$$F(\xi) = \sqrt{\frac{1 - e^{-\xi}}{\xi}}. \tag{4.11}$$

Using Eq. 4.8, we calculate for A + A collisions as,

$$\frac{dN_{ch}}{dp_T^2} = \frac{a}{(p_0\sqrt{F(\xi)_{pp}/F(\xi)_{Au+Au}} + p_T)^\alpha}. \tag{4.12}$$

Here, $\langle p_T^2 \rangle_n = \langle p_T^2 \rangle_1/\mathrm{F}(\xi)$. μ is the multiplicity and $\langle p_T^2 \rangle_n$ is the mean transverse momentum squared of the particles produced by a cluster of n strings. In pp collisions, $\langle nS_1/S_n \rangle \sim 1$ due to the low string overlap probability. The measured values of ξ for different RHIC energies are tabulated in Table 4.1. The initial temperature of the percolation cluster, $T(\xi)$ can be represented in terms of $\mathrm{F}(\xi)$ as [53],

$$T(\xi) = \sqrt{\frac{\langle p_T^2 \rangle_1}{2F(\xi)}}. \tag{4.13}$$

Recently, it has been suggested that fast thermalization in heavy-ion collisions can occur through the existence of an event horizon caused by a rapid de-acceleration of the colliding nuclei [149]. The thermalization in this case is due to the Hawking-Unruh effect [150, 151]. In CSPM the strong color field inside the large cluster produces de-acceleration of the primary $q\bar{q}$ pair which can be seen as a thermal temperature by means of the Hawking-Unruh effect.

Table 4.1: The thermodynamical observables and transport coefficients estimated in CSPM for $(0-10)\%$ central Au+Au collisions at various RHIC energies.

$\sqrt{s_{\rm NN}}$ (GeV)	ξ	$F(\xi)$	ε/T^4	c_s^2	s/T^3	η/s	ζ/s	Δ	T (MeV)
7.7	0.75 ± 0.09	0.84 ± 0.03	6.90 ± 1.16	0.09 ± 0.04	7.56 ± 1.30	0.31 ± 0.03	0.26 ± 0.09	3.25 ± 0.30	159.96 ± 3.82
11.5	0.99 ± 0.13	0.80 ± 0.03	8.24 ± 1.42	0.12 ± 0.04	9.23 ± 1.63	0.26 ± 0.02	0.18 ± 0.07	3.78 ± 0.31	164.16 ± 4.05
19.6	1.39 ± 0.05	0.740 ± 0.006	9.85 ± 0.85	0.160 ± 0.009	11.41 ± 0.99	0.230 ± 0.005	0.106 ± 0.011	4.34± 0.10	170.83 ± 2.82
27	1.47 ± 0.03	0.724 ± 0.003	10.10 ± 0.80	0.165 ± 0.005	11.77 ± 0.94	0.227 ± 0.004	0.097 ± 0.005	4.41 ± 0.08	172.15 ± 2.76
39	1.81± 0.05	0.679 ± 0.006	10.95 ± 0.92	0.190 ± 0.006	13.04 ± 1.10	0.215 ± 0.004	0.066 ± 0.006	4.64 ± 0.09	177.72 ± 2.95
62.4	1.89 ± 0.09	0.67 ± 0.01	11.14 ± 1.07	0.19 ± 0.01	13.32 ± 1.28	0.213 ± 0.005	0.06 ± 0.01	4.68 ± 0.11	178.89 ± 3.14
130	2.59 ± 0.04	0.597 ± 0.004	12.10 ± 0.97	0.234 ± 0.003	14.94 ± 1.19	0.207 ± 0.003	0.030 ± 0.001	4.81 ± 0.08	189.59 ± 3.07
200	2.65 ± 0.14	0.59 ± 0.01	12.19 ± 1.23	0.24 ± 0.01	15.08 ± 1.53	0.207 ± 0.004	0.028 ± 0.006	4.82 ± 0.10	190.32 ± 3.50

The single string average transverse momentum, $\langle p_T^2\rangle_1$ is calculated using eq. (4.13) at critical temperature, $\rm T_c$ = 167.7 ± 2.76 MeV [152] and $\xi_c \sim 1.2$. We get $\sqrt{\langle p_T^2\rangle_1}$ = 207.2±3.3 MeV [53], which is $\simeq$ 200 MeV, obtained in the previous calculation using percolation model [143]. The initial temperatures (T) for different energies corresponding to their ξ values are also tabulated in Table 4.1. Figure 4.5 shows the percolation density parameter ξ as a function of beam energy. It is observed that ξ is a linear function of $\sqrt{s_{\rm NN}}$. The horizontal line in Fig. 4.5 at ξ_c = 1.2 is the percolation threshold at which the spanning cluster appears, a connected system of color sources and identifies the percolation phase transition [141, 142]. It is observed that this threshold is achieved for $\sqrt{s_{\rm NN}}$ = 19.6 GeV and above.

4.4 Thermodynamic and transport properties

In this work [144], we attempt to determine the thermodynamic and transport properties of the strongly interacting matter produced in the central Au+Au collisions at various RHIC energies ranging from 7.7 to 200 GeV using CSPM. We study the thermodynamical properties such as, energy

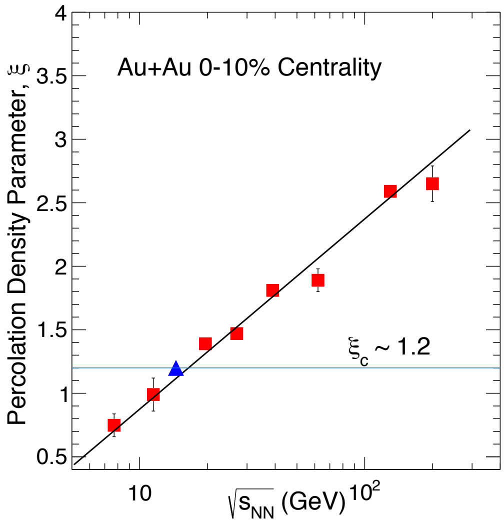

Figure 4.5: (Color online) Percolation density parameter, ξ as a function of $\sqrt{s_{\rm NN}}$. The red squares show the values for RHIC energies from $\sqrt{s_{\rm NN}}$ = 7.7 - 200 GeV [144]. The blue triangle is the prediction for 14.5 GeV. The horizontal line at $\xi \sim 1.2$ is the critical value of ξ [141, 142].

density, speed of sound, entropy density and transport properties like electrical conductivity, shear and bulk viscosities etc. These observables are discussed in details in the following sections.

4.4.1 Chemical freeze-out and initial temperature

The predictions of chemical freeze-out temperature (T_{ch}), and baryon chemical potential (μ_B) obtained at various energies of RHIC experiment are shown in Fig. 4.6. The blue dash-dotted line represents the lQCD calculations of the chiral curvature in terms of T and μ_B [153]. The co-ordinates of hadronization points estimated by using a transport model fit to the experimental data at SPS energies are shown by green triangles [154]. The blue circles are the experimentally measured values of (T_{ch}, μ_B) by the STAR experiment [155], which uses a statistical thermal model fit to the experimental particle ratios. The initial temperatures obtained in CSPM at RHIC energies are presented by red squares and it is found that as we go from lower energies to higher energies, the differences between initial temperatures and chemical freeze-out temperatures increases. The initial energy density created in heavy-ion collisions govern the subsequent hadronization and system evolution to the final state, characterized by the system freeze-out. The large difference in the initial temperature at higher energies, as obtained in the framework of CSPM and the chemical freeze-out temperatures obtained in the framework of statistical hadron gas models using experimental particle ratios are simply because of the higher initial energy densities (temperatures) at lower baryochemical potentials. The values of T_{ch} obtained by STAR experiment lie below the lQCD results except at vanishing baryon chemical potential.

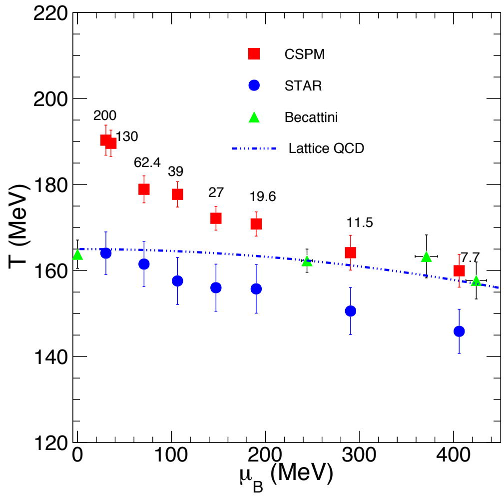

Figure 4.6: (Color online) The temperature and baryon chemical potential (μ_B) estimated in different calculations at various center-of-mass energies [144]. The red squares are the initial temperatures at RHIC energies estimated in CSPM. The blue dash-dotted line is the prediction from lQCD [153]. The green triangles are for hadronization temperature and baryon chemical potential as obtained in the statistical model [154]. The blue circles are (T, μ_B) at freeze-out estimated by STAR experiment [155].

4.4.2 Initial energy density

CSPM assumes that the initial temperature of the fluid in local thermal equilibrium is determined at the string level. So, CSPM along with boost invariant Bjorken hydrodynamics [156] is used to calculate energy density, pressure, entropy etc. The expression for initial energy density (ε) is given as,

$$\varepsilon = \frac{3}{2}\frac{\frac{dN_{ch}}{dy}\langle m_T \rangle}{S_N \tau_{pro}}, \tag{4.14}$$

where, S_N is the nuclear overlap area estimated by using Glauber model [157] and τ_{pro} is the production time for a boson (gluon). Here, $m_T = \sqrt{m^2 + p_T^2}$ is the transverse mass. For evaluating ε, we use the charged pion multiplicity dN_{ch}/dy at midrapidity and S_N values from STAR for $0\% - 10\%$ central Au+Au collisions at $\sqrt{s_{\rm NN}}$ = 7.7 - 200 GeV [157, 158]. The dynamics of massless particle production has been studied in two-dimensional Quantum Electrodynamics (QED_2). QED_2 can be scaled from electrodynamics to quantum chromodynamics using the ratio of the coupling constants [159]. The production time (τ_{pro}) for the boson (gluon) is [160],

$$\tau_{pro} = \frac{2.405\hbar}{\langle m_T \rangle}. \tag{4.15}$$

Figure 4.7 shows the variation of the energy density with ξ. Solid circles

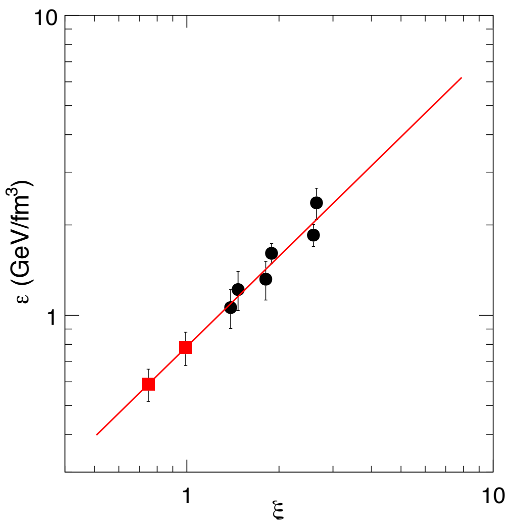

Figure 4.7: (Color online) Initial energy Density ε as a function of the percolation density parameter, ξ [144]. The black circles show the values for RHIC energies from $\sqrt{s_{\rm NN}}$ = 19.6 - 200 GeV. The red squares are the interpolated ξ values for 7.7 and 11.5 GeV.

are the results obtained using CSPM at RHIC energies starting from $\sqrt{s_{\rm NN}}$

= 19.6 - 200 GeV. Line represents fitting of CSPM results. Here, we do not consider the results at $\sqrt{s_{\mathrm{NN}}}$ = 7.7, and 11.5 GeV as they behave differently in comparison to the other RHIC energies due to the excess presence of baryons. It is found that ε is proportional to ξ. The parameterisation of the CSPM results gives, $\varepsilon = 0.786\ \xi$ (GeV/fm^3). We extrapolate this relationship to estimate ξ values for $\sqrt{s_{\mathrm{NN}}}$ = 7.7, and 11.5 GeV. We use this relationship to calculate various thermodynamical and transport properties. Figure 4.8 presents the variation of ϵ/T^4, which is proportional to

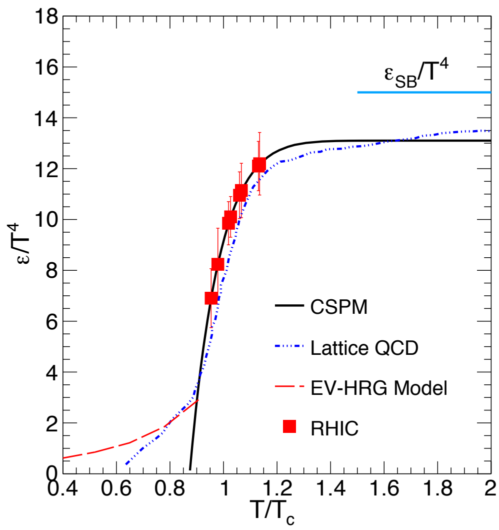

Figure 4.8: (Color online) Scaled energy density (ε/T^4) as a function of T/T_c [144]. The black solid line is CSPM results and the blue dash-dotted line corresponds to the lattice QCD results [145]. The red dashed line shows the result from EV-HRG model [161].

degrees of freedom of the system with scaled temperature (T/T_c), where T_c is the critical temperature. The square symbols are the results calculated from CSPM at various RHIC energies starting from 7.7 - 200 GeV. The lattice QCD results from HotQCD collaboration [145] are also shown by the blue dash-dotted line. The solid line is the CSPM results calculated using our parameterisation. The red dashed line shows the result for hadron gas calculated using Excluded-Volume Hadron Resonance Gas (EV-HRG) model [161] at $\mu_B = 0$, which matches with the lQCD results at lower temperature. We find that ε/T^4 varies rapidly around $T/T_c \sim 1$, which suggests that the number of degrees of freedom change rapidly at this temperature and there is a cross-over phase transition from hadron gas to quark-gluon plasma. After $T/T_c \sim 1.2$, we observe that ε/T^4 saturates with temperature. It is observed that CSPM results are in good agreement with the lattice QCD results [145] and always lie below to the value of the ideal gas Stefan-Boltzmann limit.

4.4.3 Shear viscosity

The observation of the large elliptic flow at RHIC in non-central heavy-ion collisions suggests that the matter created is a nearly perfect fluid with very low shear viscosity [57, 162–164]. Shear viscosity to entropy density ratio (η/s) as a measure of the fluidity is used as one of the important observables to understand the QCD medium. η/s shows minimum at the critical point for various substances for example helium, nitrogen and water [165]. Thus the measurement of η/s can provide the required information to locate the critical end point/crossover region in the QCD phase diagram. In the framework of a relativistic kinetic theory, the shear viscosity over entropy density ratio, η/s is given by [166–168],

$$\eta/s \simeq \frac{T\lambda_{mfp}}{5}, \tag{4.16}$$

where, T is temperature, λ_{mfp} is the mean free path calculated by using the following formula,

$$\lambda_{mfp} = \frac{L}{(1-e^{-\xi})}. \tag{4.17}$$

L is the longitudinal extension of the string ~ 1 fm. Now Eq.4.16 becomes,

$$\eta/s \simeq \frac{TL}{5(1-e^{-\xi})}. \tag{4.18}$$

Figure 4.9(b) shows η/s as a function of T/T_c. The CSPM results are shown along with the results for weakly interacting QGP (wQGP) [168] and strongly interacting QGP (sQGP) [168]. The lower bound of this ratio *i. e.* $1/4\pi$ proposed by AdS/CFT calculations [169] is also shown

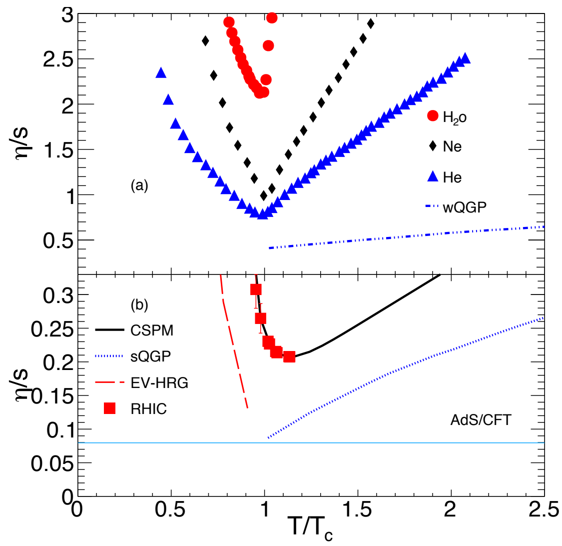

Figure 4.9: (Color online) η/s as a function of T/T_c. The red square shows the results from various RHIC energies from the CSPM [144]. The black solid line shows the extrapolation to higher temperatures from CSPM. The solid horizontal line around $1/4\pi$ represents the AdS/CFT limit [169]. Blue dash-dotted and blue dotted line show the results from wQGP and sQGP, respectively [168]. The red dashed line shows the calculations of EV-HRG [161].

in Fig.4.9(b). It is observed that the matter produced in such collisions has the smallest η/s value among any known fluids which supports the finding of the formation of perfect fluid at RHIC. For comparison purpose η/s values for various atomic fluids are shown in Fig. 4.9(a) [165]. The measured values of η/s are tabulated in the Table 4.1.

4.4.4 Trace anomaly

Trace anomaly ($\Delta = (\varepsilon - 3P)/T^4$) measures the deviation from the conformal behaviour, which is the trace of energy-momentum tensor, $\langle \Theta^{\mu}_{\mu} \rangle = (\varepsilon - 3p)$. This also helps in identifying the existence of interactions in the medium [170]. The reciprocal of η/s is in quantitative agreement with Δ for a wide range of temperatures. So, the minimum of η/s corresponds to the maximum of Δ. Figure 4.26 shows the variations of Δ with the temperature. We show the calculations of CSPM along with the results of lQCD from HotQCD collaboration [171] and Wuppertal collaboration [172]. We find that CSPM results are in close agreement with that of the HotQCD collaboration results while lie above to that of Wuppertal collaboration. The value of Δ is found to be maximum at top RHIC energy where η/s shows minimum in CSPM calculations [53].

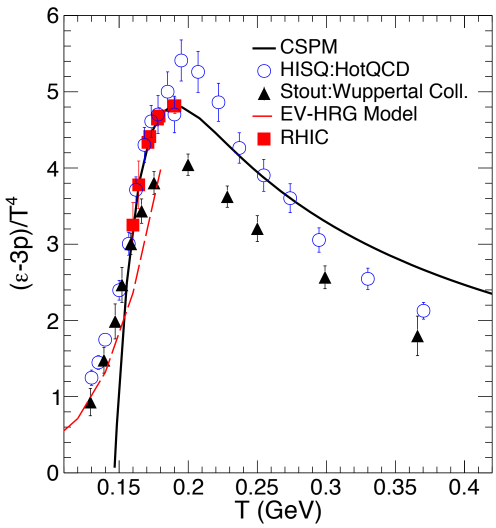

Figure 4.10: (Color online) Variation of trace anomaly $\Delta = (\varepsilon - 3P)/T^4$ with respect to temperature [144]. Blue circles represent results from HotQCD collaboration [171]. Black triangle refer to Wuppertal collaboration [172]. The red dashed line shows the result from EV-HRG model [161]. The red squares are the results obtained from CSPM for RHIC energies and black line is the extrapolated CSPM results.

4.4.5 Speed of sound

The speed of sound is an important quantity which is related with the small perturbations produced in the medium formed in heavy-ion collisions. It explains how the change in the energy density profile of the created medium is converted into pressure gradients. In hydrodynamics, the collective expansion is observed due to pressure gradients. Using the boost-invariant Bjorken 1D hydrodynamics [156] with CSPM, the square of speed of sound (C_s^2) is calculated as [53],

$$\begin{aligned} C_s^2 &= (-0.33)\left(\frac{\xi e^{-\xi}}{1-e^{-\xi}} - 1\right) \\ &+ \ 0.0191(\Delta/3)\left(\frac{\xi e^{-\xi}}{(1-e^{-\xi})^2} - \frac{1}{1-e^{-\xi}}\right), \end{aligned} \tag{4.19}$$

where $\Delta = (\varepsilon - 3P)/T^4$ is the trace anomaly. In Fig. 4.11, we show the variations of C_s^2 with T/T_c. The solid line represents the result obtained in CSPM while the blue dash-dotted line is the lattice QCD results at zero chemical potential [145]. There is a very good agreement between these two, particularly at higher T/T_c where the deviation is observed in an earlier work [147]. At $\mathrm{T/T_c} = 1$, CSPM and lQCD results agree with the EV-HRG results shown by the red dashed line. The red squares are the results at RHIC energies. CSPM results always lie below the limiting value of C_s^2 for ideal gas which is 1/3 at all the temperatures. These findings are expected in the case of interacting matter and suggest that the causality is respected.

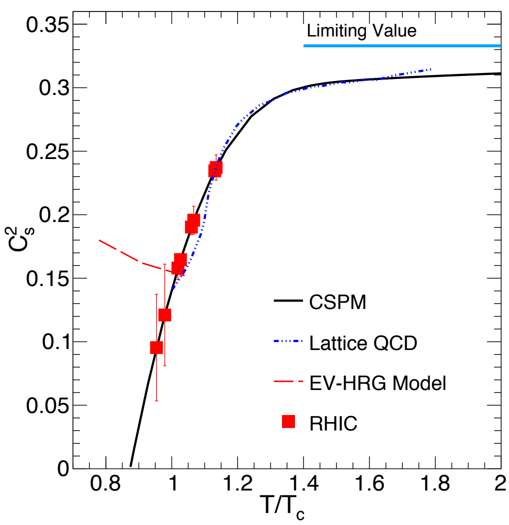

Figure 4.11: (Color online) The squared speed of sound (C_s^2) as a function of $\mathrm{T/T_c}$ [144]. The red squares are the CSPM results at RHIC energies. The black line is the extrapolated CSPM result. Blue dash-dotted line represents lQCD results [145]. The red dashed line shows the result from EV-HRG [161].

4.4.6 Entropy density

We estimate the entropy density (s) using CSPM coupled to the hydrodynamics. In CSPM, the strings interact strongly to form clusters and produce pressure and energy density at the early stages of the collisions.

The expression for entropy density is,

$$s = (1 + C_s^2)\frac{\varepsilon}{T}. \tag{4.20}$$

Figure 4.12 shows the variations of scaled entropy density (s/T^3) with $\mathrm{T/T_c}$. The solid line is the CSPM results using our parameterisation. The red squares show the results for RHIC energies. The red dashed line shows the result from EV-HRG model for a hadron gas. The solid blue line is the s/T^3 in the Stefan-Boltzmann limit. Again, we find a good agreement between CSPM results and lQCD data [145] shown by the blue dash-dotted line. We find that s/T^3 changes rapidly with temperature. The rise of entropy density close to the phase transition temperature region, determined by the fluctuations of the chiral order parameter, is a consequence of the production of many new quark degrees of freedom [173].

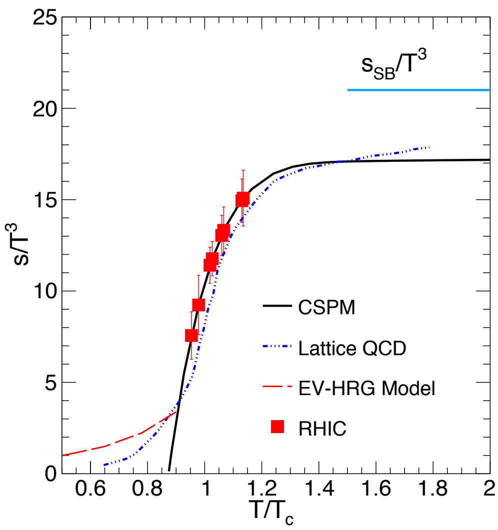

Figure 4.12: (Color online) Entropy density (s/T^3) as a function of $\mathrm{T/T_c}$ [144]. The red squares are the results from CSPM for RHIC energies. Blue dash-dotted line represents the lQCD results [145]. The red dashed line shows the result calculated using EV-HRG model [161].

4.4.7 Bulk viscosity

In the perfect fluid limit the energy density decreases with proper time due to longitudinal expansion. However, the viscosity opposes the system to perform the useful work while expanding longitudinally. In order to quantify the location of the critical point, it is very important to study the bulk viscosity to entropy density ratio (ζ/s) which changes rapidly at this point. The ζ/s is calculated through the relation of shear viscosity and speed of sound given as follows [174],

$$\frac{\zeta}{s} = 15\frac{\eta}{s}(\frac{1}{3} - C_s^2)^2. \tag{4.21}$$

In Fig.4.13, we show the variation of ζ/s with the temperature. We compare CSPM results with the lQCD calculations [175] and again find a good agreement between these two. We observe that ζ/s is small compared to η/s for $\mathrm{T/T_c} > 1$.

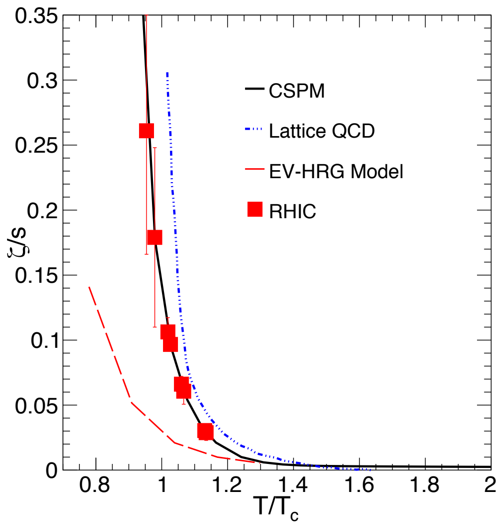

Figure 4.13: (Color online) The ratio of bulk viscosity and entropy density (ζ/s) as a function of $\mathrm{T/T_c}$ is shown by red squares from CSPM [144] and the black solid line shows the extrapolated CSPM results. The blue dash-dotted line corresponds to results from lQCD [175]. The red dashed line is the result of EV-HRG model [161].

4.4.8 Electrical conductivity

Electrical conductivity ($\sigma_{\rm el}$) is another key transport coefficient in order to understand the behaviour and properties of strongly interacting matter. This plays an important role in the hydrodynamic evolution of the matter produced in heavy-ion collisions where charge relaxation takes place. In

Ref. [135], the electrical conductivity is extracted from charge dependent flow parameters from asymmetric heavy-ion collisions. Experimentally, it has been observed that very strong electric and magnetic fields are created in the early stages (1-2 fm/c) of non-central collisions of nuclei at RHIC and LHC [135, 136]. The values of the electric and magnetic fields at RHIC are eE $\approx m_\pi^2 \approx 10^{21}$ V/cm and eB $\approx m_\pi^2 \approx 10^{18}$ G [136]. Such a large electrical field influences the medium, which depends on the electrical conductivity. $\sigma_{\rm el}$ is responsible for producing an electric current in the early stage of the heavy-ion collision.

Although with the prior knowledge of color charges and the associated electric charges of the quarks, one might presume the QCD matter to be highly conductive. In the contrary, this assumption fails due to the high interaction rates of the produced QCD matter, which again suggests low shear viscosity to entropy density (η/s). In highly conducting quark-gluon plasma the screening of external electromagnetic fields happen due to the high values of $\sigma_{\rm el}$ like the Meissner effect in superconductors as well as the "skin effect" for the electric current [176]. The electrical conductivity is one of the fundamental reasons for chiral magnetic effect [177], a signature of CP violation in the strong interaction. In view of this, a detailed study of electrical conductivity in the strongly interacting QCD matter is inevitable.

The experimental measurement of electrical conductivity ($\sigma_{\rm el}$) of the matter produced in heavy-ion collisions is not possible. Its information can be extracted from flow parameters measured in heavy-ion collision experiments [135]. Recently, various theoretical approaches have been used to study the electrical conductivity [176, 178–191]. $\sigma_{\rm el}$ is also related to the soft dilepton production rate [192] and the magnetic field diffusion in the medium [193, 194].

In our work [195], we develop the formulation for evaluating the electrical conductivity of strongly interacting matter using the color string percolation approach. To calculate the electrical conductivity of strongly interacting matter, which is one of the most important transport properties of QCD matter, we proceed as follows. The mean free path, which describes the relaxation of the system far from equilibrium can be written in terms of number density and cross-section as,

$$\lambda_{\text{mfp}} = \frac{1}{n\sigma_{\text{tr}}}, \tag{4.22}$$

where n is the number density of an ideal gas of quarks and gluons and σ_{tr} is the transport cross-section. In CSPM the number density is given by the effective number of sources per unit volume

$$n = \frac{N_{\text{sources}}}{S_{\text{n}}L}. \tag{4.23}$$

Here, L is the longitudinal extension of the string $\sim$1 fm. The area occupied by the strings is given by the relation $(1 - e^{-\xi})S_{\text{n}}$. Thus, the effective number of sources is given by the total area occupied by the strings divided by the area of an effective string, $S_1F(\xi)$ as shown below,

$$N_{\text{sources}} = \frac{(1 - e^{-\xi})S_{\text{n}}}{S_1F(\xi)}, \tag{4.24}$$

In general, N_{sources} is smaller than the number of single strings. N_{sources} equals to the number of strings N_{s} in the limit of $\xi = 0$. So,

$$n = \frac{(1 - e^{-\xi})}{S_1F(\xi)L}. \tag{4.25}$$

Now, using eqs. 4.22 and 4.25, we get,

$$\lambda_{\text{mfp}} = \frac{L}{(1 - e^{-\xi})}, \tag{4.26}$$

where σ_{tr}, the transverse area of the effective strings equals to $S_1F(\xi)$. Now we derive the formula for electrical conductivity. For this, we use Anderson-Witting model, in which the Boltzmann transport equation is given as [196],

$$p^{\mu}\partial_{\mu}f_k + qF^{\alpha\beta}p_{\beta}\frac{\partial f_k}{\partial p^{\alpha}} = \frac{-p^{\mu}u_{\mu}}{\tau}(f_k - f_{eq,k}), \tag{4.27}$$

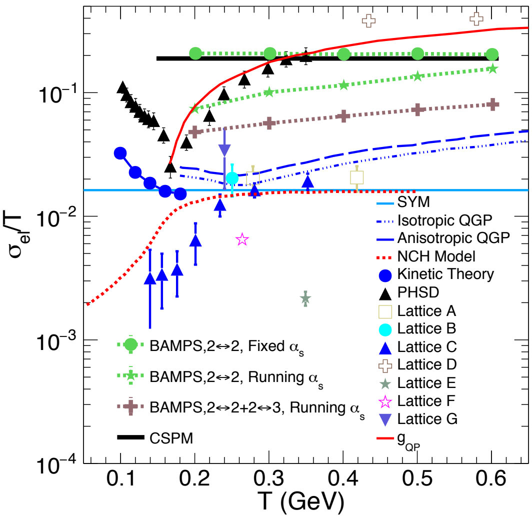

Figure 4.14: (Colour online) $\sigma_{\rm el}/$T versus T plot [195]. The black solid line is the result obtained in CSPM and black triangles are PHSD results [176]. The green and brown dotted lines correspond to various BAMPS results [197]. The NCH model [189] results are shown by the red dotted line. The blue circles are kinetic theory calculations [198]. The horizontal line is the result obtained for conformal supersymmetric (SYM) Yang-Mills Plasma [199]. Lattice data: lattice A- G [180–186, 200] are also shown by various symbols in the figure. The results for isotropic and anisotropic QGP [201] are shown by the blue dash-dotted and dashed lines, respectively. The red solid line depicts the results of quasi-particle (QP) model [188].

where $f_k = f(x, \overrightarrow{p}, t)$ is the full distribution function and $f_{eq,k}$ is the equilibrium distribution function of k$^{\rm th}$ species. τ is the mean time between collisions and u_μ is the fluid four velocity in the local rest frame. Eq. 4.27 provides a straightforward calculation of the quark distribution after applying the electric field. The gluon distribution function remains thermal and not altered by electric field. Here, we assume that there are as many quarks (charge q) as anti-quarks (charge -q) and uncharged gluons in the system. $F^{\alpha\beta}$ is the electromagnetic field strength tensor given by electric field and the magnetic flux tensor as [197],

$$F^{\mu\nu} = u^\nu E^\mu - u^\mu E^\nu - B^{\mu\nu}. \tag{4.28}$$

Since we study the effect of electric field, the magnetic field is set to zero, $B^{\mu\nu} = 0$ in the calculations. The electric current density of the k$^{\rm th}$ species in the x-direction is given as,

$$j_k^x = q_k \int \frac{d^3pp^x}{(2\pi)^3p^0} f_k = g_k\tau \frac{8}{3}\frac{\pi q_k^2 T^2}{(2\pi)^3} E^x. \tag{4.29}$$

According to Ohm's law, $j_k^x = \sigma_{el} E^x$. Using eq. 4.29 and relation $n_k = g_k T^3/\pi^2$, electrical conductivity in the assumption of very small electric field and no cross effects between heat and electrical conductivity in the relaxation time approximation is given by,

$$\sigma_{\rm el} = \frac{1}{3T}\sum_{\rm k=1}^{M} q_{\rm k}^2 n_{\rm k} \lambda_{\rm mfp}, \tag{4.30}$$

Putting eq. 4.26 in Eq. 4.30 and considering the density of up quark(u) and its antiquark($\bar{u}$) in the calculation, we get the expression for $\sigma_{\rm el}$ as,

$$\sigma_{\rm el} = \frac{1}{3T}\frac{4}{9} e^2 n_{\rm q}(T) \frac{L}{(1-e^{-\xi})}. \tag{4.31}$$

Here, the pre-factor 4/9 reflects the fractional quark charge squared ($\sum_{\rm f} q_{\rm f}^2$) and $n_{\rm q}$ denotes the total density of quarks or antiquarks. Here, e^2 in the natural unit is taken as $4\pi\alpha$, where $\alpha = 1/137$. The lQCD estimations

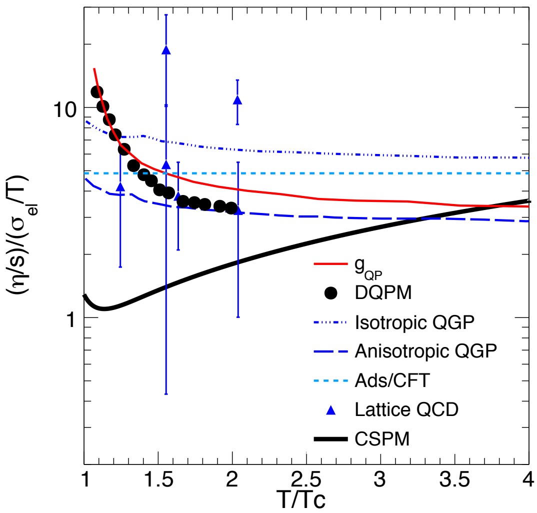

Figure 4.16: (Colour online) The ratio η/s and $\sigma_{\rm el}$/T as a function of T/T$_{\rm c}$ [195]. The black solid line is the CSPM result and broken lines are results from Ref. [201]. The symbols are lattice QCD results [188]. The DQPM and QP results are shown by the black circles and red solid line, respectively [188].

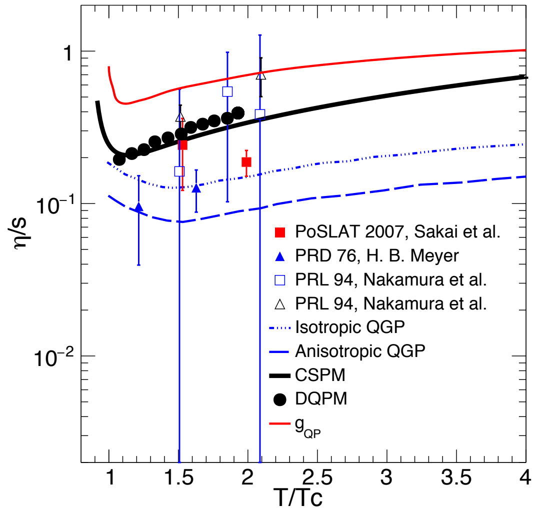

Figure 4.15: (Colour online) The ratio η/s as a function of $\mathrm{T/T_c}$ [195]. The black solid line is the CSPM result and broken lines are results from Ref. [201]. The symbols are lattice QCD results: full triangles [202], open squares and open triangles [203], full squares [204]. The black circles are the results obtained in DQPM [205]. The red solid line is QP model results [188].

i.e. lattice A - G [180–186, 200] are shown in the figure for comparison. The green and brown dotted lines are the result of microscopic transport model BAMPS [197], in which the relativistic (3+1)- dimensional Boltzmann equation is solved numerically to extract the electric conductivity for a dilute gas of massless and classical particles described by the relativistic Boltzmann equation. The green dotted line with the solid circles is the result for only elastic processes 2↔2, where strong coupling constant (α_s) is taken as constant ($\alpha_s = 0.3$) and the green dotted line with the solid stars is with the same setup for the running α_s. The brown dotted line with the brown plus symbols is the BAMPS result, where both elastic 2↔2 and inelastic 2↔3 processes are taken into consideration with the running α_s. The BAMPS results show a slower increase of $\sigma_{\rm el}/\mathrm{T}$ with temperature for both the cases of running α_s as the effective cross section changes with the temperature, while $\sigma_{\rm el}/\mathrm{T}$ remains almost independent of temperature for the case of constant α_s. The BAMPS results are above the lQCD results. The solid black line shows our results of CSPM for u- quark and its antiquark calculated using eq. 4.31. We observe that $\sigma_{\rm el}/T$ is almost independent of temperature and matches with the results of BAMPS with constant α_s, which may be due to the similar basic ingredients and procedure for the estimation of $\sigma_{\rm el}/T$.

Although the percolation of string approach is not directly obtained from QCD but it is QCD inspired, as like the BAMPS model is governed by pQCD. The basic ingredients for the percolation are strings, which are stretched between the partons of the projectile and target and forms color electric and magnetic field in the longitudinal directions. The color strings fragment into $q - \bar{q}$ and/or $qq - \bar{q}q$ pairs and form hadrons [53]. In the present study, we consider the strings to fragment into only $u - \bar{u}$ pairs. We use Drude formula in the relativistic case to estimate the electrical conductivity, which can be obtained after solving the relativistic Boltzmann transport equation with some approximations as mentioned in the formulation section. So the observation proclaims the almost similar approach of both the models for the calculation of $\sigma_{\rm el}/T$. It has been shown in Ref. [206] that the real electrical conductivity can be even more than a 50% larger than the estimate of the Drude formula unless the cross section is isotropic (no angular dependence).

A non-conformal holographic model [189] is used to estimate the electrical conductivity of the strongly coupled QGP, which is shown by the red dashed line and explains the lQCD data qualitatively. Kinetic theory [198] is also used to calculate electrical conductivity of hadron gas whose results are shown by blue circles in the figure, which shows a decrease of $\sigma_{\rm el}$/T with temperature. The electrical conductivity for conformal Yang-Mills plasma [199] is also shown by the horizontal line in the figure. The blue dash-dotted and dotted lines are the results for QGP obtained using the quasi-particle model for quark and gluons [201] for isotropic and anisotropic cases, respectively. Here, all the quarks and antiquarks have both the masses i.e. thermal and bare. The thermal masses of quarks and antiquarks arise due to the interaction with the constituents of the medium. Parton-Hadron-String Dynamics (PHSD) model results [176] are also shown by the black triangles in the figure for both the phases-hadron gas and quark-gluon plasma with different approaches. The hadron-string-dynamics transport approach has been used for the hadronic sector PHSD, while the partonic dynamics in the PHSD is based on the dynamical quasiparticle model (DQPM). σ_{el} in PHSD decreases with temperature in hadronic phase when approaches towards $\mathrm{T_c}$ and increases almost linearly for $\mathrm{T_c} < \mathrm{T}$, in the partonic phase after a sudden drop around $\mathrm{T_c}$. The calculations of quasi-particle (QP) model [188] are also shown in the figure by solid red line, which match with the PHSD results for QGP phase.

Figure 4.15 shows the variation of η/s as a function of $\mathrm{T/T_c}$. We have also shown η/s as a function of $\mathrm{T/T_c}$ again comparing with same model results taken for $\sigma_{\mathrm{el}}/\mathrm{T}$ to acquire a overall picture. Here, $\mathrm{T_c}$ is the critical temperature which is different in different model calculations. The black solid line is the CSPM result and the broken lines are quasiparticle model results [201]. Here, the dotted line is the result for anisotropic case while the dash-dotted is for isotropic case. A direct comparison with anisotropic QGP gives a feeling of temperature dependent effect of anisotropy on the discussed observables in figures 4.15 and 4.16. However, the comparison with the results for isotropic case is only meaningful for CSPM calculations unless the partons are considered as massless. The blue triangle symbols are results of lQCD with (2+1)- dynamical flavours [202–204]. The black circles are the estimations from dynamical quasiparticle model (DQPM) [205]. The red line is the results obtained in QP model [188]. In CSPM, η/s first decreases and after reaching a minimum value, it starts increasing with temperature. Thus, it forms a dip which occurs at $\mathrm{T/T_c} = 1$. The quasi-particle model results [201] show a similar behaviour but the dip does not occur at critical temperature in this case. We notice that CSPM results are close to the DQPM predictions and stay little higher than the results obtained in the quasiparticle model.

Recently, the ratio $(\eta/\mathrm{s})/(\sigma_{\mathrm{el}}/\mathrm{T})$ has gained a considerable interest in heavy-ion phenomenology [188]. QGP is expected as a good conductor due to the presence of deconfined color charges. A small value of η/s suggests large scattering rates which can damp the conductivity. Since, we know that η/s is affected by the gluon-gluon and quark-quark scatterings while $\sigma_{\rm el}$ is only affected by the quark-quark scatterings [188]. Thus, the ratio between them is important to quantify the contributions from quarks and gluons in various temperature regions. In this work, we have studied this ratio as a function of temperature using CSPM. In Fig. 4.16, we show the ratio of η/s and $\sigma_{\rm el}$/T versus T/T$_{\rm c}$. It is observed that, this ratio behaves in a similar fashion as η/s. We have also shown the results obtained for the isotropic and anisotropic QGP using a quasi-particle model [201]. Again, the comparison with the isotropic case is only meaningful. CSPM results are also confronted with the interpolated lattice QCD data [188] and explain the data within errorbars. The dotted horizontal line is the Ads/CFT calculation [188] for strongly coupled system. We also show the results obtained in DQPM and QP by the black circles and red line, respectively.

4.5 Energy and centrality dependence study in CSPM

We have extended our study to investigate the energy and centrality dependence of percolation parameters at various RHIC energies ranging from $\sqrt{s_{\rm NN}}$ = 19.6 to 200 GeV using CSPM [207]. We use these parameters to calculate the centrality dependence of thermodynamical observables such as initial temperature of the percolation cluster, energy density, average transverse momentum, shear viscosity to entropy density ratio, and trace anomaly at RHIC energies. The basic formulation has been used as described in Sec. 4.3. Eq. 4.12 is changed to consider centrality dependent study as,

$$\frac{d^2N_{\rm ch}}{dp_T^2} = \frac{a}{(p_0\sqrt{F(\xi)_{pp}/F(\xi)^{cent}_{\rm Au+Au}} + p_T)^{\alpha}}. \tag{4.32}$$

Here $F(\xi)_{Au+Au}^{cent}$ is the centrality dependent color suppression factor and $F(\xi)_{pp} \sim 1$ at low energies due to the low overlap probability. In the present work [207], we have extracted ξ and $F(\xi)$ at mid-rapidity ($|y| < 0.5$) for different centrality classes using the transverse momentum spectra of charged particles produced in Au+Au collisions at RHIC energies from $\sqrt{s_{\rm NN}}$ = 19.6 to 200 GeV [157, 158, 208, 209]. Figure 4.17 shows the extracted percolation density parameter, ξ as a function of number of participants (N$_{\rm part}$) in Au + Au collisions for $\sqrt{s_{\rm NN}}$ = 19.6 to 200 GeV. The proton to pion ratio is affected by baryon stopping at lower center-of-mass energies. We do not consider the results of percolation density parameter for $\sqrt{s_{\rm NN}}$ = 7.7 and 11.5 GeV, as for these energies the proton to pion ratios are much larger compared to higher collision energies. The ξ values are obtained by fitting the experimentally measured transverse momentum spectra of charged particles. N$_{\rm part}$ values for different centrality classes are obtained by using Glauber model calculation [210]. The uncertainties in ξ are estimated by varying the fitting conditions. The associated systematic uncertainties in percolation density parameters are $\sim$ 3%. We have propagated the uncertainties for other observables accordingly.

It is observed that ξ values are higher for higher centre-of-mass energies and increase with N$_{\rm part}$ for a particular energy. This indicates that the string overlap is greater for central collisions. The horizontal line corresponds to the critical percolation density parameter, $\xi_c \sim 1.2$. The critical density for the onset of continuum percolation has been determined in numerical studies for a variety of different systems. In 2-dimensions the threshold for percolation is $\xi_c \sim 1.2$ [141, 142, 211]. It is observed that $\xi_c > 1.2$ for N$_{\rm part} > 50$ at $\sqrt{s_{\rm NN}}$ = 130 and 200 GeV. Whereas, for the lower collision energies starting from $\sqrt{s_{\rm NN}}$ = 19.6 - 62.4 GeV, $\xi_c > 1.2$ for central collisions. This suggests that the percolation phase transition is expected for N$_{\rm part} > 50$ at $\sqrt{s_{\rm NN}}$ = 130 and 200 GeV and for central collisions at lower energies. This is in conformity with the higher effective energy available for particle production in central collisions [212–215]. In Fig. 4.18, we show the extracted values of $F(\xi)$ as a function of pseudo-

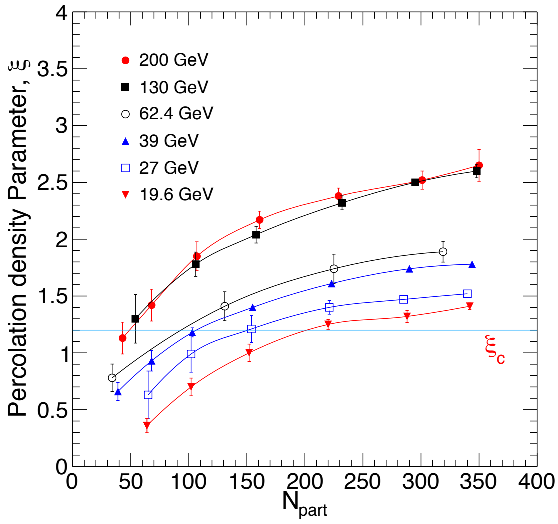

Figure 4.17: (Color online) Percolation density parameter ξ, as a function of number of participants ($\mathrm{N_{part}}$) for Au+Au collisions at RHIC energies from 19.6 - 200 GeV [207]. The symbols correspond to different centre-of-mass energies and the horizontal line is the critical percolation density.

rapidity density of the charged particles ($dN_{\rm ch}/d\eta$) for Au + Au collisions at RHIC energies from 19.6 to 200 GeV. $dN_{\rm ch}/d\eta$ values for different centrality classes are taken from experimental data [157, 158]. $F(\xi)$ decreases with increasing collision energies as well as centralities. The decreasing trend of $F(\xi)$ is due to the production of high string density, which reveals more suppression of color charges in comparison to lower collisions energies and centralities. $F(\xi)$ in heavy-ion collisions is presented as a function of $dN_{\rm ch}/d\eta$ scaled with the transverse overlap area $S_{\rm N}$, which are estimated by using the Glauber model [157] along with the results in high-multiplicity non-jet p$\bar{\rm p}$ collisions at $\sqrt{s}$ = 1.8 TeV from FNAL (Fermi National Accelerator Laboratory) E735 experiment [146] in Fig. 4.19. It is observed that $F(\xi)$ falls onto a universal scaling curve for hadron-hadron and nucleus-nucleus collisions. Particularly, in the most central Au+Au collisions and high multiplicity p$\bar{\rm p}$ collisions, $F(\xi)$ values fall in a line. This suggests that the percolation string densities are independent of collision energies and collision systems.

The initial temperature, $T(\xi)$ for different centrality classes is obtained from $F(\xi)$ by using eq. 4.13 for all the energies. Figure 4.20 shows $T(\xi)$ as a function of $\mathrm{N_{part}}$. It is found that $T(\xi)$ increases with $\mathrm{N_{part}}$ as well as with the centre-of-mass energy. Figure 4.21 represents the initial temperatures versus $dN_{\mathrm{ch}}/d\eta/S_{\mathrm{N}}$ for various collision energies and systems and we notice that it follows a universal curve for hadron-hadron and nucleus-nucleus collisions. The horizontal line at T $\sim$ 165 MeV is obtained by comparing the hadron yields measured in different collision systems such as pp, A+A, and $e^{+} + e^{-}$ with the statistical hadron gas model [152]. This temperature corresponds to the critical percolation density, ξ_c, where percolation phase transition takes place. The initial temperatures obtained in most and mid-central collisions at RHIC energies and in high multiplicity hadron-hadron collisions at $\sqrt{s} = 1.8$ TeV are above the hadronisation temperature, which evokes the creation of deconfined matter in these collision energies and systems.

The mean transverse momentum $\langle p_T \rangle$ of pions as a function of initial temperature $T(\xi)$ is shown in Fig. 4.22. The results are presented for different centralities at RHIC energies. The available $\langle p_T \rangle$ values are taken from the experimental data [157, 158] and $T(\xi)$ are calculated using the CSPM as mentioned above. $\langle p_T \rangle$ values show a scaling behaviour as a function of the initial temperature for all the colliding energies. We notice that, $\langle p_T \rangle$ in the most central collisions of lower energies overlaps with that obtained in the most peripheral collisions of higher energies, which may hint the formation of similar systems in the peripheral collisions at higher energies as formed in the most central collisions at lower energies. Again, this supports the hypothesis of effective energy for particle production [212–215].

Figure 4.23 shows the variation of the energy density, estimated by using eq. 4.14 with ξ for different centrality classes at RHIC energies. It is found that ε is proportional to ξ for all the centrality bins. In our previous work [144], we observed that ε is proportional to ξ. Similarly, here we fit the results with a linear function, $\varepsilon = \mathrm{A}\times\xi$ (GeV$/fm^3$) for different centrality classes and extract the parameters. The parameter, $A = 0.786,\ 0.693,\ 0.654,\ 0.649$ (GeV$/fm^3$) for 0-10%, 10-20%, 20-30%, 30-40% centrality classes, respectively. It shows a decreasing trend from

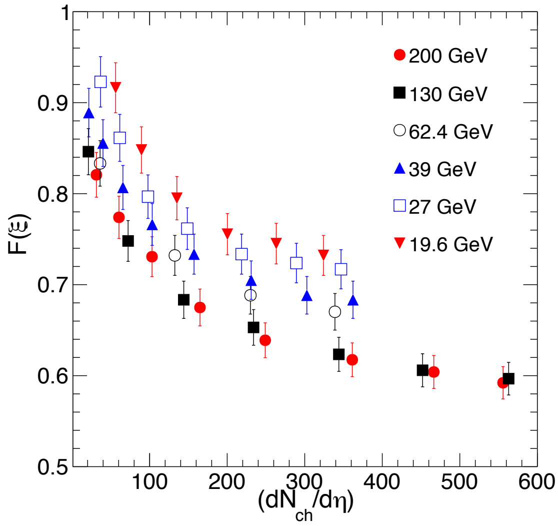

Figure 4.18: (Color online) Color Suppression factor $F(\xi)$, as a function of charged particle pseudorapidity density, $dN_{\rm ch}/d\eta$ [207]. Different symbols represent different centre-of-mass energies.

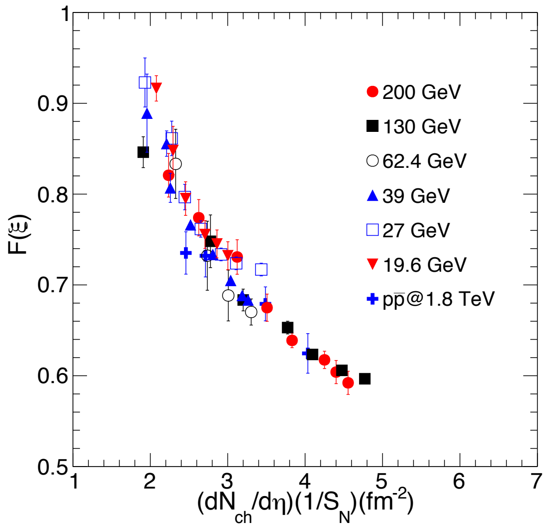

Figure 4.19: (Color online) Color Suppression factor $F(\xi)$, as a function of pseudorapidity density divided by the nuclear overlap function, $(dN_{\rm ch}/d\eta)/S_{\rm N}$ [207]. Different symbols represent different centre-of-mass energies along with high-multiplicity non-jet $p\bar{p}$ collisions at $\sqrt{s}$= 1.8 TeV at Tevatron [146].

central to peripheral collisions as expected.

Figure 4.24 shows the initial temperature estimated by using CSPM at RHIC energies and the chemical freeze-out temperatures as a function of centre-of-mass energy. The chemical freeze-out temperatures are obtained by fitting the experimental yield of hadrons [158] for different centralities in Au+Au collisions at $\sqrt{s_{\rm NN}}$ = 19.6 - 200 GeV. We observe that the ini-

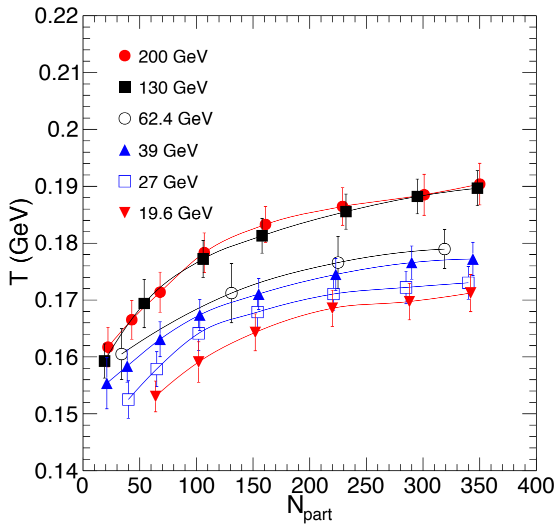

Figure 4.20: (Color online) The initial temperatures at RHIC energies estimated in CSPM as a function of number of participants ($\mathrm{N_{part}}$) for Au+Au collisions [207].

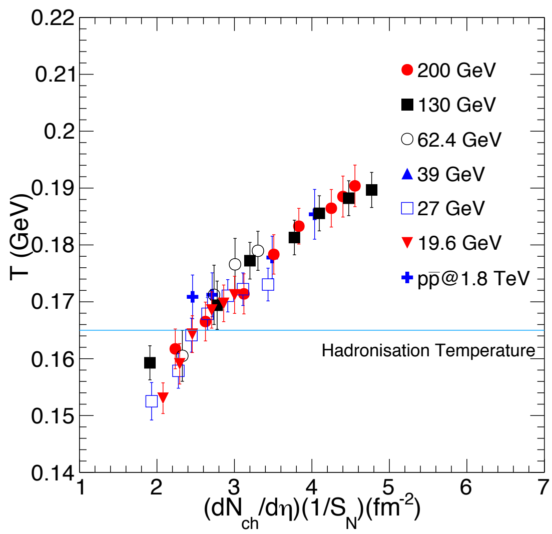

Figure 4.21: (Color online) Temperature as a function of $(dN_{\mathrm{ch}}/d\eta)/S_{\mathrm{N}}$ from pp and Au + Au collisions [207]. The horizontal line corresponds to T $\sim$ 165 MeV, which is the universal hadronisation temperature [152].

tial temperature increases with the collision energies for all the centralities while the chemical freeze-out temperatures remain constant within the uncertainties. Also, the initial temperatures are found close to the freeze-out temperatures at lower energies and the difference between them increases as we move towards the higher collision energies. A strong centrality dependence is found at higher energies in particular, at $\sqrt{s_{\mathrm{NN}}}$ = 130 and 200 GeV compared to the lower energies.

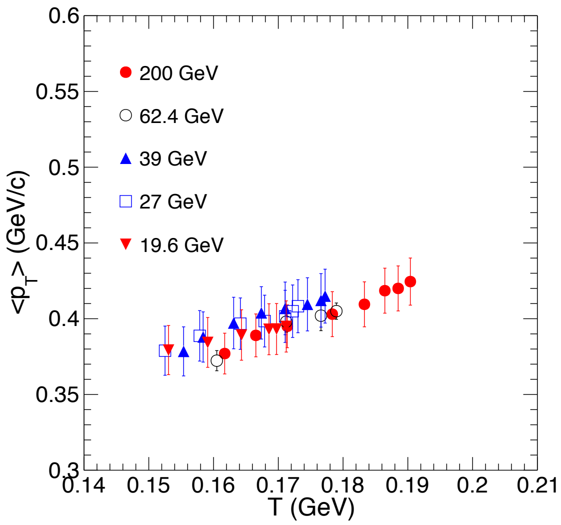

Figure 4.22: (Color online) Average momentum $\langle p_T \rangle$ of pions as a function of initial temperature, T. $\langle p_T \rangle$ are obtained from experimental data [157] and initial temperatures are estimated by using CSPM [207]. Different symbols are for different centre-of-mass energies.

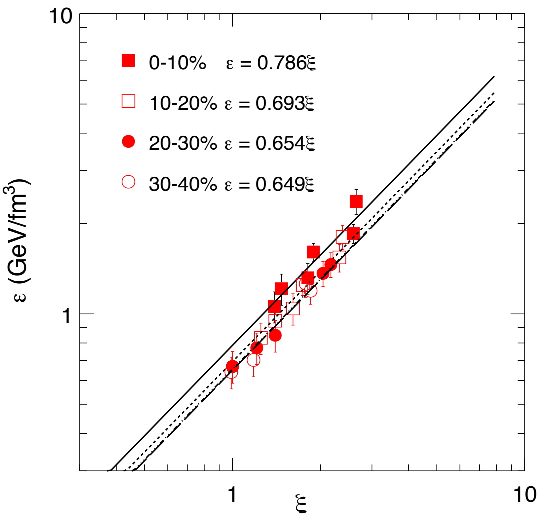

Figure 4.23: (Color online) Initial energy density, ε as a function of the percolation density parameter (ξ) for different centrality classes at RHIC energies from 19.6 to 200 GeV [207]. The different lines are the linear fits to data for different centralities.

We first investigate the centrality dependence of shear viscosity to entropy density ratio (η/s) for various RHIC energies, which act as a measure of the fluidity of the matter formed in heavy-ion collisions. We use eq. 4.18 to study the centrality dependence of η/s as a function of T as shown in the Fig. 4.25 for various RHIC energies, where higher T corresponds to the most central collisions and decreases as we go towards peripheral collisions

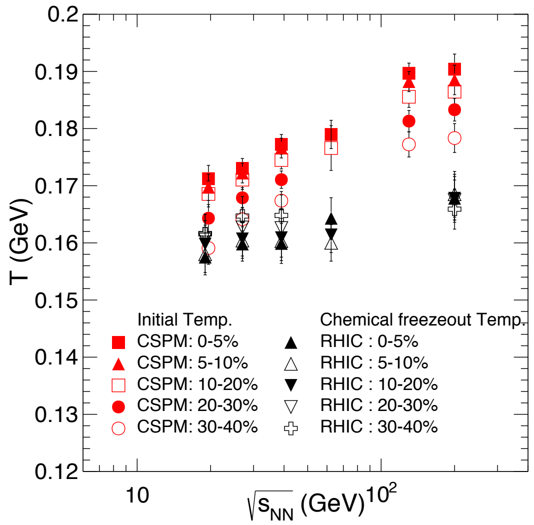

Figure 4.24: (Color online) Initial temperature, T estimated by using CSPM at RHIC energies (red symbols) and extracted chemical freeze-out temperatures for Grand Canonical Ensemble using the experimental data at RHIC energies [158] (black symbols) for different centrality classes [207].

for all energies. The horizontal line shown in this figure is the conjectured lower bound for η/s by Ads/CFT calculations [169]. It is perceived that, η/s decreases as we go from peripheral to central collisions at all the collision energies and found to be minimum at most central collisions at $\sqrt{s_{\mathrm{NN}}}$ = 130 and 200 GeV.

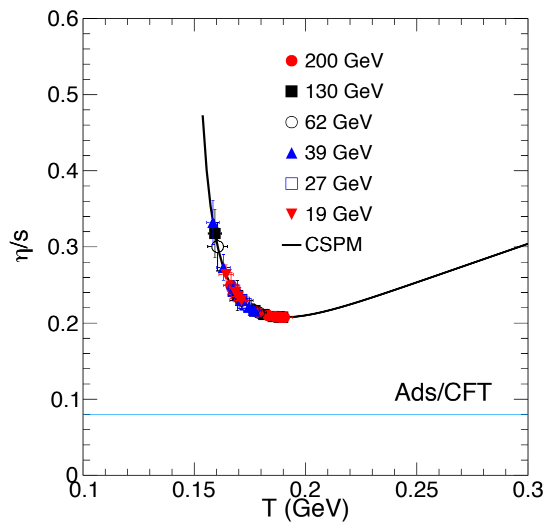

Figure 4.25: (Color online) η/s as a function of temperature. The markers show the results from various RHIC energies for different centrality bins from the CSPM [207]. The black solid line shows the extrapolation to higher temperatures from CSPM. The solid horizontal line around $1/4\pi$ represents the AdS/CFT limit [169].

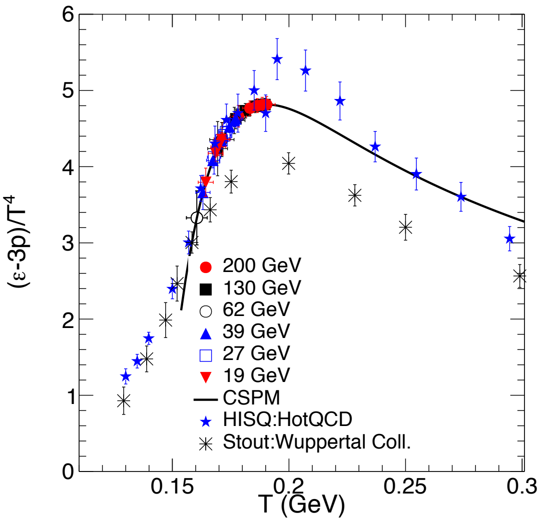

Figure 4.26: (Color online) Variation of trace anomaly $\Delta = (\varepsilon - 3P)/T^4$ with respect to temperature [207]. Blue star markers represent results from HotQCD collaboration [171]. Black asterisk markers refer to Wuppertal collaboration [172]. Different markers are the results obtained from CSPM for RHIC energies for different centrality bins and the black line represents the extrapolated CSPM results.

Figure 4.26 shows the centrality dependence of trace anomaly ($\Delta = (\varepsilon - 3P)/T^4$), which is the reciprocal of η/s versus temperature for different RHIC energies. We also compare the CSPM calculations with the LQCD data [171, 172] and find that CSPM results are closer to the HOT QCD collaboration results. Δ increases with centrality for all the RHIC energies and has its maximum value for the most central collisions at $\sqrt{s_{\rm NN}} = 130$ and 200 GeV.

4.6 Summary

We have presented the study of equilibrium thermodynamical and transport properties such as energy density, shear viscosity, trace anomaly, speed of sound, entropy density, and bulk viscosity of the QCD matter created at RHIC energies by using the clustering of color sources phenomenology. The color suppression factor $F(\xi)$ is obtained from the transverse momentum spectra of charged particles for most central heavy-ion collisions in order to obtain various observables. $F(\xi)$ is responsible for reduction in multiplicity and enhancement of transverse momentum.

It is observed that the results are in excellent agreement with the lattice QCD data. The initial temperatures at RHIC energies are presented with different model predictions of chemical freeze-out temperature (T_{ch}), and baryon chemical potential (μ_B). It is found that the initial temperatures at lower energies are very close to the chemical freeze-out temperatures. As the collision energy increases, the differences between the initial temperatures and the freeze-out temperatures increase. The ratio of shear viscosity over entropy density has been evaluated as a function of temperature at different center-of-mass energies. η/s decreases as a function of energy as well as temperature upto 200 GeV and then starts to increase. The whole picture is consistent with the formation of a fluid with a low η/s ratio. We found that ζ/s diverges near critical point. The trace anomaly as a function of temperature shows similar trend as the results obtained in HotQCD collaboration. The CSPM based analysis of RHIC data from STAR shows that the transition from de-confined to confined phase most likely will occur between $\sqrt{s_{\rm NN}}$ = 11.5 and 19.6 GeV of collision energy. The analysis of the pp collisions at $\sqrt{s}$ = 7 and 14 TeV at the LHC can map events with higher temperatures and energy densities.

We have developed a method to calculate the electric conductivity of strongly interacting matter using color string percolation approach. We use basically the well-known Drude formula for the estimation of electrical conductivity, which can be obtained after solving the Boltzmann transport equation in relaxation time approximation assuming very small electric fields and no cross-effects between heat and electrical conductivity. We see that the CSPM results for the conductivity stays almost constant with increasing temperature in a similar fashion as shown by BAMPS data and matches with the results obtained in BAMPS with the fixed strong coupling constant considering elastic cross section only. The CSPM results lie well above the lQCD results for all the temperatures. We have shown η/s as a function of $\mathrm{T/T_c}$ and compared our results with quasiparticle model results for isotropic and anisotropic cases, lQCD data, DQPM and QP model results. A similar behaviour is found for CSPM results as shown in lQCD data and other model predictions. But, our results lie above the results obtained from quasiparticle models. CSPM results go inline with that obtained in DQPM. We have also studied the ratio, $(\eta/s)/(\sigma_{\mathrm{el}}/T)$ as a function of T, which behaves in a similar manner as η/s varies. We have confronted CSPM results with the results obtained in quasiparticle model for isotropic and anisotropic QGP medium, lQCD predictions, estimations from DQPM and QP models. The results obtained in CSPM validate the outcomes from BAMPS calculations with fixed strong coupling constant and hardly explain the predictions of lQCD data.

We have presented the calculation of percolation parameters and various thermodynamical observables in nucleus-nucleus collisions at RHIC energies starting from $\sqrt{s_{\mathrm{NN}}}$ = 19.6 to 200 GeV as a function of collision centrality. We have extracted ξ and $F(\xi)$ for various centralities by fitting the transverse momentum spectra of charged particles in order to obtain thermodynamical observables. We find that, the critical percolation density ($\xi_c \sim 1.2$) is reached for the most central collisions at all the analysed collision energies. However, as we go towards peripheral collisions, the critical percolation density is difficult to achieve at lower collision energies. A universal scaling behaviour for the color suppression factor ($F(\xi)$) is observed for all the collision energies when ($F(\xi)$) is normalised by nuclear overlap area (S_{N}). The results from hadron-hadron collisions at $\sqrt{s} = 1.8$ TeV strengthen the observation showing a similar behaviour as obtained in Au+Au collisions. This indicates that the percolation string densities are independent of collision systems and collision energies. We have also shown the initial temperature as a function of $dN_{\mathrm{ch}}/d\eta$ scaled by S_{N} and find a universal scaling behaviour both in nucleus-nucleus and hadron-hadron collisions. It is also observed that the initial temperatures obtained in central collisions at RHIC energies and in high multiplicity hadron-hadron collisions at $\sqrt{s} = 1.8$ TeV are above the hadronisation temperature, which advocates the possibility of the creation of deconfined matter in these collision energies and systems is presented. This also justifies a deep look into the LHC pp high multiplicity events.

The average transverse momentum ($\langle p_T \rangle$) of pions as a function of temperature for various centralities at RHIC energies also shows a scaling behaviour as a function of the initial temperature. It is found that $\langle p_T \rangle$ in the most central collisions of lower energies overlap with that obtained in the most peripheral collisions of higher energies. This suggests that, the system formed in the peripheral collisions at higher energies is similar thermodynamically to that formed in the most central collisions at lower energies, justifying the hypothesis of effective energy. η/s as a function of temperature for different centralities are also studied in CSPM. A strong centrality dependence of η/s is found at RHIC energies. The minimum η/s is observed for the most central collisions at $\sqrt{s_{\rm NN}}$ = 130 and 200 GeV, which envisages the formation of perfect fluid at these energies.

It would be interesting to study other observables like, isothermal compressibility, thermal conductivity etc. using CSPM approach at other available collision energies and collision species.

Chapter 5

Limiting fragmentation in high-energy nuclear collisions

"Simplicity is the essence of universality."

– M. K. Gandhi

Understanding the particle productions in high energy nuclear collisions is always fascinating. The particle production in high energy collisions happens from three different regions: the projectile, the target and the central region. Particles emitted from the outer region are called projectile/target fragments. There are various nuclear fragmentation mechanisms discussed in literature [56, 216]. The most important are: a sudden fragmentation by explosive mechanisms, such as shock waves [216] and a slow fragmentation by the "fission" of the spectator regions, mainly because of the interactions with the particles or fragments emitted from the participant region at transverse angles in the center-of-momentum system [216]. The latter is a purely low-energy nuclear phenomenon, where as the former is more applicable to relativistic domain of energies. During the late 1960s, the hypothesis of limiting fragmentation became important to understand the particle production [55, 56]. According to this hypothesis the produced particles, in the rest frame of one of the projectile becomes independent of centre of mass energies, thus following a possible scaling (as a function of $\eta' = \eta \pm y_{\text{beam}}$), known as limiting fragmentation (LF). As (pseudo)rapidity is a longitudinal variable it is also called longitudinal scaling. Here $y_{\text{beam}} = \ln(\sqrt{s_{\text{NN}}}/m_{\text{p}})$, is beam rapidity and m_{p} is the mass of proton. There have been several attempts to understand the nature of hadronic interactions which lead to

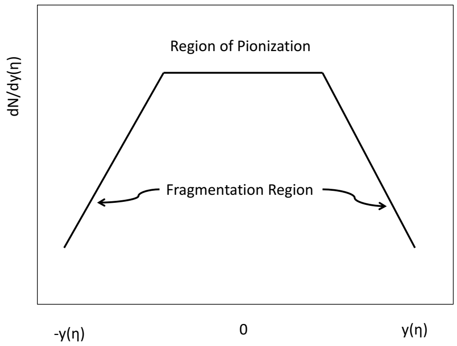

Figure 5.1: A schematic of (pseudo)rapidity distribution showing the pionization and fragmentation regions [238].

limiting fragmentation and the deviations from it [217–219].

It is expected that a central plateau develops at higher energies, which clearly separates the central rapidity from the fragmentation region. However, as such, there is no separating boundary between the central rapidity and the fragmentation region. The width of the fragmentation region is around 2-units in rapidity [220]. The fragmentation region thus, is expected to be well separated from the central region only in very high energies, as the kinematically available rapidity region is much wider than 4-units in rapidity. The particle production in fragmentation region is attributable to the valence quarks participating in hadronization, whereas in central rapidity region, it is dominated by the mid-rapidity gluonic sources at high energies [221, 222]. The central rapidity region is called Pionization region [220] and is shown in the Fig. 5.1.

There have been several experimental efforts to understand the particle production in both mid and forward rapidities [59, 223–229]. As LF is the thrust area of this paper we focus on the particle production in the forward rapidity region. The experimental observation of LF was first reported by the PHOBOS experiment at RHIC with charged particles [229], later STAR experiment also confirmed the hypothesis with inclusive photons in the forward rapidity [226]. The Limiting fragmentation was observed by

UA5 experiment at CERN for pp and p$\bar{\text{p}}$ collisions from 53 GeV to 900 GeV [230]. However, ALICE experiment at the LHC has reported a violation of LF hypothesis for inclusive photons in pp collisions with limited forward rapidity coverage [231].

Various theoretical works [218, 219, 232–237] have reported the observation of limiting fragmentation phenomenon in heavy-ion collisions. Recently, limiting fragmentation in the era of RHIC and LHC has got a special mention with a new concept called the hypothesis of "energy-balanced limiting fragmentation" [214, 215]. In Ref. [218], it is claimed that the cross-section plays an important role in fragmentation regions. Marian [219] has shown that the LF phenomenon is observed in the differential cross-section per unit pseudorapidity in proton+nucleus collisions at RHIC energies.

Our main aim in this work [238] is to study the phenomena of LF for the results of A+A collisions in view of increasing inelastic particle production cross-sections from RHIC to LHC energies. The hypothesis of limiting fragmentation can be tested for both the observables, namely the particle multiplicity density and also the differential crosssection. As LF is least explored in the case of differential cross-section, this work focuses on the later observable with a detailed discussion on multiplicity as well, for a clear comparison of the expected results at the LHC energies. The total hadronic cross-section is not a constant from lower RHIC energy to highest LHC energy but is a slowly growing function of $\sqrt{s}$ [117]. The particle production in heavy-ion collisions depends on the hadronic cross-section. Thus, a detailed study of the longitudinal scaling behaviour in terms of cross-section could be a prudent attempt. The longitudinal variables are expected to be sensitive to the available energy and the multiplicity of the produced secondaries. In this context, the study of possible longitudinal scaling of the final state multiplicity as a function of collision energy becomes judicious, in view of increasing inelastic particle production cross-sections at LHC energies. The paper is organised as follows: in Sec. 5.1, we recapitulate the basics of Landau hydrodynamics and its connection with the limiting fragmentation hypothesis. In Sec. 5.2, we present the methodology to calculate the differential cross-section per unit pseudorapidity and discuss the results obtained using experimental data and AMPT. Finally, we summarise our findings in Sec. 5.3.

5.1 Landau Hydrodynamics and Limiting Fragmentation Hypothesis

The angular distribution of the particles produced in high-energy collisions is described by the famous Landau model with relativistic hydrodynamics given by the conservation of energy momentum tensor, $\partial_\mu T^{\mu\nu} = 0$ with a blackbody equation of state, $p = \epsilon/3$, p is the pressure and ϵ is the energy density [239, 240]. Landau hydrodynamical model assumes complete thermalization of the total energy in the Lorentz contracted volume of the fireball, which makes the initial energy density to grow with collision energy [241]. The formulation given in [241] gives rise to the initial entropy of the system, which is produced in the thermalization process of the quanta of the system, to follow a Gaussian distribution in the rapidity space. The width of the rapidity distribution is determined by the Lorentz contraction factor and is related to the speed of sound [242]. The multiplicity distribution in the rapidity space, thus becomes [156, 239, 240]

$$\frac{dN}{dy} = \frac{Ks^{1/4}}{\sqrt{2\pi L}} \exp\left(-\frac{y^2}{2L}\right), \tag{5.1}$$

where $L = \sigma_y^2 = (1/2)\ln(s/m_p^2) = \ln(\gamma)$. Eq. 5.1 can be rewritten as

$$\frac{dN}{dy} = \frac{Ks^{1/4}}{\sqrt{2\pi y_{\mathrm{beam}}}} \exp\left(-\frac{y^2}{2y_{\mathrm{beam}}}\right). \tag{5.2}$$

The conclusion from Ref. [241] shows that the hypothesis of limiting fragmentation comes naturally in Landau's model of multiparticle production. Following the LF hypothesis, when the rapidity distribution is seen from one of the projectile's rest frame, i.e. by transforming to

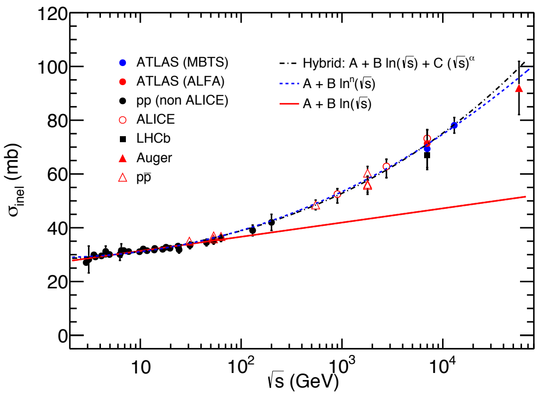

Figure 5.2: The inelastic cross-section as a function of $\sqrt{s}$ [238]. The symbols are experimental data [57, 243–245] and the fitted lines are phenomenologically motivated functions.

$y' = y - y_{\text{beam}}$, the above expression for rapidity distribution becomes ($dN/dy = dN/dy'$) [241],

For $y' = 0$, the distribution only depends on the Lorentz contraction factor, which is a function of collision energy. When we make the transformation, $y' = y - y_{\text{beam}}$, the fragmentation region shifts by a factor y_{beam}, a value which increases with the collision energies, making the region to overlap with each other.

5.2 Limiting Fragmentation at the LHC

In this section, we study the limiting fragmentation phenomenon in the pseudorapidity distributions of differential cross-section of charged particles ($d\sigma/d\eta$) for A+A collisions at various center-of-mass energies starting from 19.6 GeV to 5.02 TeV. Due to lack of experimental data of $d\sigma^{AA}/d\eta$, we take the experimentally measured $dN_{\text{ch}}^{AA}/d\eta$ at various collision energies. We transform $dN_{\text{ch}}^{AA}/d\eta$ into $d\sigma^{AA}/d\eta$ using nucleon-nucleon inelastic cross-sections (σ_{in}) for different energies applying the method discussed below. A very detailed study is needed to make the connection possible. Recent studies [219] shows that the longitudinal scaling of the differential cross-section per unit pseudorapidity is observed in the experimental data for higher RHIC energies. The rationale behind our work is to bring in the direct center-of-mass energy dependence of σ_{in}, which has a different low-energy behaviour up to the top RHIC energy in comparison to the LHC energies. This is also observed from the experimentally measured values of σ_{in} [57, 243–245], which are shown in the Fig. 5.2. In this figure, we show the variation of σ_{in} with collision energy. It is clearly seen that there is a very slow rise of σ_{in} at lower collision energies up to the top RHIC energy. We have fitted the experimental data with various phenomenologically motivated functions in order to understand the energy-dependent behaviour of σ_{in}. A logarithmic function, A + B $\ln(\sqrt{s})$, with A and B as free fitting parameters explains the data only up to RHIC energies. This seems to deviate completely after the top RHIC energy. The σ_{in} data beyond the top RHIC energy do not follow a logarithmic behaviour. To study the complete energy-dependent behaviour, we have used a hybrid function, A + B $\ln(\sqrt{s})$ + C$(\sqrt{s})^{\alpha}$, which combines logarithmic and a power-law to fit the data. Here A, B, C and α are free parameters. This hybrid function explains the data from lower to higher energies. We have also fitted the data with a function A + B $\ln^{\mathrm{n}}(\sqrt{s})$, where A and B are free parameters. A more detailed discussions could be found in Ref. [117]. This seems to describe the data very well. These findings suggest that the logarithmic function alone cannot explain the data for higher energies, while the power of logarithmic function and the hybrid function mentioned above could explain from lower to higher energies shown in the figure. The σ_{in} at LHC energies showing a different functional behaviour than the lower energies necessitates a relook into the hypothesis of limiting fragmentation.

Considering the crude approximation to the physical situation in the framework of Landau hydrodynamical model of particle production, the relationship between the differential cross-section per unit pseudorapidity ($d\sigma^{\mathrm{pp}}/d\eta$) and the pseudorapidity distribution ($dN_{\mathrm{ch}}^{\mathrm{pp}}/d\eta$) of charged particles for pp collisions is given as [246],

$$\frac{d\sigma^{\mathrm{pp}}}{d\eta} = \sigma_{\mathrm{in}} \left(\frac{dN_{\mathrm{ch}}^{\mathrm{pp}}}{d\eta} \right). \tag{5.3}$$

Now, the relation of charged particle pseudorapidity distribution in A+A collisions with the charged particle pseudorapidity distribution in pp collisions using a two-component model, where the contributions from soft and hard processes in the particle production are taken separately, is given as [247, 248],

$$\frac{dN_{\rm ch}^{\rm AA}}{d\eta} = \frac{dN_{\rm ch}^{\rm pp}}{d\eta}\left((1-x)\frac{< N_{\rm part} >}{2} + x < N_{\rm coll} >\right). \tag{5.4}$$

Here, x and $(1-x)$ are the fractions of contribution to the particle production from hard and soft processes, respectively.

Using Eq. 5.4 in Eq. 5.3, we get a relation between the differential cross-section per unit pseudorapidity in pp collisions and the charged particle pseudorapidity distribution in heavy-ion collisions as follows:

$$\frac{d\sigma^{\rm pp}}{d\eta} = \frac{\sigma_{\rm in}\left(\frac{dN_{\rm ch}^{\rm AA}}{d\eta}\right)}{\left((1-x)\frac{<N_{\rm part}>}{2} + x < N_{\rm coll} >\right)}. \tag{5.5}$$

Now, we proceed towards deriving relationship between differential cross-section per unit pseudorapidity in pp collisions with that in A+A collisions. The distribution of quarks and gluons in a nucleus is different from that in a nucleon with a small effect ($< 10\%$) of shadowing and EMC effects [249]. With a crude approximation one can assume that the gluon distribution in a nucleus is just A times that for a proton, where A is the atomic number. The production is expected to increase by a factor of A^2 when two nuclei of atomic number A collide in a central way and the pseudorapidity spectrum transforms as [250],

$$\frac{d\sigma^{\rm AA}}{d\eta} = \mathrm{A}^2\left(\frac{d\sigma^{\rm pp}}{d\eta}\right). \tag{5.6}$$

Using Eqs. 5.5 and 5.6, we write the differential cross-section per unit pseudorapidity in terms of charged particle pseudorapidity distribution for the heavy-ion collisions as,

Table 5.1: The values of parameters obtained from the fitting of experimental data of $dN_{\rm ch}/d\eta$ with the double Gaussian function given by Eq. 5.8

Parameters	$\sqrt{s_{\rm NN}}$ = 2.76 TeV	$\sqrt{s_{\rm NN}}$ = 5.02 TeV
A_1	2592.29 ± 311.56	2102.16 ± 28.39
A_2	959.59 ± 304.26	1817.56 ± 37.90
σ_1	3.27 ± 0.13	4.75 ± 0.01
σ_2	1.67 ± 0.23	0.61 ± 0.14

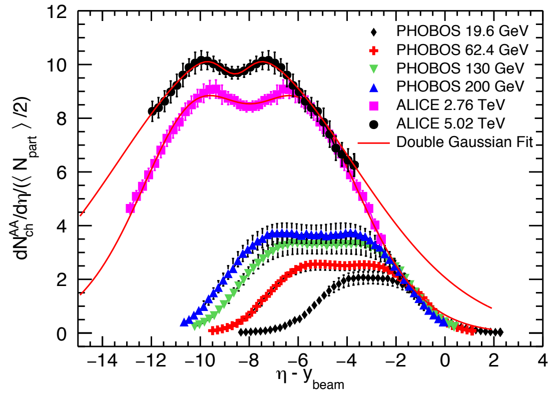

Figure 5.3: The number of participant pair normalized pseudorapidity distribution of charged particles ($dN_{\rm ch}^{\rm AA}/d\eta$) in heavy-ion collisions versus $\eta - y_{\rm beam}$ for various energies [238]. The symbols are experimental data [57, 251–253] and the lines are the double Gaussian fits.

$$\frac{d\sigma^{\rm AA}}{d\eta} = \frac{{\rm A}^2\sigma_{\rm in}\left(\frac{dN_{\rm ch}^{\rm AA}}{d\eta}\right)}{\left((1-x)\frac{<N_{\rm part}>}{2} + x < N_{\rm coll} >\right)}. \tag{5.7}$$

A large number of experimental data on the charged particle pseudorapidity distribution are available at various center-of-mass energies ranging from RHIC energies like $\sqrt{s_{\rm NN}}$ = 19.6, 62.4, 130 and 200 GeV to LHC energies such as $\sqrt{s_{\rm NN}}$ = 2.76 and 5.02 TeV [57, 251–253]. In a recent paper by the ALICE experiment [252], the limiting fragmentation phenomenon is studied in the pseudorapidity distribution of charged particles at RHIC and LHC energies. At $\sqrt{s_{\rm NN}}$ = 2.76 TeV, the authors have used a double Gaussian function to extrapolate the data in the fragmentation region and find that the phenomenon of LF is observed at this energy.

In Fig. 5.3, we have shown $dN_{\rm ch}^{\rm AA}/d\eta/(< N_{\rm part} > /2)$ as a function of $\eta - y_{\rm beam}$ for various energies from 19.6 GeV to 5.02 TeV. Due to lack of the experimental data in the fragmentation region at LHC energies, we

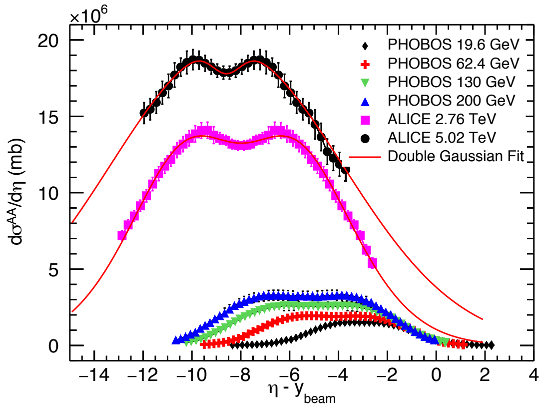

Figure 5.4: The differential cross-section per unit pseudorapidity ($d\sigma^{\mathrm{AA}}/d\eta$) as a function of $\eta - y_{\mathrm{beam}}$ for various collision energies [238]. The symbols are experimental points and the lines are double Gaussian fits.

have used double Gaussian function to fit and extrapolate the experimental data in the projectile rapidity region. The double Gaussian function used for fitting is given as follows,

$$f(\eta) = A_1 e^{\frac{-\eta^2}{2\sigma_1^2}} - A_2 e^{\frac{-\eta^2}{2\sigma_2^2}}, \tag{5.8}$$

where A_1, A_2 are the amplitudes and σ_1, σ_2 are widths of the double Gaussian function. This function describes the experimental data very well at LHC energies within uncertainties [252, 253]. The fitting parameters are given in the table 5.1 for $\sqrt{s_{\mathrm{NN}}} = 2.76$ and 5.02 TeV. We observe that the limiting fragmentation phenomenon seems to be violated at $\sqrt{s_{\mathrm{NN}}} =$ 5.02 TeV, while it is observed at energies from $\sqrt{s_{\mathrm{NN}}} = 19.6$ GeV to 2.76 TeV. Despite this, at $\sqrt{s_{\mathrm{NN}}} = 5.02$ TeV, the extrapolation of the charged particle pseudorapidity density scaled with average number of participant does not show a similar behaviour in the fragmentation region as observed at lower energies. The lack of data around the beam rapidity region and the asymmetric values around $\eta = 0$ refrain us to draw any solid conclusion on the behaviour observed at highest LHC energies.

Now, we evaluate $d\sigma^{\mathrm{AA}}/d\eta$ using Eq. 5.7 for $\sqrt{s_{\mathrm{NN}}} = 19.6$ GeV to 5.02 TeV taking the x parameters from Ref. [248], which is almost energy independent from RHIC to LHC energies. The inelastic cross-sections for various energies are taken from Ref. [57, 243–245]. The Monte Carlo

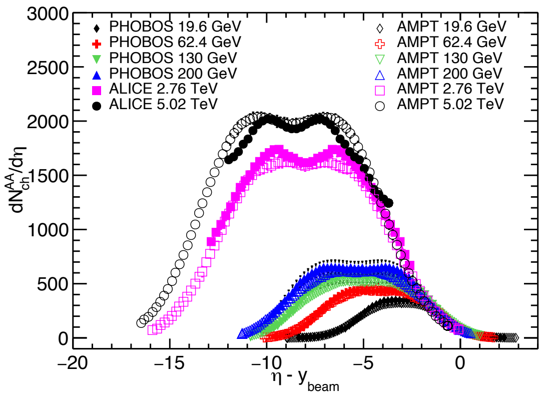

Figure 5.5: The comparison of AMPT model predictions with experimental data on $dN_{\rm ch}^{\rm AA}/d\eta$ versus $\eta - y_{\rm beam}$ for various energies [238].

Glauber model [254] is used to calculate number of participants ($N_{\rm part}$) and number of binary collisions ($N_{\rm coll}$) at different energies. The differential cross-section per unit pseudorapidity for various center-of-mass energies starting from $\sqrt{s_{\rm NN}}$ = 19.6 GeV to 5.02 TeV are shown in Fig. 5.4 with respect to $\eta - y_{\rm beam}$. We notice that the limiting fragmentation hypothesis appears to be violated at LHC energies, *i.e.* at $\sqrt{s_{\rm NN}}$ = 2.76 and 5.02 TeV. These findings suggest that, it is very important to consider the energy dependent $\sigma_{\rm in}$ in order to study LF phenomenon particularly at LHC energies.

The experimental data for pseudorapidity distributions of charged particles in the full phase space are not available at the LHC energies. In addition, a double Gaussian extrapolation of $dN_{\rm ch}/d\eta$ to the $y_{\rm beam}$ at a given energy, seem to introduce an artefact in the spectra, which forbids one to look into the hypothesis of limiting fragmentation. To circumvent this problem, we take AMPT model in string melting scenario [60] as tuned in Ref. [255] for the most central bin 0-6% and 0-5% for RHIC and LHC energies, respectively. We have then compared the measured experimental data for pseudorapidity distribution of charged particles [57, 251–253] with the results obtained in AMPT model. The comparison of experimental data with the AMPT model prediction is shown in Fig. 5.5. AMPT predictions reproduce the mid-rapidity and the fragmentation region very well but cannot reproduce around the peak region ($\eta \sim 0$) at RHIC energies.

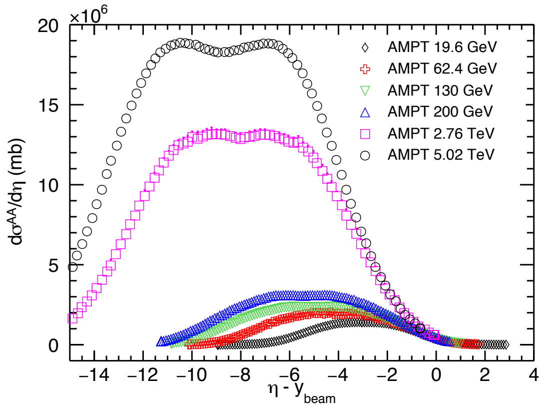

Figure 5.6: $d\sigma^{\mathrm{AA}}/d\eta$ versus $\eta - y_{\mathrm{beam}}$ using AMPT results [238].

For LHC energy at $\sqrt{s_{\mathrm{NN}}} = 2.76$ TeV, the AMPT predictions are in good agreement with the experimental data except for the mid-rapidity region, where the predictions slightly underestimate the measured data. Similarly, for $\sqrt{s_{\mathrm{NN}}} = 5.02$ TeV, the predictions from AMPT model slightly overestimate the data measured for 0-5% centrality bin. In this figure, we see that the phenomenon of longitudinal scaling is observed at RHIC and LHC energies. Theses findings are also described in the Ref. [256], where various transport models like AMPT and the Ultra-relativistic Quantum Molecular Dynamics (UrQMD) model are used to study this phenomenon. They observed that AMPT (both default and string melting versions) and UrQMD with default version show the longitudinal scaling in pseudorapidity distributions of charged particles at RHIC and LHC energies.

We convert the AMPT results of $dN_{\mathrm{ch}}^{\mathrm{AA}}/d\eta$ into $d\sigma^{\mathrm{AA}}/d\eta$ using Eq. 5.7. In Fig. 5.6, we have shown $d\sigma^{\mathrm{AA}}/d\eta$ versus $\eta - y_{\mathrm{beam}}$ to see the longitudinal scaling phenomena in the fragmentation region for different energies from 19.6 GeV to 5.02 TeV. Again, we have found a similar observation for the AMPT model as observed in the experimental data i.e. LF is observed up to RHIC energies in $d\sigma^{\mathrm{AA}}/d\eta$ and seems to be violated for LHC energies. Theses findings are very important while discussing the longitudinal scaling hypothesis at LHC energies.

5.3 Conclusions and Outlook

In this work, we have revisited the phenomenon of limiting fragmentation in the pseudorapidity distributions of differential cross-sections of the charged particles using the energy dependent inelastic cross-section. The findings of this analysis are:

- We have observed the limiting fragmentation phenomenon in the experimental data of $dN_{\rm ch}^{\rm AA}/d\eta$ from $\sqrt{s_{\rm NN}}$ = 19.6 GeV to 2.76 TeV and it is violated at $\sqrt{s_{\rm NN}}$ = 5.02 TeV. Here, the double Gaussian function is used to extrapolate the experimental data in the fragmentation region. However, on the basis of extrapolation method, one can not infer any exact physics conclusions.

- We have transformed experimental data of $dN_{\rm ch}^{\rm AA}/d\eta$ to $d\sigma^{\rm AA}/d\eta$ for various energies from $\sqrt{s_{\rm NN}}$ = 19.6 GeV to 5.02 TeV and see the distributions in the rest frame of one of the nuclei. We have found that the LF hypothesis seems to be violated at both the energies i.e. at $\sqrt{s_{\rm NN}}$ = 2.76 and 5.02 TeV, when one considers the energy dependent inelastic cross-section.

- We have also studied the phenomenon of longitudinal scaling using AMPT model and employing the same procedure as used for the experimental data. Our studies suggest that, AMPT seems to show a possible violation of limiting fragmentation phenomenon for $d\sigma^{\rm AA}/d\eta$ at LHC energies.

- The hypothesis of LF comes as a natural outcome when the particle production follows the Landau hydrodynamics, with a Gaussian pseudorapidity profile.

- LF works fine, when the hadronic cross-section is assumed to be almost independent of energy, which is not the case and hence it is expected to be violated at higher energies. We find that the limiting fragmentation appears to be violated at LHC energies while using the energy dependent cross-section.

- The thermal model with Landau extrapolation to LHC for charged particles, predicts a violation of LF at LHC [257]. What about photons in this framework? It has been observed that for pions in thermal model with longitudinal flow, the LF is violated at the LHC energies [258]. What about photons with a longitudinal flow? These need further investigations.

- It is expected that at higher energies, Landau hydrodynamics should fail and we should expect Bjorken boost invariant hydrodynamics to work out, with the observation of a mid-rapidity plateau. If LF is a natural outcome of Landau model, then LF should be violated at LHC for two reasons: i) failure to see a Gaussian pseudorapidity distribution and ii) cross-sections vary substantially towards higher collision energies.

- At lower collision energies, baryon stopping at the mid-rapidity is expected and the $dN_{\mathrm{ch}}/d\eta(y)$ is expected to follow a Gaussian-like behaviour, which could be described by the particle production in Landau hydrodynamic model. Hence, at these energies, the observation of a limiting fragmentation hypothesis in particle production is expected. But at higher energies, where Landau hydrodynamics fails due to the absence of Gaussian rapidity distribution, LF is found to be violated.

- Going from the top RHIC energy to the LHC energies, there is an order of magnitude increase in the collision energy. Considering at least two units of (pseudo)rapidity overlap for the LF to be valid, the observed y_{beam} at $\sqrt{s_{\mathrm{NN}}}$ = 200 GeV and 5.02 TeV makes hardly any overlap in (pseudo)rapidity. While looking into the possible observation of limiting fragmentation, one looks at spectral overlap in the fragmentation region, which may not be expected as mentioned.

Hence, RHIC can't be combined with LHC while looking for the hypothesis of Limiting Fragmentation.

- Theoretical models are mostly assumption dependent. In order to validate a model, one needs to confront a model to experimental data. We need forward charged particle and photon detectors at the LHC energies in order to validate the LF hypothesis. In the absence of this, extrapolation of any theoretical findings from mid-rapidity to extreme forward rapidity would be a speculation sometimes or a mere coincidence, as the physics of particle production is highly rapidity dependent. In view of this, in the present work we have taken the inelastic cross section with the collision geometry to study the LF hypothesis. This is the novelty of the present work.

Chapter 6

Summary and Outlook

"Knowledge has its boundary line, where it abuts on ignorance; on the outside of that boundary line are ignorance and miracles; on the inside of it are science and no miracles."

– Horace Mann

In this thesis, the first measurements for $K^*(892)^{\pm}$ resonance obtained in inelastic pp collisions at 5.02 and 8 TeV LHC energies are presented. Due to its very short lifetime it is used for the study of the in-medium dynamics of the strongly interacting QCD matter. And as it contains strange (s) quark it may also give information about the mechanism and dynamics of strange particle production in the medium. The transverse momentum spectra have been measured at mid-rapidity $|y| < 0.5$ in the range $0 < p_T < 15$ GeV/c. The measurements of $K^{*\pm}$ complement and confirm the results at the same collision energies of the K^{*0} meson. The p_T-spectra compared with QCD-inspired models (PYTHIA6, PYTHIA8) and hybrid model (EPOS–LHC). With the increase of collision energy the agreement of the QCD-inspired models increases with data. The EPOS-LHC is able to well reproduce the hardening of the p_T-spectrum with the increase of the collision energy. The $K^{*\pm}$ transverse momentum spectrum is harder going from 5.02 to 13 TeV collision energy and an increase in the $\langle p_T \rangle$ of about 11% is observed from 5.02 to 13 TeV collisions. The evolution of the p_T-spectra with collision energy is clearly seen considering the ratios of the $K^{*\pm}$ p_T-spectra at $\sqrt{s} = 8$ and 13 TeV to 5.02 TeV. The observed increase of the slope for $p_T < 1$ GeV/c suggests an increase of the hard scattering processes with the collision energy. While a particle production mechanism in the soft energy region is independent of the collision energy. This is suggested by the same yield value, within the estimated uncertainties for all the three energies. Multiplicity study of $K^{*\pm}$ in pp collisions at the same energies will reveal more information about the production mechanism. Subsequently, measurement of $K^{*\pm}$ like resonances in p–Pb, Xe–Xe and Pb–Pb collisions will strengthen our physics understanding.

We have also presented the study of equilibrium thermodynamical and transport properties such as energy density, shear viscosity, trace anomaly, speed of sound, entropy density, and bulk viscosity of the QCD matter created at RHIC energies by using the clustering of color sources phenomenology. The color suppression factor, F(ξ) is responsible for reduction in multiplicity and enhancement of transverse momentum for heavy-ion collisions. It is observed that the results are in excellent agreement with the lattice QCD data. The initial temperatures at RHIC energies are presented with different model predictions of chemical freeze-out temperature (T_{ch}), and baryon chemical potential (μ_B). It is found that the initial temperatures at lower energies are very close to the chemical freeze-out temperatures. As the collision energy increases, the differences between the initial temperatures and the freeze-out temperatures increase. The observations from each and every observable estimated by using CSPM, show indication of a phase transition from de-confined to confined phase most likely between $\sqrt{s_{NN}}$ = 11.5 and 19.6 GeV of collision energy. Another interesting observable, the normalized electrical conductivity (σ_{el}/T), is estimated using the CSPM approach shows a very weak dependence on the temperature. The results obtained in CSPM validate the outcomes from BAMPS calculations with fixed strong coupling constant. We have studied the ratio $(\eta/s)/(\sigma_{el}/T)$, which has gained considerable interest in heavy-ion phenomenology. A small value of η/s suggests large scattering rates that can damp the conductivity. It is observed that η/s is affected by the gluon-gluon and quark-quark scatterings while σ_{el}/T is only affected by the quark-quark scatterings. Thus, the ratio between them is important to quantify the contributions from quarks and gluons in various temperature regions. It is observed that this ratio behaves in a fashion similar to η/s.

In our another work with the same framework we have investigated percolation parameters and various thermodynamical observables in nucleus–nucleus collisions at RHIC energies as a function of collision centrality. We have studied the percolation density parameter as a function of the number of participants at various RHIC energies. We find that, the critical percolation density ($\xi_c \sim 1.2$) is reached for the most central collisions at all the analysed collision energies. $F(\xi)$ is also studied and a universal scaling behaviour of percolation parameters ($F(\xi)$), $\langle p_T \rangle$ and temperature (T) observed when scaled with the transverse overlap area (S_N), which indicates that the percolation string densities are independent of collision systems and collision energies. The results from hadron-hadron collisions at $\sqrt{s} = 1.8$ TeV strengthen the observation showing a similar behaviour as obtained in Au+Au collisions. The minimum η/s is observed for the most central collisions at $\sqrt{s_{\rm NN}} = 130$ and 200 GeV, which envisages the formation of perfect fluid like matter created at these energies. It would be interesting to study other observables like, isothermal compressibility, thermal conductivity etc. using CSPM approach at other available collision energies and collision species.

We have revisited, the phenomenon of limiting fragmentation in the pseudorapidity distributions of differential cross-sections of the charged particles using the energy dependent inelastic cross-section. The hypothesis of LF comes as a natural outcome when the particle production follows the Landau hydrodynamics, with a Gaussian pseudorapidity profile. We have transformed experimental data of $dN_{\rm ch}^{\rm AA}/d\eta$ to $d\sigma^{\rm AA}/d\eta$ for various energies from $\sqrt{s_{\rm NN}} = 19.6$ GeV to 5.02 TeV and checked the distributions in the rest frame of one of the nuclei. We have observed the limiting fragmentation phenomenon in the experimental data of $dN_{\rm ch}^{\rm AA}/d\eta$ from $\sqrt{s_{\rm NN}} = 19.6$ GeV to 2.76 TeV, however it is violated at $\sqrt{s_{\rm NN}} = 5.02$ TeV LHC energy. But when we consider energy dependent inelastic cross-section to estimate $d\sigma^{\rm AA}/d\eta$, we have found that the LF hypothesis seems to be violated at both the LHC energies i.e. at $\sqrt{s_{\rm NN}} = 2.76$ and 5.02 TeV. We have also investigated the phenomenon of longitudinal scaling using AMPT model tuned with parameters and employing the same procedure as used for the experimental data. Our studies suggest that, AMPT seems to show a possible violation of limiting fragmentation phenomenon for $d\sigma^{\rm AA}/d\eta$ at LHC energies, whereas for $dN_{\rm ch}^{\rm AA}/d\eta$ LF is respected upto $\sqrt{s_{\rm NN}}$ = 2.76 TeV. LF works fine, when the hadronic cross-section is assumed to be almost independent of energy, which is not the case and hence it is expected to be violated at higher energies. We find that the limiting fragmentation appears to be violated at LHC energies while using the energy dependent cross-section. In this scenario its worth while to check longitudinal scaling for photons in this framework. Study on thermal model shows the violation of LF for pions with longitudinal flow at the LHC energies. So it opens up to enquire more about photons with a longitudinal flow.

Bibliography

[1] D. J. Griffiths, Introduction to Elementary Particles; Wiley, New York, (2008).

[2] S. L. Glashow, Nucl. Phys. 22, 579 (1961).

[3] A. Salam and J.C. Ward, Phys. Lett. 13, 168 (1964).

[4] S. Weinberg, Phys. Rev. Lett. 19, 1264 (1967).

[5] R. K. Ellis, W. J. Stirling and B. R. Webber, "QCD and Collider Physics", Cambridge University Press, (2003).

[6] D. J. Gross, F. Wilczek, Phys. Rev. D 8, 3633 (1973).

[7] H. D. Politzer, Phys. Rev. Lett. 30, 1346 (1973).

[8] R. Stock, Prog. Part. Nucl. Phys. 42, 295 (1999).

[9] R. C. Hwa, X. Wang, "Quark-Gluon Plasma", vol. 3, World Scientific (2004).

[10] F. Karsch, Nucl. Phys. A **698**, 199 (2002).

[11] J. Cleymans, H. Oeschler, K. Redlich and S. Wheaton, Phys. Rev. C **73**, 034905 (2006).

[12] B. I. Abelev *et al.* [STAR Collaboration], Phys. Rev. C **81**, 024911 (2010).

[13] B. Mohanty [STAR Collaboration], J. Phys. G **38**, 124023 (2011).

[14] B. Mohanty, PoS CPOD **2013**, 001 (2013).

[15] https://particlesandfriends.wordpress.com/2016/10/14/evolution-of-collisions-and-qgp/

[16] Introduction to High Energy Heavy Ion Collisions, C. Y. Wong, World Scientific Publishing Co. (1994).

[17] K. Aamodt *et al.*, ALICE collaboration, JINST 3, S08002 (2008).

[18] T. Matsui and H. Satz, Phys. Lett. B 178, 416 (1986).

[19] (NA60 Collaboration) R. Arnaldi *et al.*, Nucl. Phys., A 783, 261-268 (2007).

[20] (PHENIX Collaboration) A. Adare *et al.*, Phys. Rev. Lett. 98, 232301 (2007).

[21] (PHENIX Collaboration) A. Adare *et al.*, Phys. Rev. C 84, 054912 (2011).

[22] P. Koch, B. Muller, J. Rafelski, Phys. Rep. 142, 167–262 (1986).

[23] (ALICE Collaboration) B. Abelev *et al.*, Phys. Lett. B 728, 216 (2013), Erratum-ibid. 734, 409-410 (2014); (ALICE Collaboration) B. Abelev *et al.*, Phys. Rev. Lett. 111, 222301 (2013).

[24] (STAR Collaboration) G. Agakishiev *et al.*, Phys. Rev. Lett. 108, 072301 (2012).

[25] (NA57 Collaboration) K. F. Hetland *et al.*, J. Phys. G 28, (2002).

[26] S. S. Adler *et al.* [PHENIX Collaboration], Phys. Rev. Lett. **91**, 072301 (2003).

[27] B. B. Back *et al.* [PHOBOS Collaboration], Phys. Rev. Lett. **91**, 072302 (2003).

[28] I. Vitev and M. Gyulassy, Phys. Rev. Lett. **89**, 252301 (2002).

[29] M. Gyulassy, P. Levai and I. Vitev, Phys. Rev. Lett. **85**, 5535 (2000).

[30] X. N. Wang, Phys. Rev. C **70**, 031901 (2004).

[31] R. Pasechnik and M. Sumbera, Universe **3**, 7 (2017).

[32] S. Voloshin, Y. Zhang, Z. Phys. Rev. C **70**, 665 (1996).

[33] A. M. Poskanzer, S. A. Voloshin, Phys. Rev. C **58**, 1671-1678 (1998).

[34] B. I. Abelev *et al.* [STAR Collaboration], Phys. Rev. C **75**, 054906 (2007)

[35] Dénes Molnár and Sergei A. Voloshin, Phys. Rev. Lett. 91, 092301 (2003).

[36] R.J Fries *et al.*, Phys. Rev. C 68, 044902 (2003).

[37] R. C. Hwa and C. B. Yang, Phys. Rev. C 70, 024904 (2004).

[38] E. V. Shuryak, Phys. Lett. B **78**, 150 (1978).

[39] E. L. Feinberg, Nuovo Cim. A **34**, 391 (1976).

[40] G. Domokos, J. Goldman, Phys. Rev. D **23**, 203 (1981).

[41] P. Stankus, Ann. Rev. Nucl. Part. Sci. **55**, 517 (2005).

[42] (ALICE Collaboration) K. Aamodt *et al.*, Phys. Lett. B 696, 328-337 (2011).

[43] (Particle Data Group) Olive, K. A. and others, Chin. Phys. C 38, 090001 (2014).

[44] G. Torrieri, J. Rafelski, Phys. Lett. B 509, 239-245 (2001).

[45] C. M Ko, Phys. Rev. C 23, 2387 (1981).

[46] AguilarBenitez M et. al. , .Z. Phys. C **50** 40 (1991).

[47] T. Sjostrand, S. Mrenna and P. Z. Skands, JHEP **0605**, 026 (2006).

[48] T. Sjostrand, S. Mrenna and P. Z. Skands, Comput. Phys. Commun. **178**, 852 (2008).

[49] R. Engel and J. Ranft, Phys. Rev. D **54**, 4244 (1996).

[50] N. S. Amelin, M. A. Braun and C. Pajares, Phys. Lett. B **306**, 312 (1993).

[51] M. A. Braun, F. Del Moral and C. Pajares, Phys. Rev. C **65**, 024907 (2002).

[52] M. A. Stephanov, K. Rajagopal, and E. V. Shuryak, Phys. Rev. Lett. **81** 4816 (1998).

[53] M.A. Braun *et al.* Phys. Reports. **509** 1 (2015).

[54] http://www.hbni.ac.in/phdthesis/phys/PHYS04200704003.pdf

[55] J. Benecke, T. T. Chou, C. N. Yang and E. Yen, Phys. Rev. **188**, 2159 (1969).

[56] W. Kittel and E.A. De Wolf, Soft Multihadron Dynamics, World Scientific, Singapore (2005).

[57] B. B. Back *et al.*, Nucl. Phys. A **757**, 28 (2005).

[58] B. I. Abelev *et al.* [STAR Collaboration], Nucl. Phys. A **832**, 134 (2010).

[59] J. Adams *et al.* [STAR Collaboration], Phys. Rev. C **73**, 034906 (2006).

[60] Z. W. Lin, C. M. Ko, B. A. Li, B. Zhang and S. Pal, Phys. Rev. C **72**, 064901 (2005).

[61] L. Evans and P. Bryant, JINST 3, S08001 (2008).

[62] https://indico.cern.ch/event/656452/contributions/2899751/attachments/1648386/2636730/Alic

[63] C. De Melis, "The CERN accelerator complex. Complexe des accélérateurs du CERN", http://cds.cern.ch/record/2119882.

[64] (ATLAS Collaboration) G. Aad *et al.*, JINST 3, S08003 (2008).

[65] (CMS Collaboration) S. Chatrchyan *et al.*, JINST 3, S08004 (2008).

[66] (ATLAS Collaboration) G. Aad *et al.*, Phys. Lett. B 716, 1-29 (2012).

[67] (CMS Collaboration), S. Chatrchyan *et al.*, Phys. Lett. B 716, 30-61 (2012).

[68] (LHCb Collaboration) Alves *et al.*, JINST 3, S08005 (2008).

[69] (ALICE Collaboration) B. Abelev *et al.*, Int. J. Mod. Phys. A 29, 1430044 (2014).

[70] (ALICE Collaboration), JINST 3, S08002 (2008).

[71] P. G. Kuijer, "Commissioning and Prospects for Early Physics with ALICE," Nucl. Phys. A **830**, 81C (2009)

[72] (ALICE TRD Collaboration) Andronic *et al*, Nucl. Instrum. Meth. A 522, 40 (2004); (ALICE Collaboration) Adler *et al*, Nucl. Instrum. Meth. A 552, 364 (2005).

[73] "ALICE Time-Of-Flight system (TOF): Technical Design Report, CERNLHCC-2000-012"; http://cdsweb.cern.ch/record/430132; "ALICE Time-Of-Flight system (TOF): addendum to the technical design report, CERN-LHCC- 2002-016", http://cdsweb.cern.ch/record/545834.

[74] "ALICE Technical Design Report of the Photon Spectrometer (PHOS), CERN/LHCC 99-4 (1999)", https://edms.cern.ch/document/398934/1.

[75] "ALICE electromagnetic calorimeter: addendum to the ALICE technical proposal", CERN-LHCC-2006-014, http://cdsweb.cern.ch/record/932676.

[76] "ALICE electromagnetic calorimeter: addendum to the ALICE technical proposal, CERN-LHCC-2006-014", http://cdsweb.cern.ch/record/932676.

[77] A. Fernandez *et al.* Czech. J. Phys. 55, B801-B807 (2005); A. Fern andez *et al.*, Nucl. Instrum. Meth. A572, 102 (2007).

[78] “ALICE Photon Multiplicity Detector (PMD): Technical Design Report, CERNLHCC-99-032”; http://cdsweb.cern.ch/record/451099;

[79] “ALICE Technical Design Report on Photon Multiplicity Detector, Addendum-1”, CERN/LHCC 2003-038 (2003).

[80] “ALICE forward detectors: FMD, T0 and V0: Technical Design Report”, CERNLHCC-2004-025, http://cdsweb.cern.ch/record/781854.

[81] (ALICE Collaboration) E. Abbas *et al.*, JINST 8, P10016 (2013).

[82] “ALICE Technical Design Report of the Zero Degree Calorimeter (ZDC)”, CERN LHCC-99-005, http://cdsweb.cern.ch/record/381433.

[83] (a) “ALICE dimuon forward spectrometer: Technical Design Report, CERN-LHCC-99-022”; http://cdsweb.cern.ch/record/401974; (b) “ALICE dimuon forward spectrometer: addendum to the Technical Design Report, CERN-LHCC- 2000-046”, http://cdsweb.cern.ch/record/494265.

[84] (ALICE Collaboration), “ALICE Inner Tracking System (ITS): Technical Design Report”, https://cds.cern.ch/record/391175.

[85] J. Wiechula, “Commissioning and Calibration of the ALICE-TPC”, PhD Thesis, Goethe-Universittat Frankfurt am Main, (2008).

[86] “ALICE Time Projection Chamber: Technical Design Report, CERN-LHCC-2000-001”, http://cdsweb.cern.ch/record/451098 (2000).

[87] W. Blum, W. Riegler, and L. Rolandi, “Particle detection with drift chambers”; Springer, Berlin (2008). https://cds.cern.ch/record/1105920.

[88] http://alice-analysis.web.cern.ch/sites/alice-analysis.web.cern.ch/files/documents/Analysis/JensJD.pdf

[89] Particle Identification Studies with an ALICE Test TPC P. Christiansen, for the ALICE TPC Collaboration, Int.J.Mod.Phys.E16:2457-2462 (2007)

[90] J. F. Grosse-Oetringhaus *et al.*, "The ALICE Online-Offline Framework for the Extraction of Conditions Data", Journal of Physics: Conference Series 219, 022010 (2010).

[91] F. Carena *et al.*, Nucl. Inst. and Meth. in Phys. Res. A 741, 130-162 (2014).

[92] (ALICE Collaboration) T. Alt *et al.*, J. Phys., G 30, S1097-S1100 (2004).

[93] (ALICE Collaboration), ALICE Technical Design Report of the Trigger, Data Acquisition, High-Level Trigger, Control System, CERN/LHCC 2003/062 (2004), https://edms.cern.ch/document/456354/2.

[94] T. Sjöstrand, S. Mrenna, and P. Skands, J. High Energy Phys. 05, 026 (2006).

[95] T. Sjöstrand, S. Mrenna *et al.*, Comput. Phys. Commun. 178, 852 (2008).

[96] R. Engel, Z. Phys. C 66, 203 (1995).

[97] Xin-Nian Wang and M. Gyulassy, Phys. Rev. D 44, 3501 (1991).

[98] R. Brun *et al.*, CERN program library long write-up, W5013, GEANT detector description and simulation tool (1994).

[99] S. Agostinelli *et al.*, Nucl. Instrum. Meth. A 506, 250 (2003), http://cdsweb.cern.ch/record/602040.

[100] A. Fasso *et al.*, Proceedings of the IV International Conference on Calorimeters and their Applications, World Scientific, Singapore (1994).

[101] P. Billoir, “Progressive track recognition with a Kalman like fitting procedure”, Comput. Phys. Commun. 57, 390 (1989).

[102] C. Markert [STAR Collaboration], Acta Phys. Hung. A **24**, 175 (2005)

[103] A. Ilner, D. Cabrera, C. Markert and E. Bratkovskaya, Phys. Rev. C **95**, 014903 (2017)

[104] M. Alston, L. W. Alvarez, P. Eberhard, M. L. Good, W. Graziano, H. K. Ticho and S. G. Wojcicki, Phys. Rev. Lett. **6**, 300 (1961).

[105] (STAR Collaboration) J. Adams *et al.*, Nucl. Phys. A 757, 102-183 (2005).

[106] M. Gyulassy *et al.*, Nucl. Phys. A 750, 30-63 (2005).

[107] https://alice-notes.web.cern.ch/node/628

[108] https://alice-notes.web.cern.ch/node/629

[109] ALICE Collaboration, B. Abelev et al., ”Performance of the ALICE Experiment at the CERN LHC”, Int. J. Mod. Phys. A29 (2014) 1430044,

[110] https://aliceinfo.cern.ch/Notes/node/425

[111] https://alice-notes.web.cern.ch/node/425

[112] https://alice-notes.web.cern.ch/node/631

[113] https://alice-publications.web.cern.ch/node/4270

[114] V. Riabov, “$\rho \rightarrow \pi\pi$ production in pp collisions at $\sqrt{s}$= 2.76 TeV with TPC-PID”, ALICE-ANA- 2179, https://aliceinfo.cern.ch/Notes/node/374

[115] T. Ullrich and Z. Xu, “Treatment of errors in efficiency calculations? (Preprint physics/ 0701199v1) (2007)

[116] https://alice-notes.web.cern.ch/node/665

[117] C. Loizides, J. Kamin and D. d'Enterria, Phys. Rev. C **97**, no. 5, 054910 (2018)

[118] https://twiki.cern.ch/twiki/pub/ALICE/PWG2Resonances/Knospe_Grouping_Unc

[119] R. Barlow, hep-ex/0207026.

[120] https://twiki.cern.ch/twiki/bin/viewauth/ALICE/AliDPGtoolsTrackSystematicU

[121] https://alice-notes.web.cern.ch/node/478

[122] J. Adam et al. (ALICE Coll.), "Production of $K^{*}(892)^{0}$ and $\phi(1020)$ in p-Pb collisions at $\sqrt{s}$ = 5.02 TeV",Eur. Phys. J. C 76 (2016) 245.

[123] J. Adam *et al.* [ALICE Collaboration], Eur. Phys. J. C **76**, no. 5, 245 (2016)

[124] https://alice-publications.web.cern.ch/node/4170

[125] R. T. Jimenez Bustamante [ALICE Collaboration], J. Phys. Conf. Ser. **832**, no. 1, 012015 (2017)

[126] https://alice-notes.web.cern.ch/node/793

[127] https://alice-notes.web.cern.ch/node/563

[128] B. Andersson, G. Gustafson, G. Ingelman and T. Sjostrand, Phys. Rept. **97**, 31 (1983).

[129] A. Ortiz Velasquez, P. Christiansen, E. Cuautle Flores, I. Maldonado Cervantes and G. Paic, Phys. Rev. Lett. **111**, no. 4, 042001 (2013)

[130] P. F. Kolb, J. Sollfrank, and U. W. Heinz, Phys. Rev. C **62**, 054909 (2000).

[131] J.-Y. Ollitrault, Phys. Rev. D **46**, 229 (1992).

[132] L. Adamczyk *et al.* (STAR Collaboration), Phys. Rev. Lett. **112**, 032302 (2014).

[133] M. Bluhm *et al.* Phys. Rev. C **84**, 025201 (2011).

[134] Nihar Ranjan Sahoo (STAR Collaboration), J. Phys.: Conf. Ser. **535**, 012007 (2014).

[135] Y. Hirono, M. Hongo and T. Hirano, Phys. Rev. C **90**, 021903 (2014).

[136] K. Tuchin, Adv. High Energy Phys. **2013**, 490495 (2013).

[137] Gordan Baym, Physica 96A ,131(1979).

[138] T. Celik, F. Karsch, H. Satz, Phys. Lett. B 97 128 (1980).

[139] L. McLerran and R. Venugopalan Phys. Rev. D **49**, 2233 (1994).

[140] http://www.curtismeyer.com/material/lecture.pdf

[141] M. B. Isichenko, Rev. Mod. Phys. **64**, 961 (1992).

[142] H. Satz, Rept. Prog. Phys. **63**, 1511 (2000).

[143] J. Dias de Deus, C. Pajares, Phys. Lett. B **642**, 455 (2006).

[144] P. Sahoo, S. K. Tiwari, S. De, R. Sahoo, R. P. Scharenberg and B. K. Srivastava, Mod. Phys. Lett. A **34**, 1950034 (2019)

[145] A. Bazavov *et al.*, Phys. Rev. D **80**, 014504 (2009).

[146] L. J. Gutay *et al.*, Int. J. Mod. Phys. E **24**, 1550101 (2015).

[147] R. P. Scharenberg, B. K. Srivastava and A. S. Hirsch, Eur. Phys. J. C **71**, 1510 (2011).

[148] M.A. Braun, C. Pajares, Eur. Phys. J. C **16**, 349 (2000).

[149] D. Kharzeev, E. Levin and K. Tuchin , Phys. Rev. C **75**, 044903 (2007).

[150] S. W. Hawking, Commun. Math. Phys. **43**, 199 (1975).

[151] W. G. Unruh, Phys. Rev. D **14**, 870 (1976).

[152] F. Becattini, P. Castorina, A. Milov and H. Satz, Eur. Phys. J. C **66**, 377 (2010).

[153] A. Bazavov *et al.*, Phys. Rev. D **95**, 054504 (2017).

[154] F. Becattini *et al.*, Phys. Lett. B **764**, 241 (2017).

[155] S. Das (STAR Collaboration), EPJ Web Conf. **90**, 08007 (2015).

[156] J. D. Bjorken, Phys. Rev. D **27**, 140 (1983).

[157] B. I. Abelev *et.al.* (STAR Collaboration), Phys. Rev. C. **79**, 034909 (2009).

[158] L. Adamczyk *et al.* (STAR Collaboration), arXiv:1701.07065 [nucl-ex].

[159] C. Y. Wong, Introduction to High Energy Heavy-Ion Collisions (World Scientific, Singapore, 1994).

[160] J. Schwinger, Phys. Rev. **128**, 2425 (1962).

[161] S. K. Tiwari, P. K. Srivastava and C. P. Singh, Phys. Rev. C **85**, 014908 (2012).

[162] I. Arsene *et al.* (BRAHMS Collaboration), Nucl. Phys. A **757**, 1 (2005).

[163] J. Adams *et al.* (STAR Collaboration), Nucl. Phys. A **757**, 102 (2005).

[164] K. Adcox *et al.* (PHENIX Collaboration), Nucl. Phys. A **757**, 184 (2005).

[165] B. Mohanty, and V. Roy, Current Science, **103**, 1267 (2012) and references therein.

[166] J. Dias de Deus *et al.*, Eur. Phys. J. C **72**, 2123 (2012).

[167] P. Danielewicz and M. Gyulassy, Phys. Rev. D **31**, 53 (1985).

[168] T. Hirano and M. Gyulassy, Nucl. Phys. A **769**, 71 (2006).

[169] P. Kovtun, D. T. Son and A. O. Starinets, Phys. Rev. Lett. **94**, 111601 (2005).

[170] M. Cheng *et al.*, Phys. Rev. D **81**, 054504 (2010).

[171] A. Bazavov *et al.* [HotQCD Collaboration], Phys. Rev. D **90**, 094503 (2014).

[172] S. Borsanyi *et al.*, JHEP **1011**, 077 (2010).

[173] C. Schmidt and S. Sharma, arXiv:1701.04707 [hep-lat].

[174] K. Dusling and T. Schafer, Phys. Rev. C **85**, 044909 (2012).

[175] F. Karsch, D. Kharzeev and K. Tuchin, Phys. Lett. B **663**, 217 (2008).

[176] W. Cassing, O. Linnyk, T. Steinert and V. Ozvenchuk, Phys. Rev. Lett. **110**, 182301 (2013).

[177] K. Fukushima, D. E. Kharzeev and H. J. Warringa, Phys. Rev. D **78**, 074033 (2008).

[178] P. B. Arnold, G. D. Moore and L. G. Yaffe, JHEP **0011**, 001 (2000).

[179] P. B. Arnold, G. D. Moore and L. G. Yaffe, JHEP **0305**, 051 (2003).

[180] S. Gupta, Phys. Lett. B **597**, 57 (2004).

[181] G. Aarts, C. Allton, J. Foley, S. Hands and S. Kim, Phys. Rev. Lett. **99**, 022002 (2007).

[182] P. V. Buividovich, M. N. Chernodub, D. E. Kharzeev, T. Kalaydzhyan, E. V. Luschevskaya and M. I. Polikarpov, Phys. Rev. Lett. **105**, 132001 (2010).

[183] H.-T. Ding, A. Francis, O. Kaczmarek, F. Karsch, E. Laermann and W. Soeldner, Phys. Rev. D **83**, 034504 (2011).

[184] Y. Burnier and M. Laine, Eur. Phys. J. C **72**, 1902 (2012).

[185] B. B. Brandt, A. Francis, H. B. Meyer and H. Wittig, JHEP **1303**, 100 (2013).

[186] A. Amato, G. Aarts, C. Allton, P. Giudice, S. Hands and J. I. Skullerud, Phys. Rev. Lett. **111**, 172001 (2013).

[187] T. Steinert and W. Cassing, Phys. Rev. C **89**, 035203 (2014).

[188] A. Puglisi, S. Plumari and V. Greco, Phys. Lett. B **751**, 326 (2015).

[189] S. I. Finazzo and J. Noronha, Phys. Rev. D **89**, 106008 (2014).

[190] S. Mitra and V. Chandra, Phys. Rev. D **94**, 034025 (2016).

[191] P. K. Srivastava, L. Thakur and B. K. Patra, Phys. Rev. C **91**, 044903 (2015).

[192] G. D. Moore and J. M. Robert, arXiv:hep-ph/0607172.

[193] G. Baym and H. Heiselberg, Phys. Rev. D **56**, 5254 (1997).

[194] D. Fernandez-Fraile and A. Gomez Nicola, Phys. Rev. D **73**, 045025 (2006).

[195] P. Sahoo, S. K. Tiwari and R. Sahoo, Phys. Rev. D **98**, 054005 (2018)

[196] J. Anderson and H. Witting, Physica (Utrecht) **74**, 466 (1974).

[197] M. Greif, I. Bouras, C. Greiner and Z. Xu, Phys. Rev. D **90**, 094014 (2014).

[198] M. Greif, C. Greiner and G. S. Denicol, Phys. Rev. D **93**, 096012 (2016). Erratum: [Phys. Rev. D **96**, 059902 (2017).]

[199] S. Caron-Huot, P. Kovtun, G. D. Moore, A. Starinets and L. G. Yaffe, JHEP **0612**, 015 (2006).

[200] G. Aarts, C. Allton, A. Amato, P. Giudice, S. Hands and J. I. Skullerud, JHEP **1502**, 186 (2015).

[201] L. Thakur, P. K. Srivastava, G. P. Kadam, M. George and H. Mishra, Phys. Rev. D **95**, 096009 (2017).

[202] H. B. Meyer, Phys. Rev. D **76**, 101701 (2007).

[203] A. Nakamura and S. Sakai, Phys. Rev. Lett. **94**, 072305 (2005).

[204] S. Sakai and A. Nakamura, PoS LATTICE **2007**, 221 (2007).

[205] R. Marty, E. Bratkovskaya, W. Cassing, J. Aichelin and H. Berrehrah, Phys. Rev. C **88**, 045204 (2013).

[206] A. Puglisi, S. Plumari and V. Greco, Phys. Rev. D **90**, 114009 (2014).

[207] P. Sahoo, S. De, S. K. Tiwari and R. Sahoo, Eur. Phys. J. A **54**, 136 (2018).

[208] C. Adler *et al.* [STAR Collaboration], Phys. Rev. Lett. **89**, 202301 (2002).

[209] B. I. Abelev *et al.* [STAR Collaboration], Phys. Lett. B **655**, 104 (2007).

[210] C. Loizides, Phys. Rev. C **94**, 024914 (2016).

[211] H. Satz, Nucl. Phys. A **642**, 130 (1998).

[212] E.K.G. Sarkisyan, A.S. Sakharov, Eur. Phys. J. C **70**, 533 (2010).

[213] A. N. Mishra, R. Sahoo, E. K. G. Sarkisyan and A. S. Sakharov, Eur. Phys. J. C **74**, 3147 (2014) Erratum: [Eur. Phys. J. C **75**, 70 (2015)].

[214] E. K. Sarkisyan-Grinbaum, A. N. Mishra, R. Sahoo and A. S. Sakharov, arXiv:1803.01428 [hep-ph].

[215] E. K. G. Sarkisyan, A. N. Mishra, R. Sahoo and A. S. Sakharov, Phys. Rev. D **93**, 054046 (2016) Addendum: [Phys. Rev. D **93**, 079904 (2016)].

[216] A. Jipa *et al.*, Rom. Rep. Phys. **56**, 577 (2004).

[217] P. Brogueira, J. Dias de Deus and C. Pajares, Phys. Rev. C **75**, 054908 (2007).

[218] F. Gelis, A. M. Stasto and R. Venugopalan, Eur. Phys. J. C **48**, 489 (2006).

[219] J. Jalilian-Marian, Phys. Rev. C **70**, 027902 (2004).

[220] Yu. P. Nikitin and I.L. Rozental, Theory of Multiparticle Production Processes, Harwood Academic Publishers (1988).

[221] G. Wolschin, J. Phys. G **40**, 045104 (2013).

[222] G. Wolschin, Eur. Phys. J. A **5**, 85 (1999).

[223] B. B. Back *et al.* (PHOBOS Collaboration), Phys. Rev. C **74**, 021902(R) (2006).

[224] G. Alner *et al.*, (UA5 Collaboration), Z. Phys. C **33**, 1 (1986).

[225] B. Alver *et al.* (PHOBOS Collaboration), Phys. Rev. Lett. **102**, 142301 (2009).

[226] J. Adams *et al.* (STAR Collaboration), Phys. Rev. Lett. **95**, 062301 (2005).

[227] B. I. Abelev *et al.* (STAR Collaboration), Nucl. Phys. A **832**, 134 (2010).

[228] B. B. Back *et al.* (PHOBOS Collaboration), Phys. Rev. C **72**, 031901(R) (2005).

[229] B. B. Back *et al.*(PHOBOS Collaboration), Phys. Rev. Lett. **91**, 052303 (2003).

[230] B. Abelev *et al.* [ALICE Collaboration], Phys. Rev. Lett. **110**, no. 3, 032301 (2013)

[231] B. B. Abelev *et al.* (ALICE Collaboration), Eur. Phys. J. C **75**, 146 (2015).

[232] A. Bialas and M. Jezabek, Phys. Letts. B **590**, 233 (2004).

[233] J. Ruan and W. Zhu, Phys. Rev. C **81**, 055210 (2010).

[234] M. Nasim, C. Jena, L. Kumar, P. K. Netrakanti and B. Mohanty, Phys. Rev. C **83**, 054902 (2011).

[235] J. Bleibel, L. V. Bravina, A. B. Kaidalov and E. E. Zabrodin, Phys. Rev. D **93**, 114012 (2016).

[236] A. Stasto, Nucl. Phys. A **854**, 64 (2011).

[237] G. Torrieri, Phys. Rev. C **82**, 054906 (2010).

[238] P. Sahoo, P. Pareek, S. K. Tiwari and R. Sahoo, arXiv:1803.05155 [hep-ph]. [Phys. Rev. C, (In Press)]

[239] L. D. Landau, Izv. Akad. Nauk Ser. Fiz. **17**, 51 (1953).

[240] P. Carruthers, Annals N. Y. Acad. Sci. **229**, 91 (1974).

[241] P. Steinberg, Acta Phys. Hung. A **24**, 51 (2005).

[242] J. Steinheimer and M. Bleicher, Eur. Phys. J. A **48**, 100 (2012).

[243] G. Aad *et al.* [ATLAS Collaboration], Nature Commun. **2**, 463 (2011).

[244] B. Abelev *et al.* [ALICE Collaboration], Phys. Rev. C **88**, 044909 (2013).

[245] J. Adam *et al.* [ALICE Collaboration], Phys. Rev. Lett. **116**, 222302 (2016).

[246] P. Carruthers and M. Doung-van, Phys. Rev. D **8**, 859 (1973).

[247] X. N. Wang and M. Gyulassy, Phys. Rev. Lett. **86**, 3496 (2001)

[248] A. Nath Mishra, R. Sahoo, P. Sahoo, P. Pareek, N. K. Behera and B. K. Nandi, Eur. Phys. J. A **52**, 319 (2016).

[249] L. Frankfurt, M. Strikman and S. Liuti, Nucl. Phys. A **527**, 571C (1991).

[250] R. C. Hwa, In Beijing 1989, Proceedings, Relativistic heavy-ion collisions, 239-308 and Oregon Univ. Eugene - OITS-412 (89,rec.Jul.) 68 p.

[251] B. B. Back *et al.* [PHOBOS Collaboration], Phys. Rev. C **74**, 021901 (2006).

[252] E. Abbas *et al.* [ALICE Collaboration], Phys. Lett. B **726**, 610 (2013).

[253] J. Adam *et al.* [ALICE Collaboration], Phys. Lett. B **772**, 567 (2017).

[254] M. L. Miller, K. Reygers, S. J. Sanders and P. Steinberg, Ann. Rev. Nucl. Part. Sci. **57**, 205 (2007).

[255] S. Basu, T. K. Nayak and K. Datta, Phys. Rev. C **93**, 064902 (2016).

[256] M. Nasim, C. Jena, L. Kumar, P. K. Netrakanti and B. Mohanty, Phys. Rev. C **83**, 054902 (2011).

[257] J. Cleymans, J. Strumpfer and L. Turko, Phys. Rev. C **78**, 017901 (2008).

[258] S. K. Tiwari and R. Sahoo, Eur. Phys. J. A **52**, 365 (2016).